FINAL REPORT

Project Title: Tribological Behavior of Structural Materials in High Temperature Helium Gas-Cooled Reactor Environments

Technical Work Scope Identification: RC-2.3 (Advanced Reactor Components - Helium Tribology for HTGRs)

Covering Period: July 2019 through September 2019 (ID: *16-10210_Q4_FY2019*)

Date of Report: March 31, 2020

Recipient: University of Wisconsin, Madison, WI 53706

Project Number: 16-10210 (DE-NE0008548)

PICSNE Workpackage #: NU-16-WI-UWM_-030301-09

Partners: Argonne National Laboratory, Argonne, IL (Dr. Dileep Singh and Dr. Oyelayo Ajayi)

Other Subcontractors: None

Contact(s): **Principal Investigator:** Dr. Kumar Sridharan (kumar@engr.wisc.edu)

Co-Principal Investigator: None

Technical POC: Dr. Sam Sham

Federal Manager: William Corwin

EXECUTIVE SUMMARY

The High-Temperature Gas-cooled Reactor (HTGR) is a Generation IV concept designed to produce electricity and hydrogen at high efficiencies via high operating temperatures (700 °C or higher). Helium, the primary coolant for HTGRs, contains impurities (e.g., CO, H_2O and CH_4) that can induce corrosion reactions at high temperatures such as oxidation and (de)carburization, which in turn can affect the tribological behavior of components. Incoloy® 800HT (Ni-Fe-Cr austenitic solid-solution alloy) and Inconel® 617 (Ni-Cr-Co-Mo solid-solution alloy) are two high-temperature superalloys currently selected as candidate structural materials for the HTGR. The objective of this study is to evaluate the high-temperature tribological performance of these two candidate alloys after conditioning them in HTGR environments. Four regimes of corrosion were considered: a non-conditioned regime (Regime I), an oxidizing regime (Regime II), a carburizing and oxidizing regime (Regime III), and a carburizing regime (Regime IV). To simulate oxidation in HTGR, samples were conditioned for 22 days at elevated temperatures in a once-through helium loop with 4 ppmv H_2O. Carburization of the samples was achieved by the commercial process, Kolsterising®. In addition, two surface treatments – shot peening and aluminization – were considered as potential routes of improving the alloys' wear resistance. Surface-treated samples were tested both before and after conditioning in Regime II. Tribological testing of the samples was performed via a pin-on-disk tribometer at elevated temperatures in ambient environment – 650 and 750°C for 800HT; 850 and 900°C for 617 – with applied loads of 1N, 2N and 5N. The wear behavior of the alloys was

assessed via wear volume and friction coefficient measurements, supported by morphological, structural and compositional analyses of the wear tracks.

Conditioning the samples in Regime II led to the formation of a chromium oxide on both alloys. This protective scale increased the wear resistance compared to that of as-received samples (Regime I) due to the formation of a compacted ‘glaze’ oxide layer during sliding, rendering the wear track nearly undistinguishable from the unworn background and resulting in wear volumes below the detection limits of the measurement technique. The variability of the friction coefficients of the conditioned samples was also considerably reduced compared to that of the as-received samples due to the glaze layer. Additionally, the initial friction coefficients of the samples conditioned in Regime II were reduced by 45% and 54% compared to those of as-received samples for alloys 800HT and 617, respectively. Carburizing the samples (Regime IV) hardened the surfaces of both alloys and promoted the formation of an iron oxide on 800HT during tribological testing, thereby increasing the wear resistance and decreasing the initial friction coefficient by a factor of two compared to those of as-received 800HT. Alloy 617 exhibited an enhanced wear resistance but similar initial friction coefficient compared to those of as-received samples due to the increased surface hardness. The Mn-Cr oxide developed during Regime III conditioning of 800HT did not develop a glaze layer during tribotesting, even at lower loads. Thus, it was not as protective as the oxide produced during conditioning of Regime

II samples, leading to lower wear resistance of 800HT in Regime III compared to that measured in the Regime II condition.

800HT benefited from the aluminization surface treatment, particularly before conditioning in Regime II, due to the promotion of a wear-resistant aluminum oxide layer during testing and the increase in surface hardness due to the presence of a FeAl intermetallic phase. The presence of this phase caused an order-of-magnitude reduction in wear volumes compared to those of as-received 800HT. Aluminization of 617 decreased its wear resistance, particularly after conditioning in Regime II, due to significant wear of the aluminum oxide via a ceramic wear mechanism. This aluminum oxide was removed during sliding, causing the wear volumes to increase by a factor of five compared to those of 617 conditioned in Regime II.

Shot-peened 800HT exhibited a tribological behavior similar to that of as-received 800HT, despite an enhancement in the rate of chromium oxide formation. Shot-peened 800HT conditioned in Regime II showed lower wear resistance compared to that of 800HT conditioned in Regime II due to the poor adhesion between the oxide and the underlying metal, preventing the formation of the glaze layer during sliding. Shot peening of 617 increased its wear resistance at higher load, reducing worn volumes by 60% compared to that measured with as-received 617. Tribotesting of shot-peened 617 in Regime II revealed

that the glaze-oxide layer was formed at every load, resulting in negligible wear, similar to what was observed from testing 617 after conditioning in Regime II.

Overall, alloy 617 exhibited tribologically superior behavior compared to that of alloy 800HT, as demonstrated by its lower friction coefficients and its order-of-magnitude lower wear volumes when measurable.

ACKNOWLEDGEMENTS

This work was supported by the U.S. Department of Energy (DOE), Nuclear Engineering University Program (NEUP) under Award No. DE-NE0008548.Inconel 617 was provided by Idaho National Laboratory (INL). We thank Dr. Richard Wright of INL, Dr. Sam Sham of ANL and Dr. Yanli Wang of ORNL for guidance on materials and helpful discussions. We gratefully acknowledge the use of facilities and instrumentation supported by NSF through the University of Wisconsin Materials Research Science and Engineering Center, DMR-1720415. We also acknowledge Dr. Robert Erck for his expertise and guidance with the high-temperature tribometer.

PUBLICATIONS

Peer-Reviewed Publications

1. J. Kern et al., “Effects of Aluminization via Thermo-Chemical Diffusion on the Wear Behavior of Structural Materials for High-Temperature Gas-Cooled Reactors,” Metallurgical and Materials Transactions A, *in progress*, 2020

2. V. Pauly et al., “Wear Performance of Incoloy 800HT and Inconel 617 in Various Surface Conditions for High-Temperature Gas-Cooled Reactor Components,” Acta Materialia, *in progress*, 2020

3. V. Pauly et al., “High-Temperature Tribological Behavior of Structural Materials after Conditioning in Impure-Helium Environments for High-Temperature Gas-Cooled Reactor Applications”, Journal of Nuclear Materials vol., 522, p. 311, 2019

4. J. Kern et al., “Versatile composite EDS mapping for identifying domains with distinct chemical compositions,” *in preparation*, 2020

5. D. Grierson et al., “Formation of compacted oxide-layer glaze on Incoloy 800HT and Inconel 617 due to high-temperature wear,” *in preparation*, 2020

Conference Proceedings, Posters, and Presentations

1. K. Sridharan, " Elevated Temperature Tribological Behavior of Alloys 800HT and 617 for High Temperature Gas-cooled Reactor Applications," presented at the TMS Annual Meeting & Exhibition in February, 2020.

2. K. Sridharan, “Corrosion Effects in Materials in High-Temperature Gas-Cooled Reactor (HTGR) Environments,” presented at the Advanced Non-Light Water Reactors – Materials and Component Integrity Workshop in December, 2019.

3. K. Sridharan, “High-temperature Tribological Behavior of Alloys 800HT and 617 after Conditioning in Impure Helium Environments,” presented at the Advanced Materials Program Review in June, 2019

4. V. Pauly, "Tribological Behavior of Alloys 800HT and 617 at Elevated Temperatures and in Impure Helium Environments," presented at the TMS Annual Meeting & Exhibition in March, 2019.

5. K. Sridharan, “Tribological Behavior of Structural Materials in High-Temperature Helium Gas-Cooled Reactor Environments,” presented at the Advanced Materials Program Review in June, 2018

6. V. Pauly et al., “Tribological Behavior of Structural Materials at Elevated Temperatures and in Impure Helium Environments for High-Temperature Gas-Cooled Reactor Applications,” ANS Transactions, vol. 118, no. 1, p. 1462, 2018

7. V. Pauly, “Tribological Behavior of Structural Materials at Elevated Temperatures and in Impure-Helium Environments for High-Temperature Gas-Cooled Reactor Applications,” presented at the American Nuclear Society Annual Meeting in June, 2018.

8. V. Pauly, “Tribological Behavior of Structural Materials in High-Temperature Helium Gas-Cooled Reactor Environments,” presented at the American Nuclear Society Student Conference in April, 2018.

9. K. Sridharan, “Tribological Behavior of Structural Materials in High-Temperature Helium Gas-Cooled Reactor Environments,” presented at the Advanced Materials Program Review in June, 2017

Master’s Thesis

1. V. Pauly, “High-temperature Tribological Behavior of Alloys 800HT and 617 for High-Temperature Helium Gas-cooled Reactor Applications,” University of Wisconsin-Madison, August, 2019.

TABLE OF CONTENTS

TABLE OF FIGURES

1. INTRODUCTION

1.1. Nuclear Energy Overview

Nuclear powerplants are clean electricity sources that provided 19% of the electricity in the USA in 2018 [1] and 10.4% worldwide in 2016 [2]. Based on nuclear fission, this technology presents strong advantages in terms of reducing greenhouse gas emissions and increasing the robustness of energy production. Indeed, current nuclear powerplants' lifecycle greenhouse gas emissions are at least an order of magnitude lower than those of other fossil fuel powerplants and are actually in the same range as wind and solar renewable energies [3]. In addition, nuclear powerplants are capable of operating at high power for extended periods of time and had an average capacity factor of 92.6% in 2018 as compared to 54-58% for coal and natural gas fired combined cycle and 24-43% for solar, wind and conventional hydropower that are more affected by climatic events than nuclear powerplants [4, 5].

As the third generation of reactors is being licensed and built worldwide, the fourth and latest generation of nuclear reactor concepts is being designed. Conceptually, Generation IV reactor concepts share the features of Generation III+ units, as well as the ability to operate at higher temperature, which would allow for higher efficiencies, while opening the possibility of using byproduct heat for processes such as hydrogen production, water desalination, and actinide management [6]. The motivation behind Generation-IV designs is higher safety, sustainability, efficiency and reduced cost, as well as new features that

could provide solution to proliferation. The Generation IV designs have departed from the light-water reactor (LWR) concept and focus on new technologies capable of providing unprecedented features [7].

1.2. HTGR Design

High-Temperature Gas-Cooled Reactors (HTGRs) is a sub-design of the Generation IV Very-High-Temperature Reactors (VHTRs) [8]. It is currently one of the most promising Generation IV reactor concepts since it is the focus of the Next Generation Nuclear Plant (NGNP) project [6]. HTGRs are graphite-moderated nuclear reactors with a once-through uranium fuel cycle heating the helium gas coolant to temperature up to 1000°C [9]. The design of the core can either be a “prismatic block” with a classic graphite core in a single block (see Figure 1), or a “pebble-bed” design where tennis ball-sized pebbles contain thousands of micro-fuel particles called TRISO particles (see Figure 2) [8].

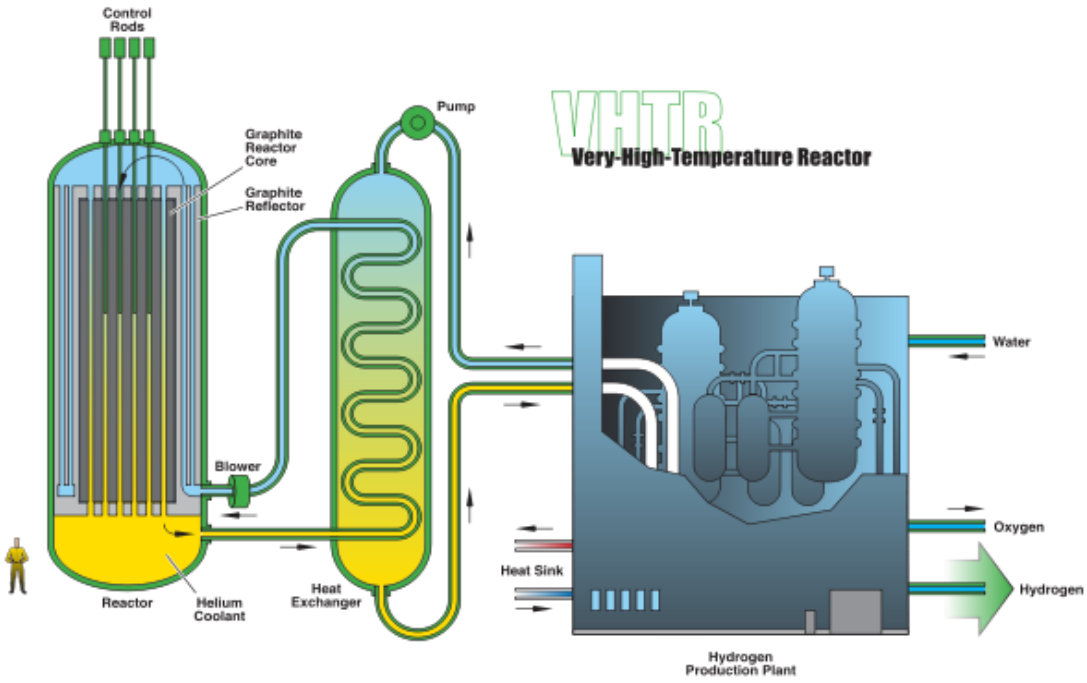

Figure 1: Schematic illustration of the HTGR concept combined with a hydrogen production plant. *Source: Wikipedia.com.*

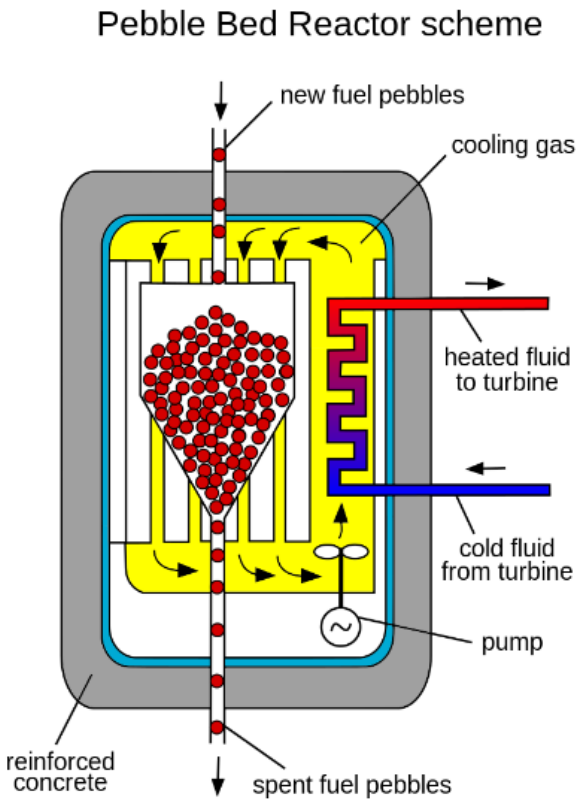

Figure 2: Schematic illustration of the "pebble-bed" reactor design.
(*Source: Wikipedia.com*)

High outlet temperatures allow for higher efficiencies than current LWRs and the byproduct process heat can potentially be used for thermochemical or electrochemical cycles such as hydrogen production [8]. However the high temperatures in HTGRs presents significant challenges in regard to materials selection and deployment [10].

1.3. Motivation

HTGRs will expose structural materials to temperatures that are without any precedent in the nuclear industry. In addition, even if several materials and alloys for high-temperature applications are in use in the petrochemical, metals processing, and aerospace industries, a very limited number of these materials have been tested or qualified for use in nuclear reactor-related systems [11]. Therefore, new materials able to withstand the corrosion, stress and radiation environments for long periods of time at these high temperatures must be studied to ensure that the HTGR design can be commercially implemented.

Incoloy® 800HT (Ni-Fe-Cr austenitic solid-solution alloy) and Inconel® 617 (Ni-Cr-Co-Mo solid-solution alloy) have been selected as candidate materials for the construction of the primary circuit of HTGRs [11]. These two high-temperature superalloys are known for their exceptional high-temperature strength [11] and corrosion resistance [12, 13], and several studies have validated their superior performance under a range of mechanical and environmental conditions [9, 14, 15, 16, 17]. Alloy 617 is currently the primary candidate for construction of the NGNP internal heat exchanger [11], whereas alloy 800HT is already code certified for use in nuclear systems, but for temperatures only up to 760°C [11].

With a target license period of 60 years [9], the primary circuit will be exposed to high-temperature helium flow for several decades and therefore, corrosion is expected to be a major aspect of the materials' degradation over time [13]. Although inert helium will not

cause corrosion, impurities in the gas coolant including H_2, H_2O, CO_2, CO, and CH_4 are inevitable, and these impurities can induce a variety of corrosion reactions at the materials' surfaces [9, 13, 14, 15, 18, 19, 20, 21, 22].

In addition to corrosion, friction and wear can also be mechanisms of degradation in HTGRs. Rubbing components such as valves and control rod drive systems experience friction and wear, and those mechanisms must be understood to ensure the operating condition of these components throughout the life of the reactor. Friction and wear can lead to dimensional recession, wear particulate generation, and self-welding. While control rod drive systems are always active in order to adjust the insertion of reactivity in the core, some valves may be required to move only occasionally. In both cases, the friction and wear experienced by the materials in HTGR environments must be quantified to evaluate their resistance to degradation and sliding. Since few viable liquid or solid lubricants can withstand temperatures higher than 500 °C while limiting the impurities ingress [23], dry sliding is likely to be the main mode of friction and wear. Thus, the corrosion mechanisms involved are expected to have a significant influence on the tribological behavior of the structural materials in mechanical contact with one another [9, 13]. Consequently, the tribological behavior of the alloys' surfaces in contacting and rubbing components is expected to vary dramatically depending on the environmental chemistry.

The objective of the project is to understand the synergy between corrosion and wear in various HTGR environmental regimes and provide experimental data that will ensure long-term operation of primary circuit components of HTGRs.

2. BACKGROUND

2.1. Corrosion

2.1.1. HTGR impurities

Helium has been selected as the primary coolant for the HTGR design [8, 11]. Although it is an inert gas and has no corrosion effect on the materials of the primary circuit, it typically contains impurities that can induce material degradation via oxidation and (de)carburization [13].

Impurities in the primary circuit of HTGRs have different origins:

- The graphite of the core is the primary source of carbon-containing species in the primary circuit, even if air ingress also plays a role [24]. Susceptible to outgassing, graphite oxidizes to form CO and CO_2 [20, 24] and can also react with H_2 via radiolysis to form CH_4 [13, 24].
- H_2O is usually adsorbed on fresh fuel assemblies [24] but can also directly come from lubricant or water ingress [13].
- H_2 originates from the adsorption on the new pebbles [13], diffusion from the steam-water circuit [24] and also reactions between metal and H_2O [13]. It could also

originate from proton diffusion through materials of water-cooled heat exchangers and coolers [20].

These impurities have varying concentration levels in HTGRs based on their ingress rate and their reaction rates with other species [25]. The potential reactions that can take place in HTGR environments have been extensively reported in the literature [18, 19]:

$$H_2O = H_2 + \frac{1}{2}\,O_2 \tag{1}$$

$$C + H_2O = CO + H_2 \tag{2}$$

$$CO + H_2O = CO_2 + H_2 \tag{3}$$

$$CO + 3\,H_2 = H_2O + CH_4 \tag{4}$$

$$C + \frac{1}{2}O_2 = CO \tag{5}$$

$$CH_4 = C + 2\,H_2 \tag{6}$$

Depending on the initial concentrations of impurities, the reactions listed above will influence the composition of the gas during operation [18, 19]. Consequently, although only a limited number of ingresses may happen, all species can potentially be formed in the HTGR environment. The composition during operation is not the equilibrium state since the helium circulates through the primary loop and the graphite core, and the metallic components and the purification systems influence the impurity levels. The high velocity of the gas prevents the attainment of thermodynamic equilibrium [18].

The levels of impurities are usually maintained below 10 ppmv via different filters placed in the primary circuit [13]. In general, molecular sieves are enough to capture most species, but CuO beds are used to oxidize H_2 in H_2O and CO in CO_2 [13]. Table I presents the impurity levels for several high-temperature reactors that were either part of experimental programs or commercial demonstration projects.

Table I: Impurity concentrations in ppmv in helium in several high-temperature helium-cooled reactors [13, 25, 26].

Facility	H_2O	H_2	CO	CO_2	CH_4	O_2	N_2
Dragon	0.1	0.1	0.05	0.02	0.1	0.1	0.05
Peach Bottom	0.5	10	0.5	<0.05	1		0.5
Fort St. Vrain	1	7	3	1	0.1	/	/
AVR	0.15	9	45	0.25	1	/	22
THTR	<0.01	0.8	0.4	0.2	0.1	/	0.1

The DRAGON Reactor Experiment (DRE) was the experimental reactor of the Organization for Economic Cooperation and Development (O.E.C.D.) High Temperature Reactor Project. Operating at 20 atm, the thermal power of the reactor was 21.5 MW with an outlet temperature of 750 °C [26]. The impurity levels of the DRAGON experimental reactor are representative of what is expected to be obtained in future HTGRs since no

particular operations or design flaws seem to have had an impact on the composition of the helium coolant [24].

Peach Bottom was a 40-MWe HTGR operating at 2.4 MPa with an outlet temperature of 1000 K [25]. For this reactor, the impurities were dominated by H_2 and CH_4 due to decomposition of oil originating from ingresses [25]. The Fort St. Vrain HTGR was a 330-MWe plant operating at 4.8 MPa with an outlet temperature of 1050 K. The levels of CO, CO_2 and H_2O in this reactor were higher than expected because of the water ingresses from water-lubricated bearings that subsequently oxidized the graphite core [25]. The AVR reactor was a prototype pebble-bed reactor constructed in 1960 in West Germany that produced a thermal power of 46 MW with an outlet temperature of 950 °C and a helium pressure of 1.1 MPa [13]. The impurities (especially H_2, CO and N_2) were introduced due to air ingresses during the constant loading and unloading of fuel elements. A smaller share of air was adsorbed on the graphite of the new fuel elements while the greater part entered the circuit during loading and unloading [24]. The Thorium High-Temperature Reactor (THTR) was developed to be a commercial demonstration scale pebble bed, based on AVR experience, with a thermal power of 750 MW, a helium pressure of 3.9 MPa and an outlet temperature of 750 °C [13]. During its two years of operation, the THTR showed reasonably low levels of impurities due to active control maintained on the H_2O and CO concentrations to reduce oxidation of the graphite reflectors [13]. It must also be noted that

the presence of N_2 due to air ingress was never high enough to impair other reactions in any of the experiments presented in this section [24].

2.1.2. Corrosion mechanisms

The presence of (de)carburizing and oxidizing impurities in the helium coolant of HTGRs exposes materials of the primary circuit to corrosion. Indeed, the high temperature of the coolant increases the potential for oxidation and (de)carburization: H_2O and O_2 levels as low as 2 ppmv have been shown to be sufficient to trigger oxidation on both 800HT and 617 [14, 15]. Additionally, Christ et al. showed that both CO_2 and H_2O oxidize 617 at temperatures higher than 832 °C, while carburization occurs at temperatures greater than 932 °C [22].

The carbon activity and the partial pressure of O_2 are important indicators of the corrosion potential of the environment since they represent the potential for carburization (decarburization if the activity is low) and the potential for oxidation, respectively [18]. Even if many of the species presented in Table I play a role in the corrosion of materials in HTGR environments, H_2O and CO are particularly important because they play the biggest roles in driving the various corrosion mechanisms of the alloys [9, 13, 22] by dictating the partial pressure of oxygen and the carbon activity [9, 13]. Specifically, CO is really at the heart of the corrosion process, not only because it is capable of both oxidizing and carburizing materials, but also because it is involved in many chemical reactions in the environment.

The Ellingham diagram presented in Figure 3 presents the stability of different oxides that may develop on the surfaces of high-temperature alloys. Since Al_2O_3 appears stable, it is likely to be formed readily on the materials at high temperature. TiO_2 and Cr_2O_3 also appear to be quite stable and are expected to form, while iron oxides have lower stability and may require more aggressive environments to form.

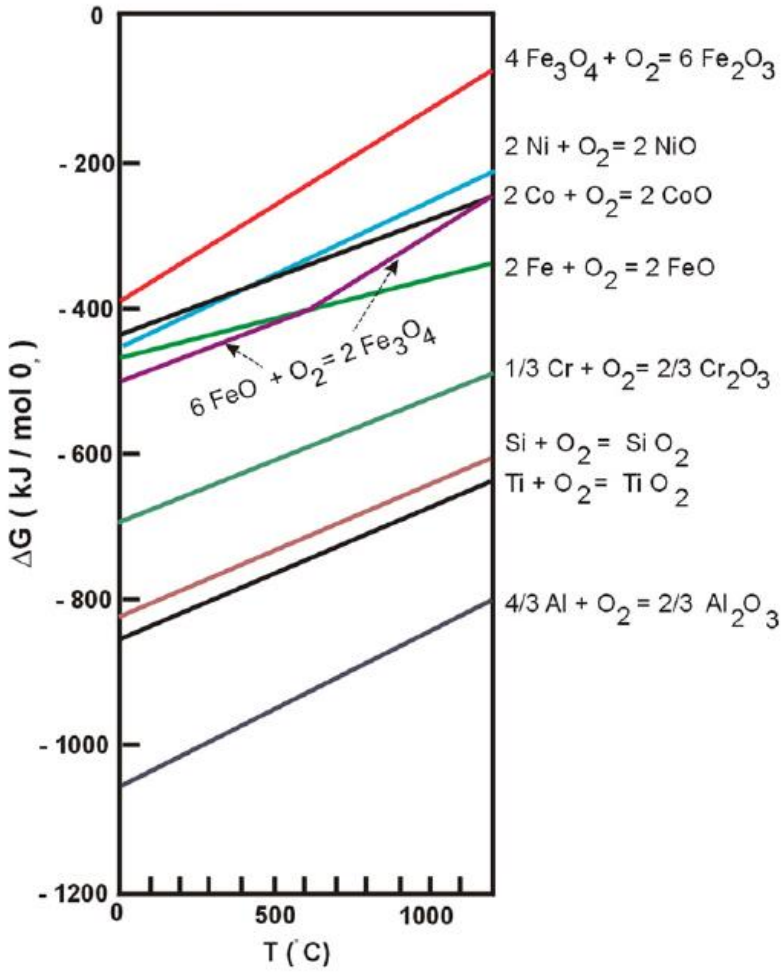

Figure 3: Ellingham diagram for various metal oxides [23].

To better comprehend the corrosion behavior of high-temperature alloys, several chemical equations describing the different corrosion mechanisms of high-temperature alloys in HTGR environments can be studied. The general equation that dictates the oxidation of materials is given in Equation 7.

$$xM + yH_2O = M_xO_y + yH_2 \quad (7)$$

Since the alloy composition plays a major role in dictating which mechanism is more likely, the typical oxidation reactions for Cr-rich and Fe-rich alloys are different and shown in Equations 8 and 9, respectively [12, 21, 24].

$$2\ Cr + 3\ H_2O = Cr_2O_3 + 3\ H_2 \quad (8)$$

$$3\ Fe + 4\ H_2O = Fe_3O_4 + 4\ H_2 \quad (9)$$

Moreover, aluminum is generally added to nickel-based superalloys to improve their high-temperature oxidation resistance by stabilizing the surface oxides such as Cr_2O_3 [15]. Thus, for Ni-based high-temperature alloys, Al_2O_3 is expected to form as an internal oxide [18]. Decarburization is also an important aspect of corrosion. In the case of Cr-rich alloys, as the chromium in the metallic surface is depleted due to the formation of an oxide scale, the equilibrium of the metal-oxide and metal-carbides will be changed and a carbide-free zone should form beneath the oxide scale [18]. In addition, the water vapor contained in the coolant can contribute to the creation of this carbide-free zone via the attack of carbides according to Equation 10 [21].

$$6\ H_2O + Cr_{23}C_6 = 23\ Cr + 6\ CO + 6\ H_2 \quad (10)$$

However, the presence of molybdenum in certain high-temperature alloys opens the door for the creation of stable M_6C carbides, making the alloy more resistant against decarburization [18].

Regarding carburization, as mentioned previously, CO can lead to both oxidation and carbide formation, but only if the temperature is lower than an upper limit around 932 °C [22]. In this case, the reaction shown in Equation 11 is favored [21, 22].

$$6\,CO + 27\,Cr = 2\,Cr_2O_3 + Cr_{23}C_6 \quad (11)$$

If the water vapor level in this environment is low, the carbides can be the stable phase and form on top of the oxide to create a dual scale [19]. For a reducing environment, the increase in carbon content and the dissolution/precipitation of carbides is dictated by the (de)carburizing nature of the environment [20]. Consequently, the oxidizing and/or (de)carburizing nature of the environment can be thought to play an important role in the various corrosion mechanisms at play. Yet, although Ellingham diagrams and reaction equations are useful tools to understand what corrosion mechanisms may take place, they do not incorporate the kinetics of these reactions which constitute a crucial aspect in determining the evolution of the materials' surfaces in HTGR environments.

Decarburization and the development of a carbide-free zone [20] may occur in the initial stages of exposure but will stop once the protective oxide scale is established [22]. In particular, decarburization on Inconel® 617 was only noticed for temperature of 950 °C

and above [22]: this is likely due to the relative stability of the surface oxide layer below this temperature [15]. Similarly, it appears that CH_4 does not play a significant role in carburizing materials above 900 °C as it directly reacts with H_2O [22].

There are many consequences of corrosion of high-temperature alloys in HTGR. Oxides forming on the surface can be flaky and/or removed via sliding contact and may not remain on the surface to protect it from further oxidation. In addition, carburization is known to lead to low temperature embrittlement [13], whereas decarburization reduces creep rupture strength [13]. Thus, an environment capable of readily producing a protective oxide layer should be sought to prevent further corrosion [13]. The optimized composition is slightly oxidizing and can lead to the formation of a protective chromia layer, that has been shown to prevent decarburization [13, 21, 22].

Christ et al. showed that 10 ppmv of H_2O at 850 °C was enough to create an external Cr_2O_3 layer and an internal zone of oxidation with Al_2O_3 particles on 617 [22]. Additionally, after a 3000-hr exposure to 1000 °C air, 617 develops an external chromium oxide, an internal aluminum oxide and a carbide-free zone [9]. Moreover, aggressive environments such as air have been shown to produce additional types of oxide such as NiO, $NiCr_2O_4$, MoO_2 and CoO for 617 [12].

2.1.3. Corrosion regimes

Since the objective of this study is to evaluate the tribological impact of HTGR environments exposure on high-temperature alloys, four regimes of corrosion are considered based on the different corrosion mechanisms described earlier [9, 13].

- **Regime I**: a decarburizing regime that represents a pure helium coolant in which no impurities are present. In this case, no oxide layer is formed, and the surface may become decarburized.
- **Regime II**: an oxidizing regime in which the environment contains only oxidizing impurities such as H_2O. In this regime an oxide layer forms, but surface decarburization may occur in the initial stages of exposure.
- **Regime III**: a regime combining oxidation and carburization. It represents an environment that contains oxidizing and carburizing species such as H_2O and CH_4 or species with both oxidizing and carburizing potentials like CO and CO_2. In this regime, an oxide layer will form, but the sub-surface remains unchanged or becomes slightly carburized.
- **Regime IV**: a carburizing regime representing an environment containing only carburizing species such as CH_4. No oxide layer will form, and the surface will become carburized.

2.2. Tribological behavior

2.2.1. Regimes of tribological behaviors

Various regimes of impurities in the helium coolant will trigger different corrosion mechanisms (oxidation, carburization and/or decarburization) on the surfaces of structural materials. Therefore, even if some features like thermal softening are not related to the coolant composition, it is expected that the tribological behavior of high-temperature alloys used in the primary circuit will vary based on the regime of impurities considered.

No matter the impurity regime, the high temperatures in HTGR will soften structural materials except perhaps in situations where some intermetallic phases like Ni_3Al may form [23]. This is particularly obvious for Inconel® 617 above 850 °C, where a significant decrease in yield strength occurs, as shown in Figure 4.

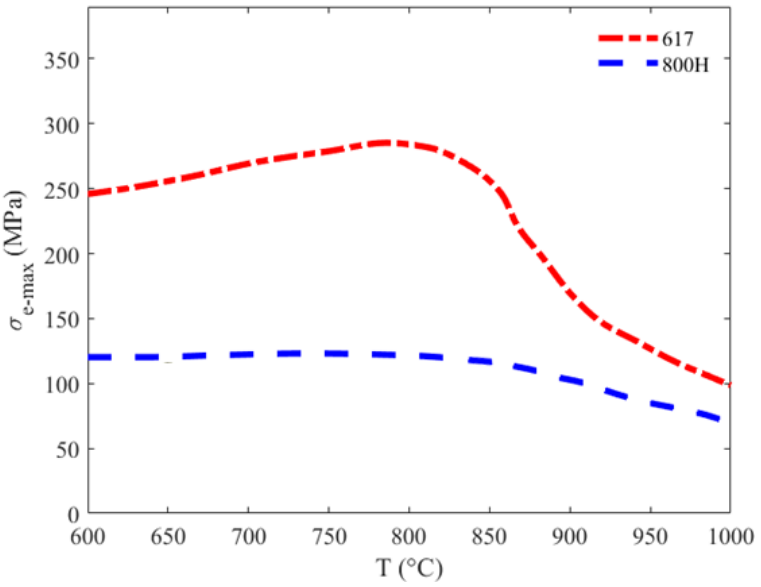

Figure 4: Yield strength as a function of temperature for alloys 800HT [27] and 617 [28].

In general, severe wear is the consequence of combined thermal softening and plastic deformation of the bulk material [29]. When the surface is not protected, the metal-on-metal contact can lead to scuffing and solid-state bonding between surfaces due to high contact temperatures. These mechanisms are thought to be the causes of severe wear of high-temperature alloys and should be avoided. Therefore, the solution to mitigating the wear of alloys in HTGR environments is to surface harden the materials and/or to create a protective layer on the surface. Both can be achieved with the correct environmental composition.

The presence of carburizing impurities or lack thereof in HTGR environments will impact the hardness of the materials' surfaces. Since carburization and decarburization hardens and softens, respectively, the materials' surface [20], the environment of the reactor is likely to have an impact on the tribological behavior of structural materials in that sense. Also, the oxidizing potential of the environment dictates whether an oxide forms on the surface of the alloys. The creation of a protective oxide layer may help the wear transition to less severe mechanisms. In reciprocating wear, as oxide and partially oxidized metal debris particles are generated and retained in the wear track, the wear transitions from severe to mild because of the formation of protective layers after compaction and agglomeration of these particles [30]. This severe-to-mild transition is fostered by low loads that do not break through the oxide layer as well as high ambient temperatures that enables higher oxidation rates and promote sintering [31]. However, increasing the load

above a certain threshold might prevent the transition to mild wear from occurring [29]. The poor adherence and significant ductility of Fe_2O_3 and Fe_3O_4 impair the resistance to high-temperature wear of materials forming these oxides [32]. Since Fe_3O_4 is the main oxide forming on steels above 400 °C, along with Fe_2O_3 and FeO [29], Incoloy® 800HT which is likely to form these oxides may be less resistant to high-temperature wear compared to Inconel® 617.

In addition to the formation of a protective oxide layer in an oxidizing environment, another interesting wear mechanism may take place. Indeed, when the right temperature and contact conditions are met, a 'glaze' oxide layer may form. Under high ambient temperature and a modest load, the reciprocating wear causes the oxide debris to sinter together via thermal softening [16] and produce a hard and smooth compacted oxide layer that drastically reduces the wear rate [31]. These highly light-reflective regions are generally at higher elevation than the surrounding non-load-bearing areas of the wear scar regions [16].

This phenomenon supports the idea that oxidation has a protective effect on high-temperature reciprocating wear [31, 32]. Virtually all the damage to the alloy happens before the glaze layer is established [16]. As temperature increases, the thermal softening and oxidation rate are more important, which accelerates the formation of the glaze layer, thereby reducing the total wear of the sample [16]. Even if the formation of a glaze layer

is time and temperature dependent, only 1 or 2 minutes might be necessary to produce this layer on certain alloys [16]. The glaze layer thickness typically varies between 0.5 and 5 μm [16], and since Fe and steels present higher oxidation rates than Ni-based alloys, the glaze-oxide layer is likely to be thicker when the conditions are favorable for it to form [16].

With Ni-20%Cr alloys forming oxides such as NiO, Cr_2O_3 and $NiCr_2O_4$ [31], Stott et al. have shown that the glaze layer for this type of alloy consists in simple oxides when the ambient temperature is less than 400 °C, and $NiCr_2O_4$ as well as simple oxides at higher temperatures [16]. For this type of alloys, Stott et al. found that the glaze areas cover between 25 and 30% of the wear track after 2h of sliding and up to 90% after longer sliding periods (30-40h) [16]. The glaze was found to contain the major metallic elements in almost the same proportions as those in the alloy, although the thinness of layers render analysis difficult [16]. Yet, it seems that the mechanical properties of the glaze and sub-surface are more pertinent in determining the tribological behavior of the alloys rather than its precise chemical composition [16].

Each corrosion regime described in Section 2.1 will induce surface modifications which are expected to have a strong influence on the tribological behavior of the samples according to the above descriptions. The expected behavior in the various regimes is described for the four regimes:

- **Regime I**: with no oxide layer present to protect the bulk of the material, scuffing is expected to occur. Also, because of the high contact temperatures, solid-state bonding may occur.
- **Regime II**: the formation of an oxide layer suggests that wear of the oxide and/or oxide delamination may take place, leading to three-body wear and the formation of a transfer film. Due to the high-temperature conditions, the transfer film may transform into a glaze layer. During the wear process, this layer can regenerate from the debris created, which maintains a protective layer.
- **Regime III**: as the subsurface does not undergo decarburization, the surface structure should be more wear resistant compared to that of Regime II. Oxide wear and transfer film formation are still expected to occur, and glaze formation remains a strong possibility.
- **Regime IV**: the absence of a protective oxide layer and the hardening of the near surface via carburization will foster abrasive wear as well as solid-state bonding. Grain pull-out may also occur.

The regimes of Sections 2.1 and 2.2 are shown schematically in Figure 5:

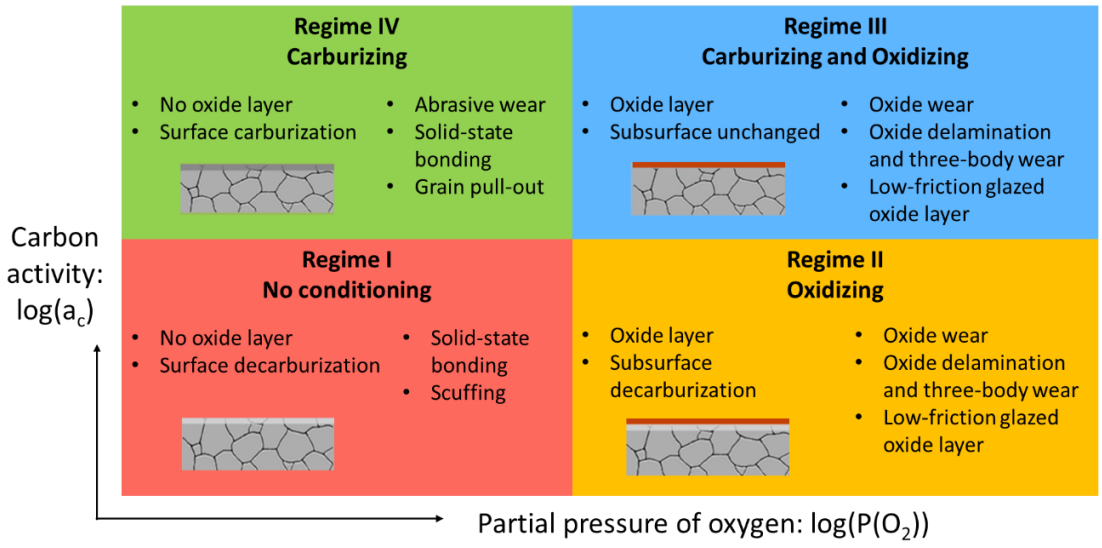

Figure 5: Corrosion regimes and corresponding tribological mechanisms that are relevant for HTGR environmental conditions.

2.2.2. Glaze formation mechanisms

Even if a glaze layer forms on different alloys, the morphology of the sub-surface and the mechanism that creates it might be quite different. Typically, the ambient temperature and the oxidation rate as well as the high-temperature strength of the alloy may differ from one situation to the other and cause the underlying region to be more or less deformed and oxidized.

In Figure 6, Stott et al. proposed three different representations of the cross-sectional morphologies of the load-bearing surfaces for different periods of wear [16]. Figure 6(a) shows the first case corresponding to short period of wear where the glaze lies on top of a gradient of deformed alloy and a chromium-rich internal oxide. Figure 6(b) shows the cross-sectional morphology corresponding to intermediate period of wear where the sub-

surface consists of a compacted layer of oxide and nickel-rich alloy particles lying on top of the previously formed gradient of deformed alloy and internal oxide. Finally, Figure 6(c) presents the morphology obtained after extended period of wear with a sub-surface completely made of compacted oxide particles lying on top of a thick Cr_2O_3 internal oxide layer supported by the gradient of deformed alloy and internal oxide.

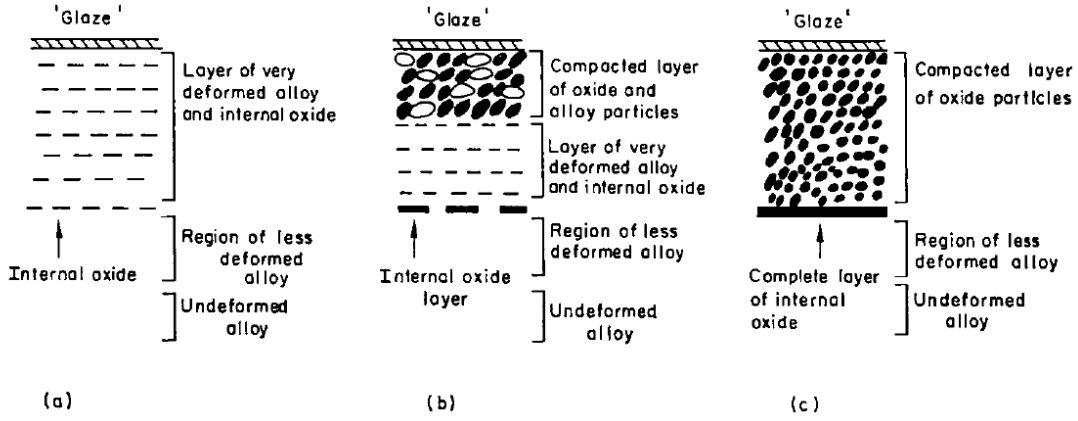

Figure 6: Schematic diagrams showing the morphologies of the load-bearing areas present on Ni-20%Cr alloys after the glaze layer has been established at high temperature [16]: (a) After wear for a short period, (b) after wear for an intermediate period, (c) after wear for a long period

For Ni-based alloys with an increased high-temperature strength, the glaze layer lies on top of a mildly deformed alloy containing little or no internal oxide at any period of wear [16]. Stott et al. also described the different glaze formation mechanisms for Ni-Cr-rich alloys based on their high-temperature strength and the ambient temperature [16]. At the initial stages of sliding, the very thin preformed oxide film is removed, and the alloy is exposed to the atmosphere. Oxide starts forming in the wear track and is being broken and removed via rubbing. As the sliding continues, the contact temperature increases since sliding produces heat at each cycle. The increase in temperature drives the oxidation rate higher

and potentially enough to enable oxide build-up in the wear track. A stable oxide layer may subsequently form on the load-bearing areas. Once this stable oxide layer is established, the high localized temperatures can trigger the sintering of oxide particles via thermal softening thereby creating a glaze layer.

The first mechanism pertains to alloys with significant high-temperature strength and sufficient oxidation rate. Once the glaze is thick enough, it remains stable and intact despite continued sliding. However, a gradient of deformation may have formed under the glaze in the initial stages of sliding. This deformation allows gaseous diffusion of oxygen until a certain depth. If significant deformation and tearing takes place before the glaze is formed, extensive oxidation of the sub-surface may occur during further sliding. In general, the sub-surface comprises different types of oxide with elemental proportions similar to the bulk material. At deeper levels where the oxygen cannot diffuse any further, a Cr_2O_3-rich layer might thicken via outward diffusion of chromium.

Alloys with lower high-temperature strength follow the second mechanism. With softer materials, the surface wear is more severe because the oxide cannot build up to create a stable and thick layer. Larger wear debris are being created and subsequently ground down into smaller oxide particles that may finally sinter together to produce the glaze layer. Once this protective film is established, the sub-surface oxidation stabilizes and is similar to the

first mechanism. This mechanism also pertains to situations with low oxidation rate, typically when the temperature is not significantly high.

The third mechanism is different from the first two as the glaze layer does not remain stable. In certain cases, when the load is too high or the oxidation rate is not significant enough, the oxide layer is consistently ruptured and disrupted during sliding, preventing it from remaining stable on the surface. This allows for further oxidation and deformation of the sub-surface.

3. MATERIALS AND METHODS

3.1. Materials

Incoloy® 800HT (Ni-Fe-Cr austenitic solid-solution alloy) and Inconel® 617 (Ni-Cr-Co-Mo solid-solution alloy) used in this study followed strict composition requirements consistent with ASME codification (UNS N08811, ASTM B408-06, ASME SB408 standards for alloy 800HT and UNS N06617, ASTM B168-08, ASME SB168 standards for alloy 617), and their compositions are listed in Table II.

Table II: Composition of alloys 800HT and 617 used in this study (at%).

Element	Fe	Ni	Cr	Mn	C	Cu	Si	S	Al	Ti	Mo	Co
800HT	45.8	31.4	19.7	1.01	0.066	0.25	0.25	0.001	0.43	0.54	/	/
617	1.6	54.1	22.2	0.1	0.05	0.04	0.1	<0.002	1.1	0.4	8.6	11.6

Alloy 617 is currently not code certified for use in nuclear systems [11], whereas alloy 800HT already is, but only for temperatures up to 760°C [11]. Therefore, this project will contribute to the code certification of the two alloys regarding corrosion and tribology in HTGR environments.

In general, high-strength properties as well as relatively rapid transient oxidation rates at elevated temperatures are desirable qualities for alloys employed under high temperature sliding conditions [16]. Alloy 617 is known to possess a superior creep resistance [9] due to solid-solution strengthening via Mo and Co [22]. It possesses exceptional creep strength at temperatures above 870°C, good cyclic oxidation resistance, and lower thermal expansion than most austenitic stainless steels [11]. Additionally, it retains toughness after long-time exposure at elevated temperatures, does not form embrittling phases and exhibits

excellent carburization resistance [11]. Alloy 800HT also possesses a solid-solution strengthened austenitic structure. However, upon aging certain precipitates can form that reduce the tensile and creep ductility. It has a lower creep rupture strength and oxidation resistance than alloy 617 [11]. Additionally, only very limited data are currently available on the mechanical properties of this alloy beyond 800°C, especially in impure helium environments [11].

For alloy 800HT, a round bar was procured from the suppliers Corrosion Materials (Houston, TX) and Valbruna Stainless Inc. (Fort Wayne, IN), and alloy 617 plates were provided by Idaho National Laboratory, procured from Thyssenkrupp Materials (Hanover, NJ). The round bar and plate stock were machined into disks and pins for use in a pin-on-disk tribometer (see Section 3.4). All machining of the materials was outsourced to the Caspersen Machining Corporation (DeForest, WI). The disks were 2” in diameter and ¼” in thickness. The pins were cylindrical in shape, with an 8 mm diameter and a 16.7 mm length, and were precision machined to radii of curvature of 16.3 mm radius, 55.3 mm radius, or 255.4 mm radius at one of the circular ends (see Figure 7).

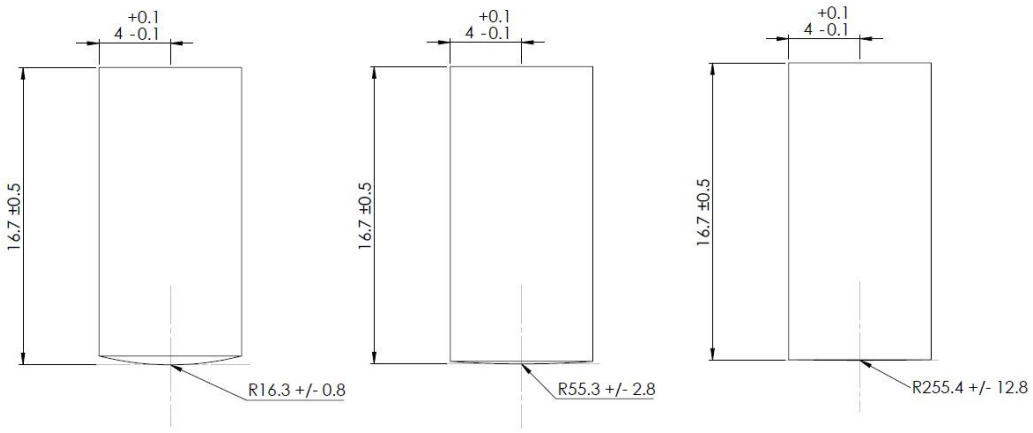

Figure 7: Schematic illustration of the pins used for the tribological tests in this research.

After machining, the disks were polished to remove any imperfections from machining in order to increase reproducibility of the tribotests. The polishing consisted of four steps: three steps of sandpaper polishing (320, 600 and 1200 grit, respectively) for 3 to 6 minutes with a 40 N load, and a final polishing step using a polycrystalline diamond paste (1 μm) for 6 minutes under a 35 N load. Disks and pins were cleaned in an ultrasonic acetone bath prior to conditioning or testing.

3.2. Conditioning

The four regimes presented in Section 2.1.3 cover the different possibilities in terms of corrosion for materials exposed to HTGR environments. In order to simulate these regimes, it was decided that impurities that are only oxidizing or only carburizing would be considered in order to decouple (de)carburization and oxidation. Thus, the only impurity species selected were H_2O and CH_4. This choice offered the possibility of independently varying the partial pressure of oxygen and the carbon activity in the otherwise pure helium.

Regime I was expected to be achieved by exposing samples to high-temperature pure helium for multiple days. After several attempts, the H_2O/O_2 content remained high enough – but still at ppmv levels – to form an oxide layer despite the use of high-purity gas along with a purifier. Consequently, to simulate Regime I, as-received samples were used. This prevented surface oxidation but also decarburization prior to tribological testing.

Regime II was achieved by exposing the samples to high-temperature impure helium with 4 ppmv of water vapor. This impurity level was sufficient to create an oxide layer on both alloys 800HT and 617 after 22 days of exposure as presented in Section 4.1.1.

Regime IV was simulated by carburizing the samples via Kolsterising®, a proprietary Bodycote diffusion process described in Section 4.2 [33]. Carburizing via high-temperature exposure to impure helium with 20 ppmv of CH_4 proved to be challenging due unpreventable oxidation and the low carburizing potential of the alloys.

Regime III was achieved by first carburizing the samples via Kolsterising®, followed by conditioning in the same environment as Regime II.

In addition to these four regimes, samples were also conditioned in ambient air as a reference. Air is expected to be more aggressive than any regime from an oxidation standpoint, however the carburization/decarburization behavior is unpredictable due to the

uncontrolled impurity levels in the environment. A box furnace (Lindberg MPH) was used to condition the samples in air for 20 days. For Regimes II and III, samples were conditioned in a once-through helium flow loop for 22 days. The conditioning temperatures for alloys 800HT and 617 were 750 °C and 900 °C, respectively. The flow loop was designed to maximize sample throughput while maintaining continuous flow of pre-mixed helium gas throughout the system.

Figure 8 presents a schematic drawing depicting the key components of the system, and a photograph of the loop is shown in Figure 9. The upstream controls enabled selection of flow rates of helium (Brooks Instrument), purification of the gas under 0.5 ppmv of moisture and oxygen (SAES Pure Gas), and in-line moisture sensing (Michell Instruments). Adjustments to the pressure were made downstream within a nonporous mullite retort (Mc Danel Advanced Ceramic Tech). The horizontal tube furnace (Thermcraft, Inc) was tuned to maintain a conditioning temperature up to 950 °C with less than 5 °C of variability. Pre-mixed helium tanks were procured from Airgas, Inc.

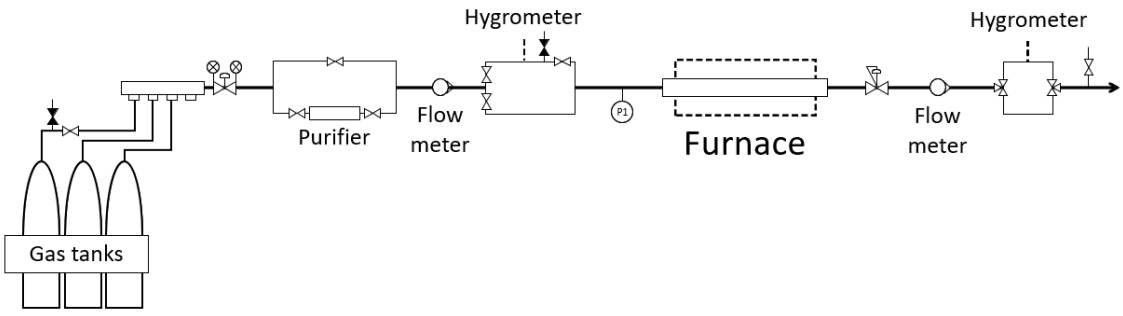

Figure 8: Schematic diagram of the once-through helium flow loop designed, built, and used for this project.

Figure 9: Photograph of the once-through helium loop used in this research.

A protocol was established for conditioning the samples in the helium loop such that the impurity level would be minimum. After placing the samples in the furnace, the loop was evacuated down to 0.5 bar. A flow of high-purity argon was then maintained for 2 days at 120 °C during a step referred to as "baking" to lower the moisture content in the loop. After "baking", the furnace was evacuated again, and the flow of impure helium was established through the loop. The furnace then brought the temperature up to 750 °C or 900 °C for alloys 800HT or 617, respectively, at a temperature ramp rate of 100 °C/hr. After maintaining this condition for 22 days, the samples were passively cooled for 2 days to room temperature. During conditioning, the flow rate was set at 150 sccm, and the pressure within the retort was maintained at 0.5 psig. However, the flow rate and pressure values used are several orders of magnitude lower than commercial HTGR conditions (~1,015

psig and ~ 540 m^3/s) [34]. Still, it appears that higher velocity and pressure do not substantially change the corrosion behavior of the superalloys [13]. Additionally, with a reduced flow velocity, the levels of impurity in the helium coolant were more likely to correspond to the thermodynamic equilibrium [22].

3.3. Surface treatment

In addition to the four regimes of corrosion corresponding to different HTGR regimes, two surfaces treatments – aluminization and shot peening – were investigated to improve the tribological behavior of the two alloys.

3.3.1. Aluminization

Surface treatments/modification of superalloys by diffusion processes has received considerable attention for improving corrosion and wear properties [35]. Aluminizing is a diffusion-based surface modification treatment that aims at increasing oxidation and corrosion resistance [36, 37]. In addition, for the purpose of this study, it is expected that aluminum oxide will increase the wear resistance compared to the oxides that typically form on Ni-Cr-based alloys [37]. Al diffusion coating are particularly promising for superalloys [35]. The process consists in diffusing aluminum into the substrate via a high-temperature aluminum gas exposure. The aluminizing of the samples was conducted by the company, IBC Coatings Technologies Inc. Alloy 800HT and alloy 617 samples were aluminized IBC Coatings Technologies Inc. for 36 hours at 800 °C (Figure 10).

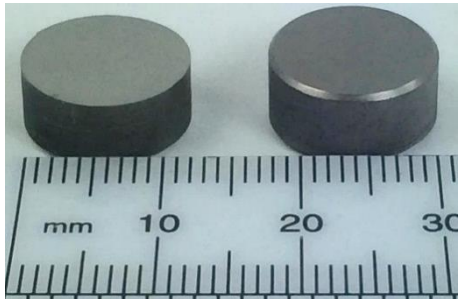

Figure 10. Photograph of alloy 617 coupons before (left) and after (right) undergoing the aluminization process for 36 hours at 800 °C.

3.3.2. Shot-peening

Shot-peening consists in bombarding a sample's surface with high-velocity metal beads. The process has been traditionally used for inducing compressive stresses in the near-surface regions of alloys to improve fatigue resistance, as well as for surface hardening. For this study, an additional goal was to refine grains in the near-surface regions to promote the formation of a superior oxide layer to mitigate high-temperature wear. In general, grain refinement is also known to mitigate exfoliation [38, 39, 40].

Grain boundaries are preferred paths for diffusion for certain elements and can play a beneficial role in terms of oxidation and corrosion. The diffusion coefficient along grain boundaries can be several orders of magnitude higher than that in the bulk lattice [39]. Thus, since the corrosion rate of alloys is dependent on the grain size [38], grain refinement is likely to foster the development of an oxide scale. In addition, shot peening makes the surface more uniform in terms of grain boundary distribution, making the oxide scale more uniform [38]. Since grain boundary diffusion of Cr cations controls the growth of Cr_2O_3,

and grain refinement favors Cr diffusion rather than Fe diffusion, more Cr_2O_3 is expected to form at the expense of Fe oxide [39, 40, 41]. Samples were shot peened with stainless steel beads at an outlet pressure of 4.1 bars for 30 and 75 seconds for alloy 800HT and alloy 617 respectively. Since the tribotests are conducted at elevated temperatures, recrystallisation also had to be considered.

3.4. Tribological testing

After conditioning, the samples were tested in a high-temperature pin-on-disk THT tribometer (CSM Instruments SA, now Anton Paar GmbH) to evaluate their tribological behavior. The tribometer, located at Argonne National Laboratory, Lemont, IL, was upgraded to reach temperatures up to 950 °C (see Figure 11). In addition, a custom ceramic heater (Zircar Ceramics, Inc.) containing a Kanthal A-1 wire was placed on top of the disk and around the pin to maintain a uniform ambient temperature for the disk and the pin. In order to protect the electronics, water-cooling lines were installed to ensure that the housing of the tribometer never exceeds 30 °C during high-temperature operation. The THT allows for adjustment of the load, the temperature, and the speed of disk rotation. The tribometer records the friction coefficient and the sliding distance continuously throughout the test.

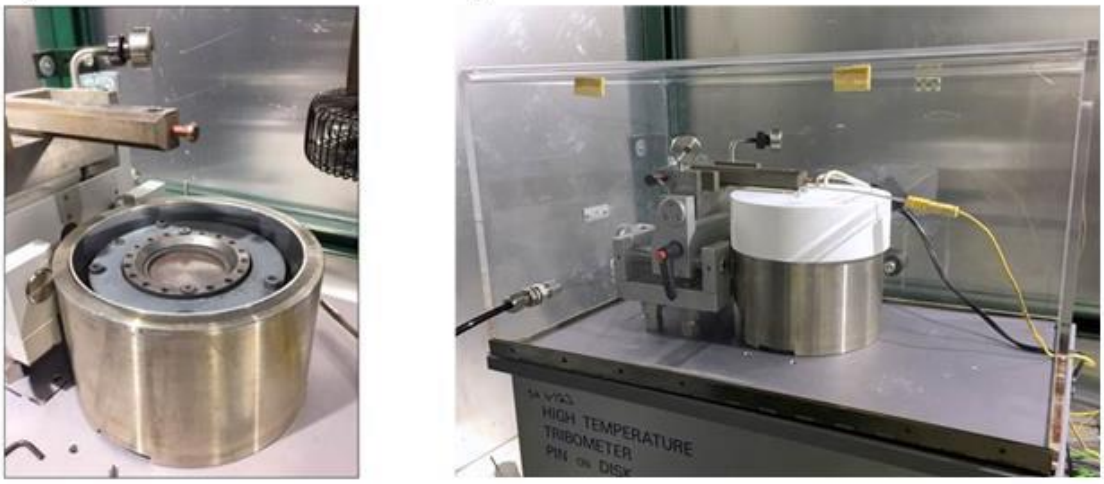

Figure 11: High-temperature pin-on-disk THT tribometer that was upgraded and used for tribotesting the candidate alloys at temperatures up to 900 °C.

Tribological testing of Incoloy® 800HT was performed at 650 °C and 750 °C in air and testing of Inconel® 617 was performed at 850 °C and 900 °C in air, for a period of 1 hour per test. The testing temperatures were selected based on the mechanical and corrosion performance of these alloys at high temperature. A testing period of 1 hour was selected as to exceed the run-in period, not induce a significant surface oxidation during the tests, and to conduct the tests in a reasonable period of time that would provide an accurate determination of the steady-state friction coefficient. Three different loads (1, 2 and 5 N) combined with three different radii of curvature (16.3, 55.3 and 255.4 mm respectively) were selected in order to investigate the effects of load/contact stress (~30, ~65, and ~120 MPa respectively) on the wear mechanisms (see Appendix 1 for details regarding the contact-stress calculations). It is crucial to acknowledge the importance of friction heat as well as surrounding heat when choosing the different testing parameters [23]. Since sliding speeds lower than 0.1 m/s are unlikely to trigger oxide melting even at 900 °C [31], a

sliding speed of 10 cm/s was selected in order to maximize the number of wear cycles for each run. Upon completion of a test, the samples were allowed to cool passively, and subsequent analyses were conducted on the pin and disk to characterize the wear behavior.

Preliminary as-received metal-on-metal tribological tests were performed with 800HT samples in an inert argon environment to investigate potential oxide formation during the 1 hour of high-temperature exposure of the tribotests in air. However, due to the enclosure system of the THT, the moisture level was unable to be maintained such that oxidation of samples was prevented. In comparison, the thickness of the oxide layer formed on the unworn regions due to testing in ambient air was approximately 600 nm. This upper bound on the degree of oxide growth within worn regions during testing indicates that oxidation during tribotesting may therefore play a role in the tribological behavior of the samples. Yet, the oxidation was not significant enough to prevent galling in the metal-on-metal cases (see Section 4.1). Thus, the unconditioned results presented in Section 4 represent lower bounds on the severity of metal-on-metal wear under inert testing conditions.

3.5. Characterization

Multiple characterization and measurement techniques and post-process analyses were employed to evaluate the corrosion behavior and wear performance of both alloys under different conditioning regimes and surface treatments. Scanning electron microscopy (SEM) (Carl Zeiss AG) was used to perform cross-sectional imaging of the conditioned samples to measure the thicknesses of the corrosion-product layers and to study the

morphology of the wear tracks. In conjunction with electron dispersion spectroscopy (EDS), it was also used to determine qualitatively the chemical compositions of the different oxides and other surface layers that formed on the samples. Finally, it also helped determine the composition of the wear tracks and provided information regarding the wear performance of the different surfaces. A custom Matlab program was used to generate composite EDS maps to identify bands of distinct chemistry within the aluminized samples. The program loads a series of EDS images that quantify the atomic percentages of individual elements found within the sample, and the program produces a single map that displays the spatial distribution of individual elements or combinations of individual elements, depending on the user's selection. The user chooses thresholds that define the minimum concentrations of the elements and/or element combinations to be displayed, and the map produced is color coded to display the regions of the sample that contain the elements or element combinations that are present at concentrations above those thresholds.

A scanning white-light interferometer (Zygo Corporation) was used to obtain the topography of the wear tracks and subsequently compute the wear volumes for each tribological test. Values for the wear volume were determined by quantifying the volume of material removed from two locations on the wear track of the disk (i.e., the volume of material missing below the surface plane of the disk), averaging those volumes, extrapolating those volumes over the full circumference of the wear track, and then

normalizing that volume by the circumference of the track. For all tribotests conducted for this study, the majority of the wear process is considered to take place during the run-in period. The uncertainty in the wear volume is calculated using the propagation of error approach, using the standard deviation of the two volume measurements and the uncertainty in the measurement technique itself due to the background roughness of the unworn surface.

X-Ray Diffraction (XRD) (Bruker D8 Discover) was used to qualify the phases on the surface of samples. In particular, it was very beneficial in identifying the intermetallic phases formed on the aluminized samples and the potential presence of carbides in Kolsterised samples. Glow-Discharge Optical Emission Spectroscopy (GDOES) (HORIBA, Ltd.) was used to quantify the elemental profile of samples. Since this technique is well calibrated to measure carbon content, it was especially used to measure the composition of Kolsterised samples. The measurements were performed at 700 Pa and 40 W with an average erosion rate of 0.0783 ± 0.060 μm/s for 800HT and 0.0957 ± 0.0018 μm/s for 617, respectively.

The THT tribometer, in addition to inducing accelerated wear, also provided in situ measurements of the friction coefficient as a function of time with an acquisition frequency of 11.1 Hz. After noise filtering, both the initial friction coefficient and the steady-state friction coefficient were obtained by averaging the values of the friction coefficient over

the first ten cycles and after the run-in period, respectively. These values provided information regarding the severity of the sliding contact at the initial stages and after run-in. It also allowed to identify the time duration of the run-in period before friction values settle down to a steady-state value.

Microhardness measurements were conducted using a Vickers microhardness tester (Buehler) using a 50 g load to quantify the hardness profile of both alloys after shot peening which is expected to increase the hardness of the samples. Additionally, nanohardness measurements using a TI 950 TriboIndenter (Hysitron, Inc.) with a diamond Berkovich tip were performed to evaluate the hardness of the tribolayers formed in the wear tracks of the samples as well as the hardness of the glaze-oxide layer which plays a crucial role in dictating the high-temperature tribological behavior of the alloys. Coupons were mounted in Bakelite (Buehler Ltd.) and polished at 320, 600, 800, and 1200 grit Si-C paper with a final 1μm diamond paste polish. The area function of the Berkovich tip was calibrated with a quartz reference to ensure the accuracy of individual measurements within 10% of the reference values Er = 69.6 GPa and H = 9.25 GPa. In order to obtain accurate statistics, an array of indents consisting of a variable number of rows and 15 columns was placed into each sample, with 5 different maximum-load levels chosen – 800 μN, 2600 μN, 4400 μN, 6200 μN or 8000 μN. Each maximum-load level was reached 3 times per row, and hardness results for a particular depth into the sample was quantified by averaging the 15 hardness values measured at that given depth. Indents were separated by between 3 and 6 μm to

ensure that results were not affected by previous indents. Indentation curves that exhibited characteristics of contamination between the tip and sample were excluded from the analysis. To correct for any errors due to potential global tilting of the sample, the residual areas of 4 or 5 indents per sample were measured using calibrated SEM images of the indents, and a correction factor was applied to each area function. Final hardness values were then calculated by taking the max indentation load and dividing that by the area-corrected area of the indent.

4. RESULTS

In this section, corrosion and tribological results will be presented for the two alloys and in the four regimes. Corrosion results will be assessed via cross-sectional SEM/EDS and GDOES elemental analysis of the conditioned alloys. These results will give information on the corrosion resistance of both alloys and provide indications regarding the potential wear resistance of the samples.

The tribological behavior of the samples will be qualified via top-down SEM/EDS morphological and compositional analysis, as well as topographical analysis of the wear tracks via optical profilometry. Wear volumes and initial friction coefficient values will be reported as a function of the corrosion and testing conditions to investigate correlations between the measured quantities and the wear mechanisms.

4.1. Regime I, II and air

4.1.1. Corrosion results

Figure 12 and Figure 13 show cross-sectional SEM images and EDS line scans of as-received 800HT and 617, respectively. As expected, the concentration profiles are uniform with high levels of Fe, Ni and Cr for alloy 800HT and of Ni, Cr, Co and Mo for 617.

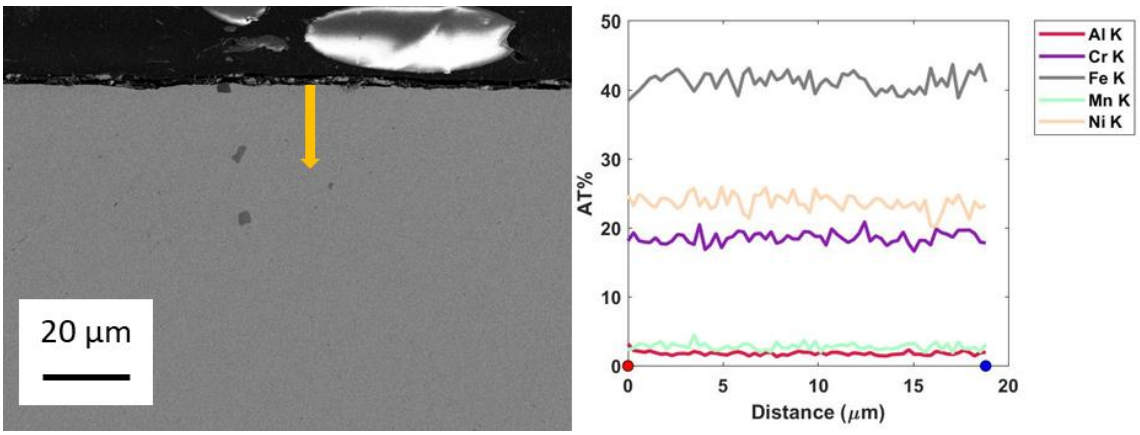

Figure 12: Cross-sectional SEM image and EDS line scan of as-received 800HT alloy.

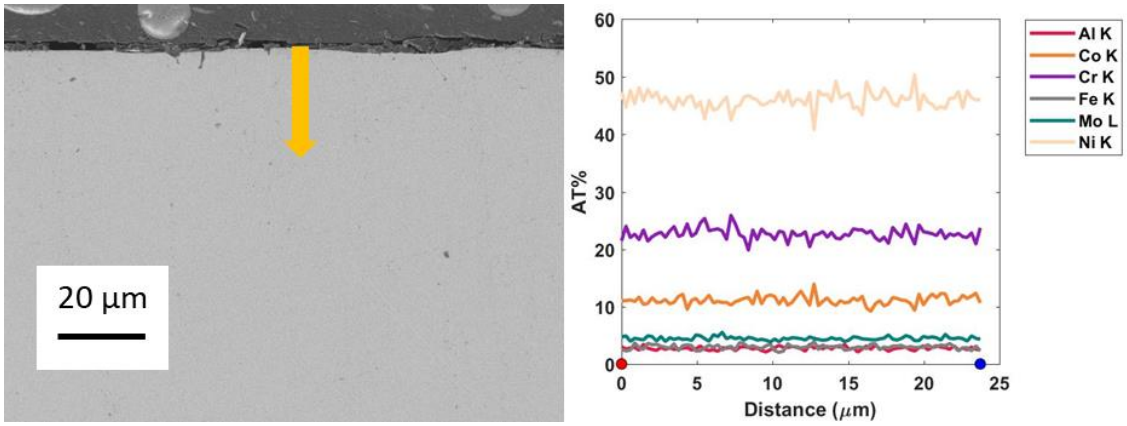

Figure 13: Cross-sectional SEM image and EDS line scan of as-received 617 alloy.

After conditioning the alloys in Regime II and in air, cross-sectional SEM imaging and EDS line scans were obtained on the samples to investigate the thickness and the character of the oxidation.

Figure 14 shows the formation of a slightly manganese-enriched chromium oxide on alloy 800HT after conditioning in Regime II for 22 days at 750 °C. Additionally, a thin internal aluminum oxide formed along the grain boundaries. The thickness of the oxide scale was measured to be 1.33 ± 0.44 µm.

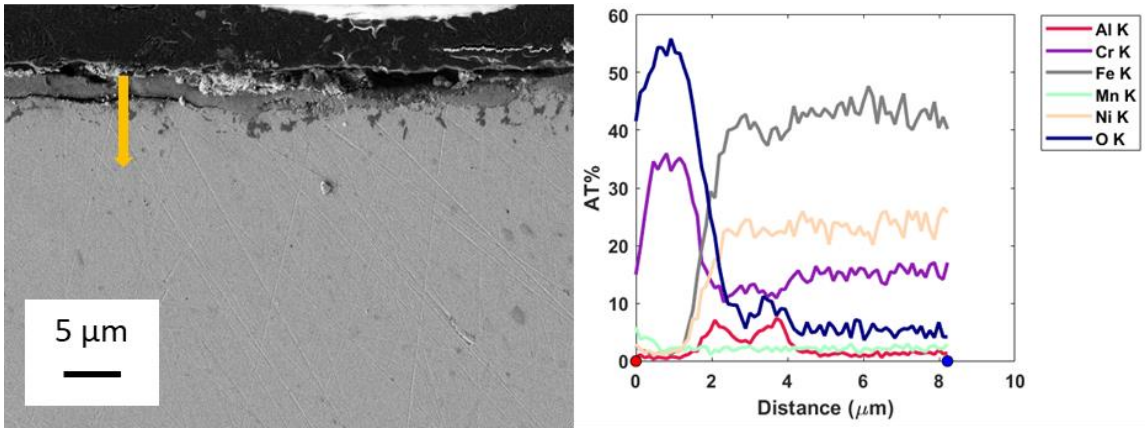

Figure 14: Cross-sectional SEM image and EDS line scan of alloy 800HT conditioned in Regime II.

The cross-sectional image and composition of alloy 617 after conditioning in Regime II for 22 days at 900 °C are presented in Figure 15. A chromium oxide formed on the surface with a thickness of 1.00 ± 0.20 µm, with a deep internal aluminum oxide developing at the grain boundaries [18]. Additionally, it appears that a thicker chromium oxide (3.50 ± 0.17

μm) also formed on the surface along the grain boundaries, making the surface non-uniform.

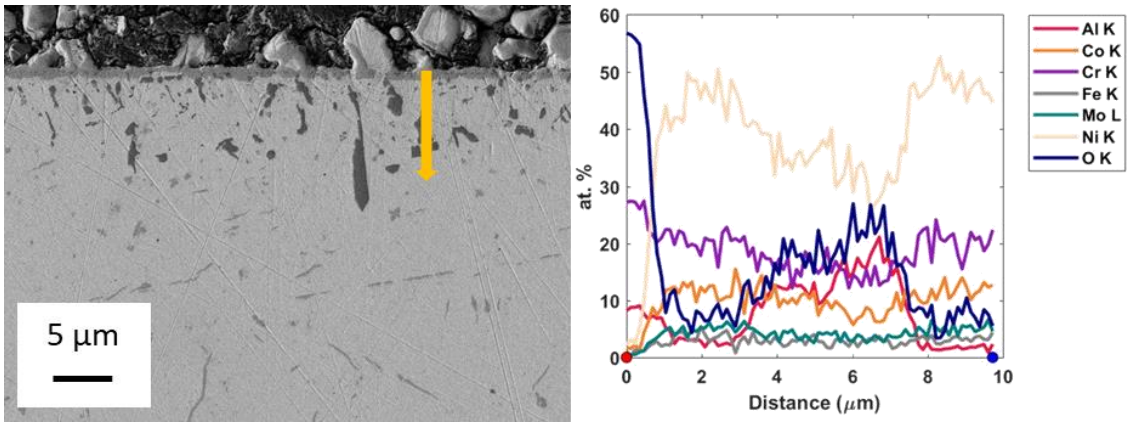

Figure 15: Cross-sectional SEM image and EDS line scan of alloy 617 conditioned in Regime II.

Figure 16 presents the cross-sectional image and composition of alloy 800HT after conditioning in air for 20 days at 750 °C. Exposure to air at high temperature triggered the formation of a non-uniform oxide on the surface. 20-μm-thick patches of external iron oxide coupled with the internal Ni-Cr oxide are surrounded by a thin chromium oxide layer. This phenomenon will have an impact on the tribological behavior of samples conditioned in air. Because the exposure temperature is higher than 400 °C, the iron oxide likely consists in Fe_3O_4 and Fe_2O_3 with FeO [15].

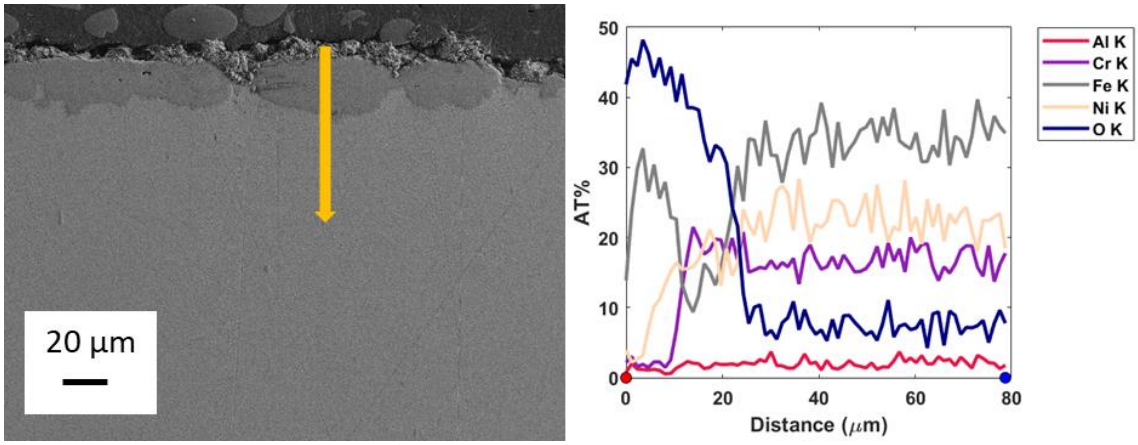

Figure 16: Cross-sectional SEM image and EDS line scan of alloy 800HT conditioned in air at 750 °C.

The cross-sectional image and composition of alloy 617 conditioned in air for 20 days at 900 °C are shown in Figure 17. The chromium oxide that developed is thicker (4.63 ± 0.68 µm) than that formed in Regime II, but oxide growth at grain boundaries is not as apparent on the surface. Internal aluminum oxidation along grain boundaries is still observed. Additionally, some internal titanium precipitates are visible near grain boundaries.

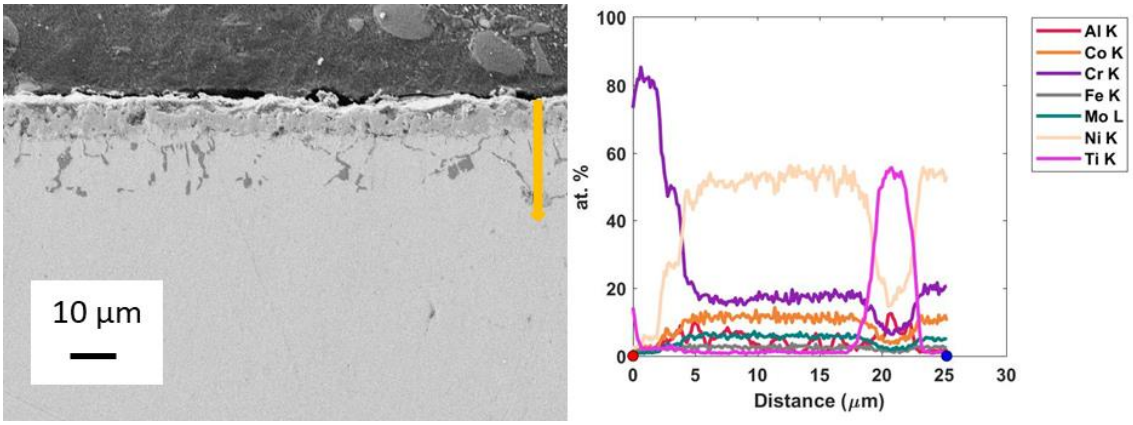

Figure 17: Cross-sectional SEM image and EDS line scan of alloy 617 conditioned in air at 900 °C.

The corrosion mechanisms of alloys 800HT and 617 have been extensively studied, and the results presented in this study are consistent with those found in the literature [12, 15, 22, 41].

The oxide thicknesses were measured from the SEM images to quantify the evolution of the oxide. Curve fitting of the data was performed assuming parabolic oxidation behavior [15, 22] to capture the general trends in oxide thickness as a function of exposure time. Figure 18 shows the plots of oxide thickness versus time for both alloys.

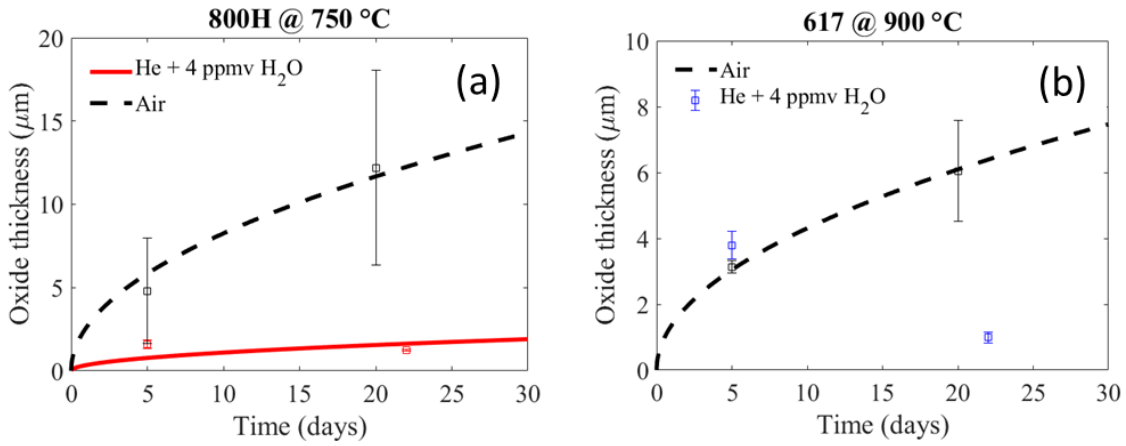

Figure 18: Evolution of oxide thickness as a function of exposure time for (a) alloy 800HT at 750 °C and (b) alloy 617 at 900 °C.

The parabolic fits to the oxide layer growth for alloy 800HT capture the general trends correctly. However, the evolution of oxide thickness for alloy 617 conditioned in Regime II does not follow a clear trend. In this case, the oxide thickness measured after 5 days was thicker than that measured after 22 days of high-temperature exposure. Previous research measuring the evolution of the weight change in alloy 617 at 1100 °C indicates that such behavior can happen because of spallation and vaporization of chromium oxides during extended exposure [15].

4.1.2. Tribological test results

Figure 19 and Figure 20 present the morphology of wear tracks for as-received samples of both alloys 800HT and 617.

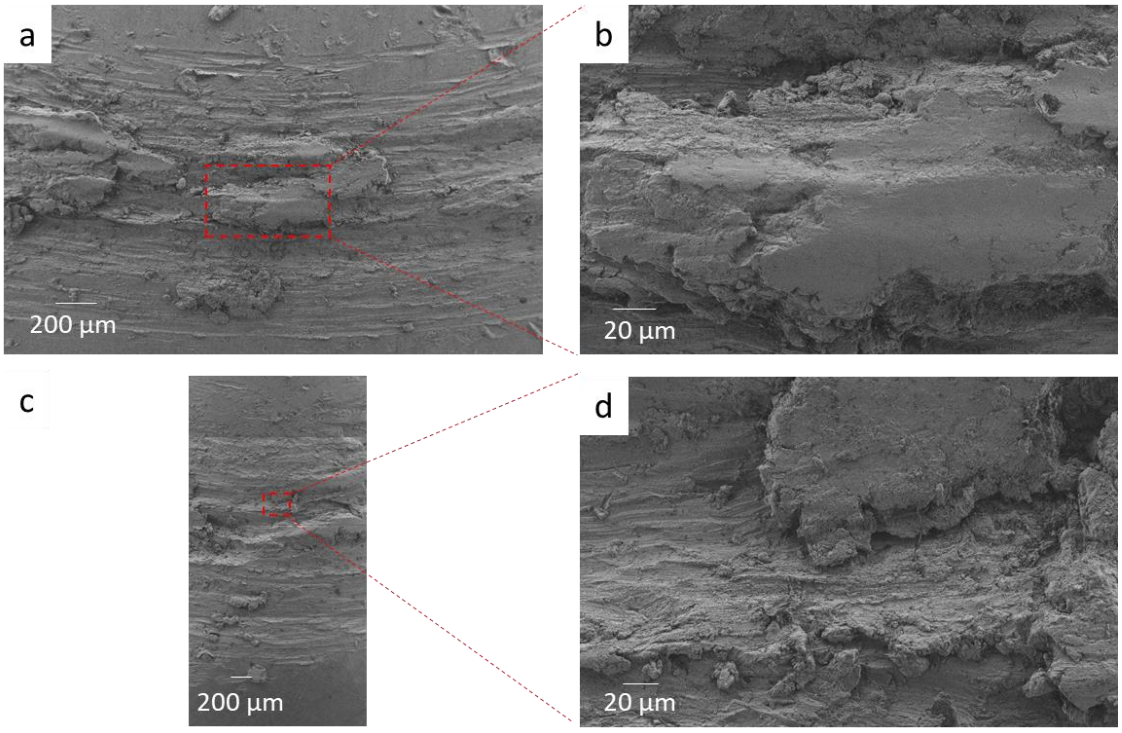

Figure 19: Morphology of the as-received 800HT wear tracks for (a, b) a 1N load at 750 °C and for (c, d) a 5N load at 750 °C.

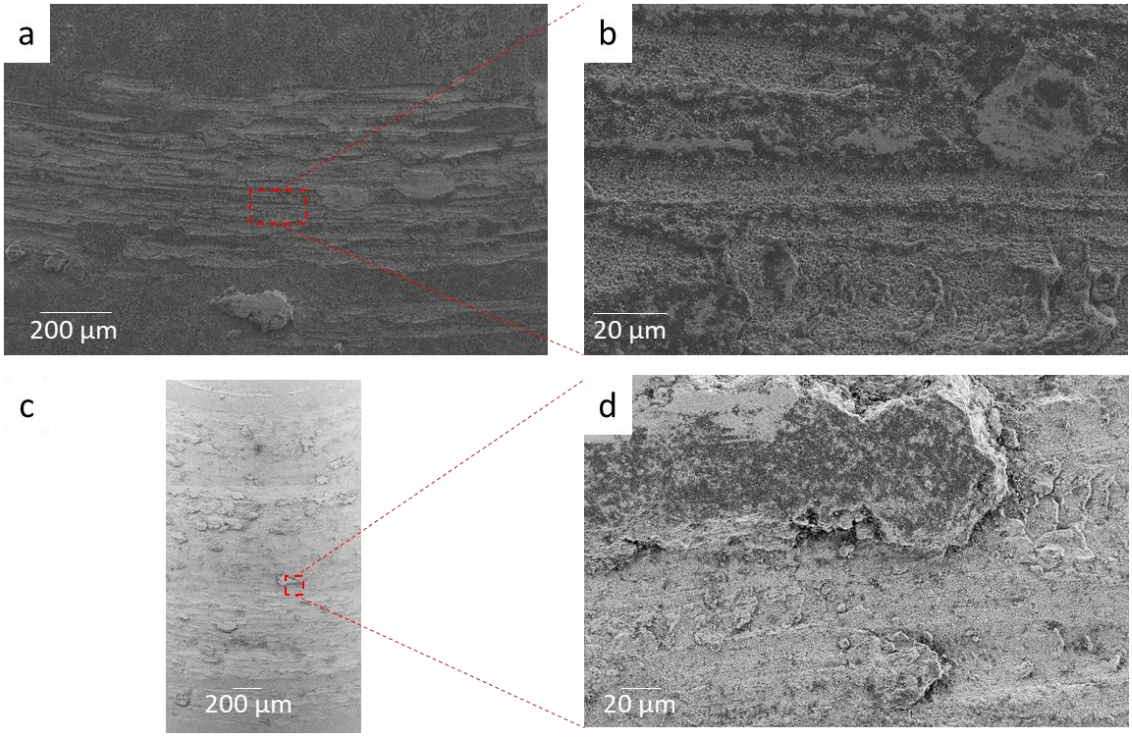

Figure 20: Morphology of the as-received 617 wear tracks for (a, b) a 1N load at 850 °C and for (c, d) a 5N load at 850 °C.

In terms of wear mechanisms, scuffing and gouging were present at both loads and no evidence of oxide compaction is present. These mechanisms appear more severe for alloy 800HT and are accompanied with debris formation.

Figure 21 and Figure 22 present elemental composition of the wear tracks and the background of the tribotested as-received samples.

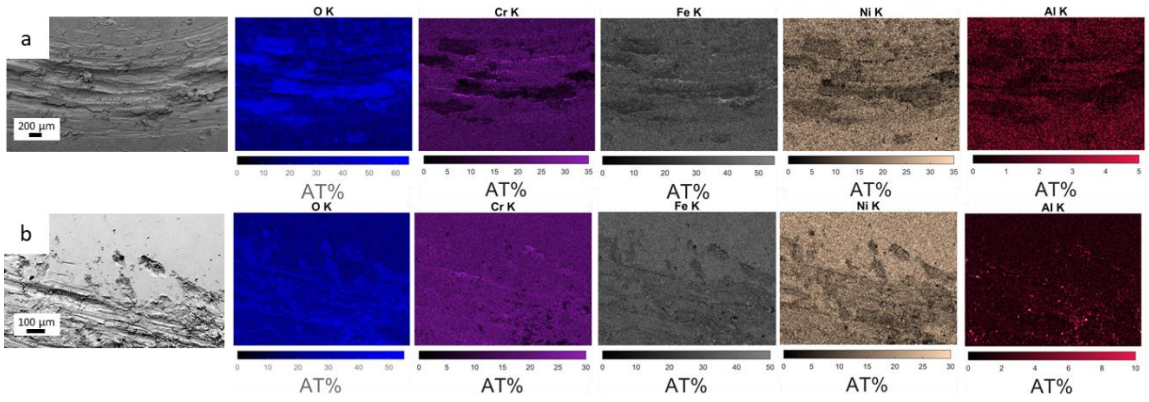

Figure 21: Top-down SEM and EDS maps of as-received 800HT wear tracks after (a) 1N wear testing at 750 °C and (b) 5N wear testing at 750 °C.

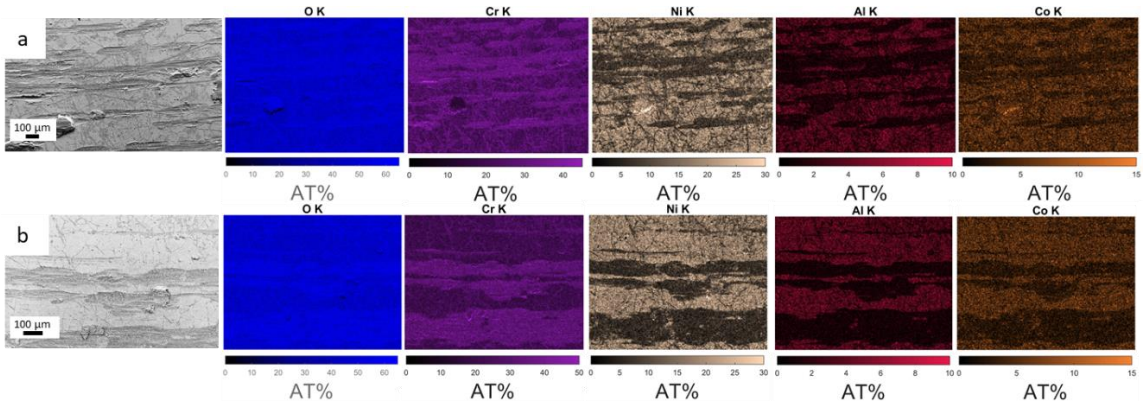

Figure 22: Top-down SEM and EDS maps of as-received 617 wear tracks after (a) 1N wear testing at 900 °C and (b) 5N wear testing at 900 °C.

Due to the broken bonds, the debris are reactive and will oxidize to form an oxide in the wear track: a chromium oxide for 617 and a mixed chromium/iron oxide for 800HT. A thin oxide likely formed on the background of the samples, but it is not thick enough to be detected by EDS, hence the bulk-like composition outside of the wear tracks for both alloys. The elevated aluminum content in the background of the samples for alloy 617 is noted as well.

As the debris build up in the wear track, the local stress will decrease until the sliding contact runs in and gouging is stopped. The run-in periods appear to be longer for 800HT than 617. Additionally, the profilometry results presented in Figure 23 indicate that the wear is less severe for 617 than for 800HT. These observations are supported by wear volumes and initial friction coefficient volumes indicating a more aggressive sliding contact for 800HT as presented in Figure 24.

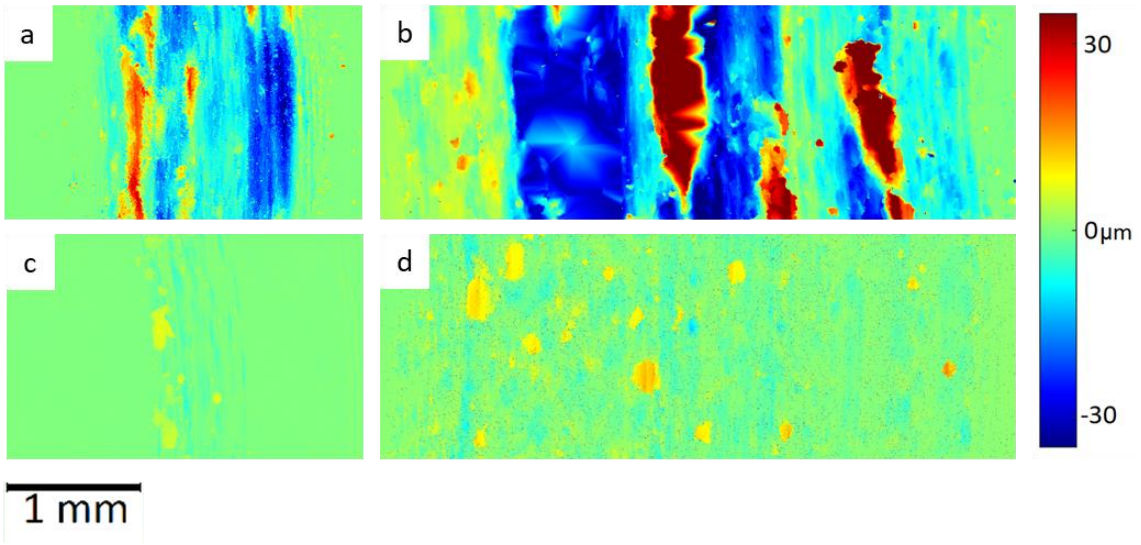

Figure 23: Wear track profilometry for (a, b) as-received 800HT tested at 1N, 750 °C and 5N, 750 °C, respectively, and (c, d) as-received 617 tested at 1N, 900 °C and 5N, 900 °C, respectively.

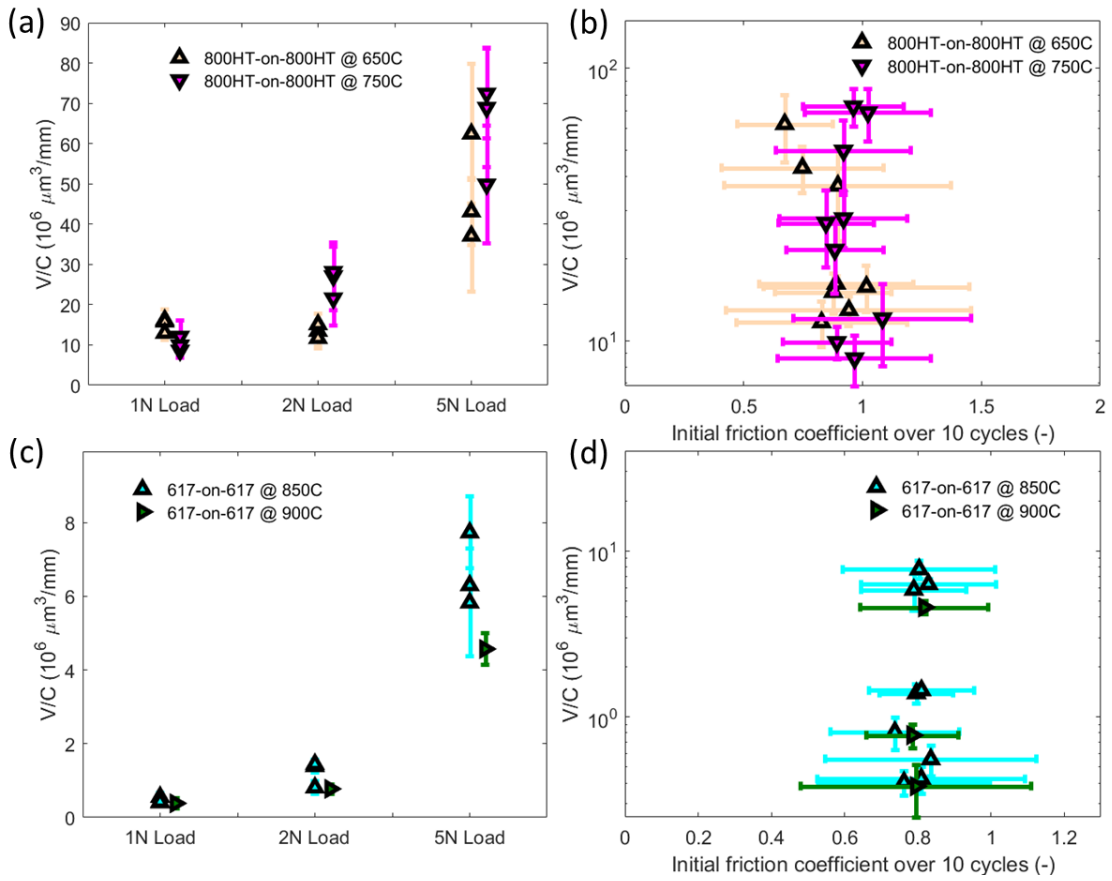

Figure 24: Wear volumes as a function of load (a, c) and initial friction coefficient (b, d) for as-received self-mated 800HT and 617 tested at elevated temperatures.

The increase in wear volumes as a function of load is expected. Alloy 800HT presents order-of-magnitude higher wear volumes and initial friction coefficients approximately 12% higher than those of 617 (0.9037 ± 0.1264 and 0.7976 ± 0.0662, respectively). In addition, despite different wear volumes, all tribotests present similar initial friction coefficients for both alloys, which supports the idea that wear mechanism is the same at all loads for both alloys.

Non-self-mated sliding of the alloys was also tribotested: 800HT pins were slid against 617 disks. The wear volumes results presented in Figure 25 show intermediate values between those of self-mated tribotests of as-received samples.

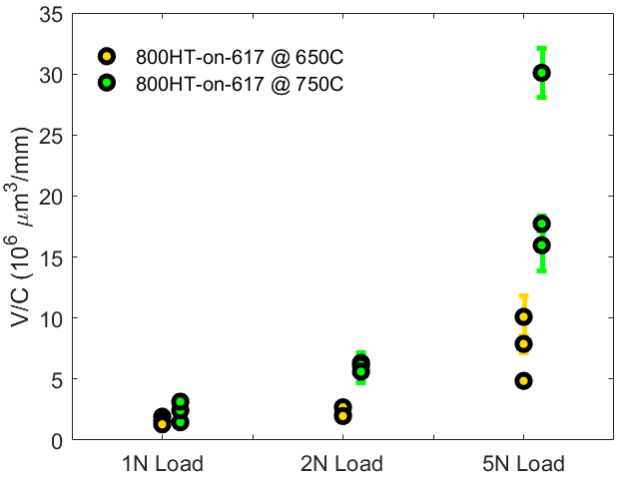

Figure 25: Wear volumes as a function of load for the as-received 800HT-on-617 tested at elevated temperatures.

Since the objective of this study is to evaluate the impact of corrosion on the tribological behavior of both alloys, samples that were conditioned in Regime II and in air were tribotested using the same tribological testing parameters as those for as-received samples. Figure 26 and Figure 27 present the morphology of wear tracks for alloys 800HT and 617 after conditioning in Regime II for 22 days at 750 °C and 900 °C, respectively.

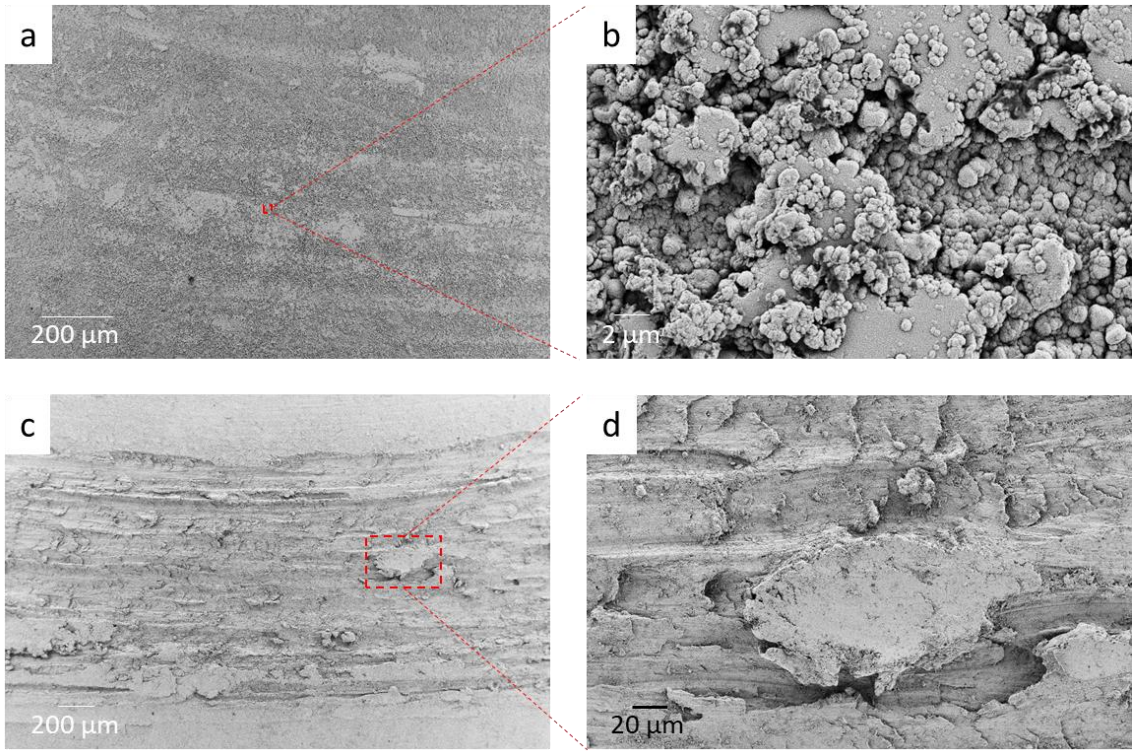

Figure 26: Morphology of 800HT wear tracks after conditioning in Regime II for (a, b) a 1N load at 750 °C and for (c, d) a 5N load at 750 °C.

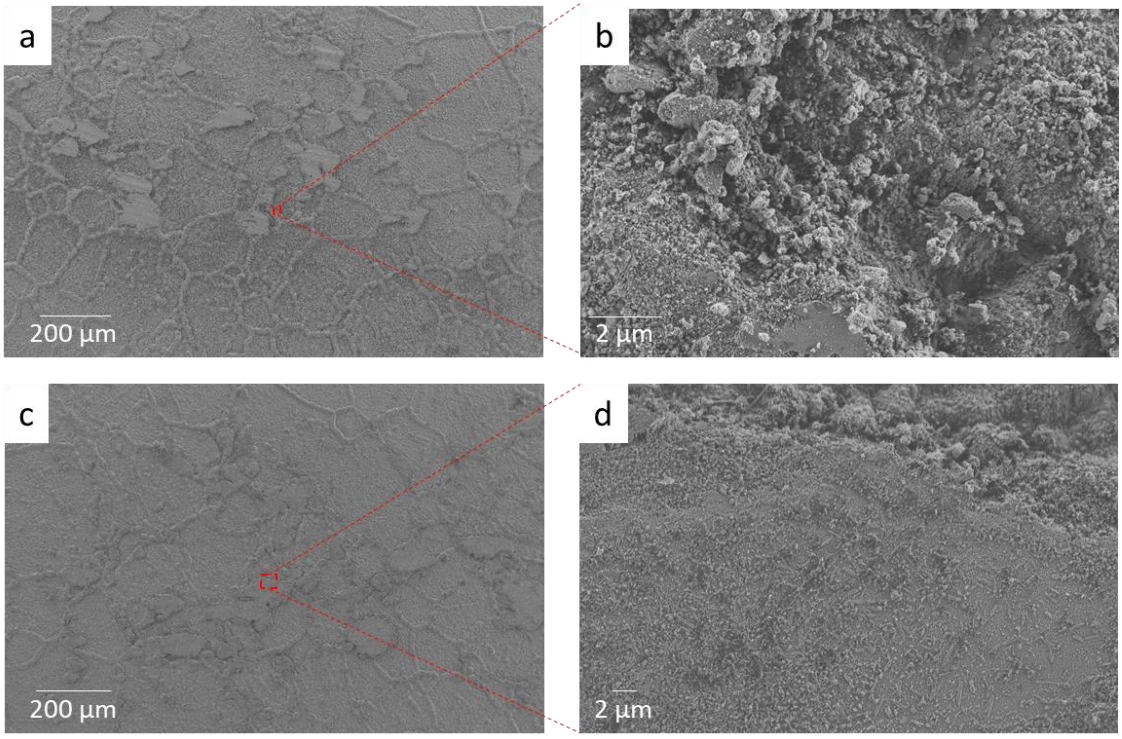

Figure 27: Morphology of 617 wear tracks after conditioning in Regime II for (a, b) a 1N load at 850 °C and for (c, d) a 5N load at 850 °C.

For alloy 800HT, the glaze layer visible in Figure 26 (b) formed at 1N and 2N loads and in two out of seven high-load cases. The remaining samples tested at 5N presented severe oxide breakthrough and scuffing as shown in Figure 26 (c, d). A glaze layer with a similar morphology formed on alloy 617 for all tribotests except for one test at higher load. Figure 26 and Figure 27 also show that the area fraction covered by the glaze layer is lower for 617 than for 800HT. This observation is consistent with the enhanced oxide growth at the grain boundary for alloy 617 which forms higher load-bearing areas as seen in Figure 27 (a, c). The morphologies of these wear tracks indicate that alloy 617 follows the first mechanism of glaze formation as described in Section 2.2.2 due to its high-temperature

strength. Alloy 800HT follows the second mechanism of glaze formation at low load since the area fraction covered by the glaze indicates that some deformation occurred. At higher load, when no glaze-oxide layer developed, alloy 800HT follows the third mechanism where further deformation of the sub-surface occurred. Also, it appears that the threshold load that enables the formation of glaze layer is about 5 N for alloy 800HT. This value is much lower than the one presented in reference [29].

In terms of composition, while the EDS cross-sectional line scan presented a chromia layer on the surface for both alloys, the exposure to air during the test triggered the formation of a patchy Fe-Ni oxide on top of alloy 800HT, as seen outside the wear tracks in Figure 28 (a). Figure 29 indicates that for alloy 617, the background is still composed of a chromium oxide, which is consistent with the EDS cross-section line scan after air exposure.

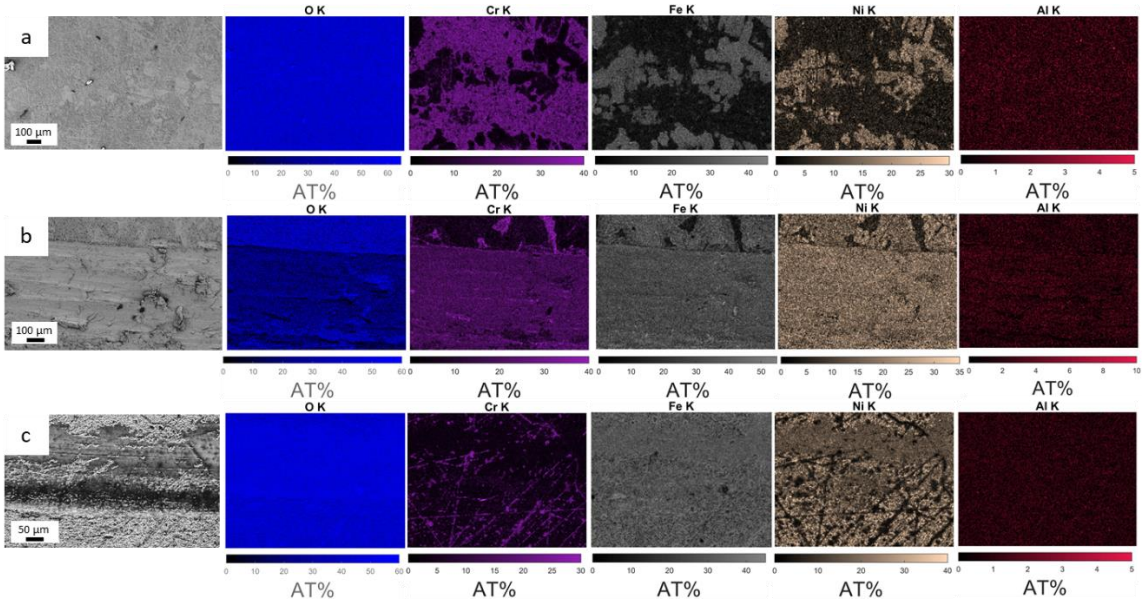

Figure 28: Top-down SEM and EDS maps of 800HT wear tracks after conditioning in Regime II for (a) a 1N load at 750 °C, (b) a 5N load at 750 °C revealing oxide breakthrough and (c) a 5N load at 750 °C revealing glaze-oxide layer formation.

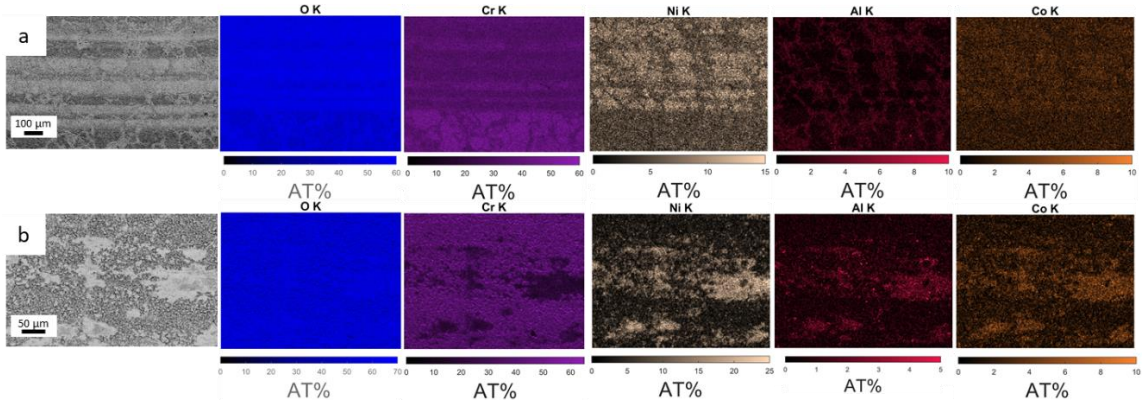

Figure 29: Top-down SEM and EDS maps of 617 wear tracks after conditioning in Regime II for (a) a 1N load at 900 °C and (b) a 5N load at 900 °C.

Figure 28 (a, c) provide evidence that the glaze layer formed on alloy 800HT consists of Ni-Fe oxide that developed on top of the pre-existing oxide. Nanohardness measurements of the glaze layer indicate a drastically higher value in hardness compared to as-received

material: 14.7 ± 0.9 GPa versus 4.9 ± 0.3 GPa, respectively. At higher load, when the oxide was broken through (as seen in Figure 28 (b)), the analysis revealed bulk-like composition. For alloy 617, Figure 29 (a, b) shows that the glaze layer developed is not continuous and is present in patches along the wear track. Figure 27 indicates that the patches tend to follow grain boundaries. The patches show the presence of an oxide with the same metallic proportions as those of the bulk material. This composition has been observed for alloy 617 [16] since, at high temperature, the glaze forms via complex oxide like $NiCr_2O_3$. Again, the hardness of the glaze is much higher than that of the as-received material: 13 ± 2 GPa versus 6.7 ± 0.5 GPa, respectively.

Profilometry results shown in Figure 30 indicate much less severe wear than that of Regime I for both alloys when glaze formed, but only slightly at high load when the oxide was broken through.

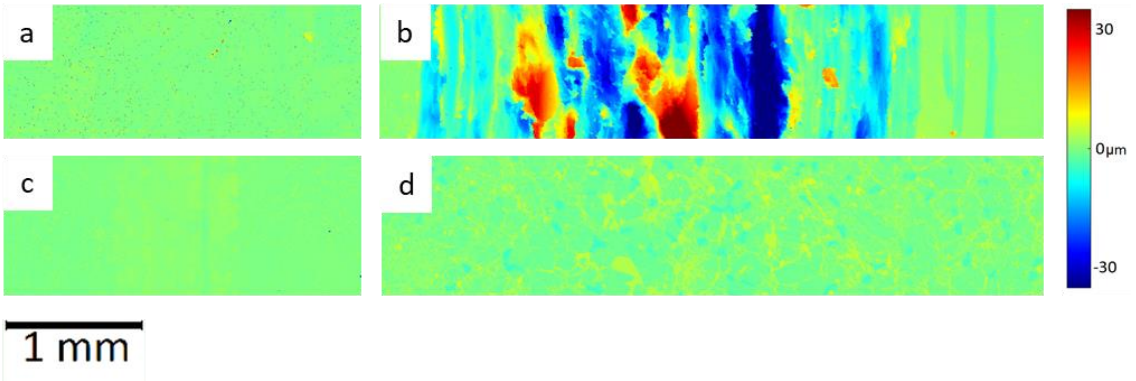

Figure 30: Wear track profilometry for (a, b) 800HT conditioned in Regime II and tested at 1N, 750 °C and 5N, 750 °C, respectively and (c, d) 617 conditioned in Regime II and tested at 1N, 900 °C and 5N, 850 °C, respectively.

Wear volumes and initial friction coefficients presented in Figure 31 also indicate mitigated wear when a glaze layer formed, rendering the wear track nearly undistinguishable from the unworn background, and resulting in wear volumes below the detection limits of the technique. This is particularly visible for alloy 800HT at every load and alloy 617 at a 5N load. For alloy 800HT, when the oxide was broken through, the wear volumes and initial friction coefficients present similar values as those for as-received samples as shown in Figure 31 (b). This indicates that the oxide is crucial in the protective feature of the corrosion process, and the initial friction coefficient can serve as an indicator of the wear mechanism and the severity of the sliding contact.

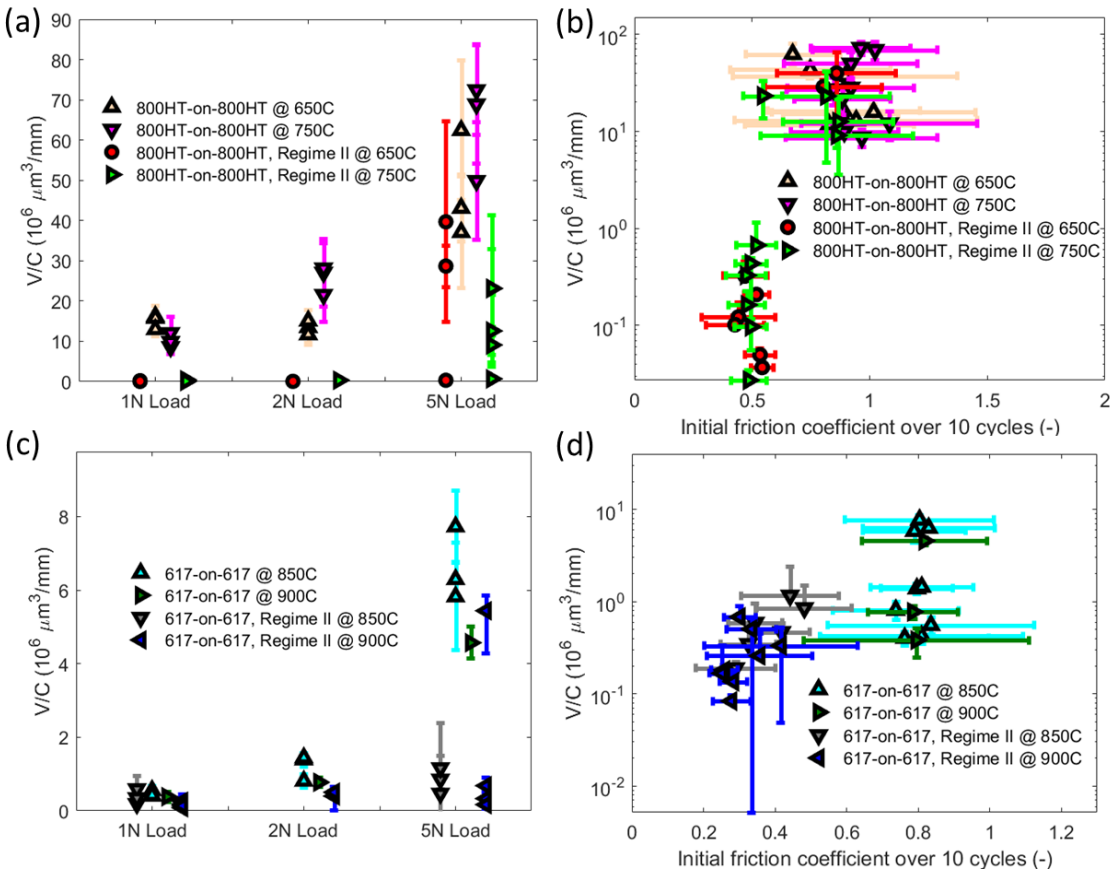

Figure 31: Wear volumes as a function of load (a, c) and initial friction coefficient (b, d) for self-mated 800HT and 617 both as-received and after conditioning in Regime II.

Samples conditioned in air for 20 days at 750 °C and 900 °C for alloys 800HT and 617, respectively were also tribotested in order to compare their behavior with those of samples conditioned in Regime II.

Figure 32 and Figure 33 present the morphology of the wear tracks for 800HT and 617 samples, respectively, after conditioning in air.

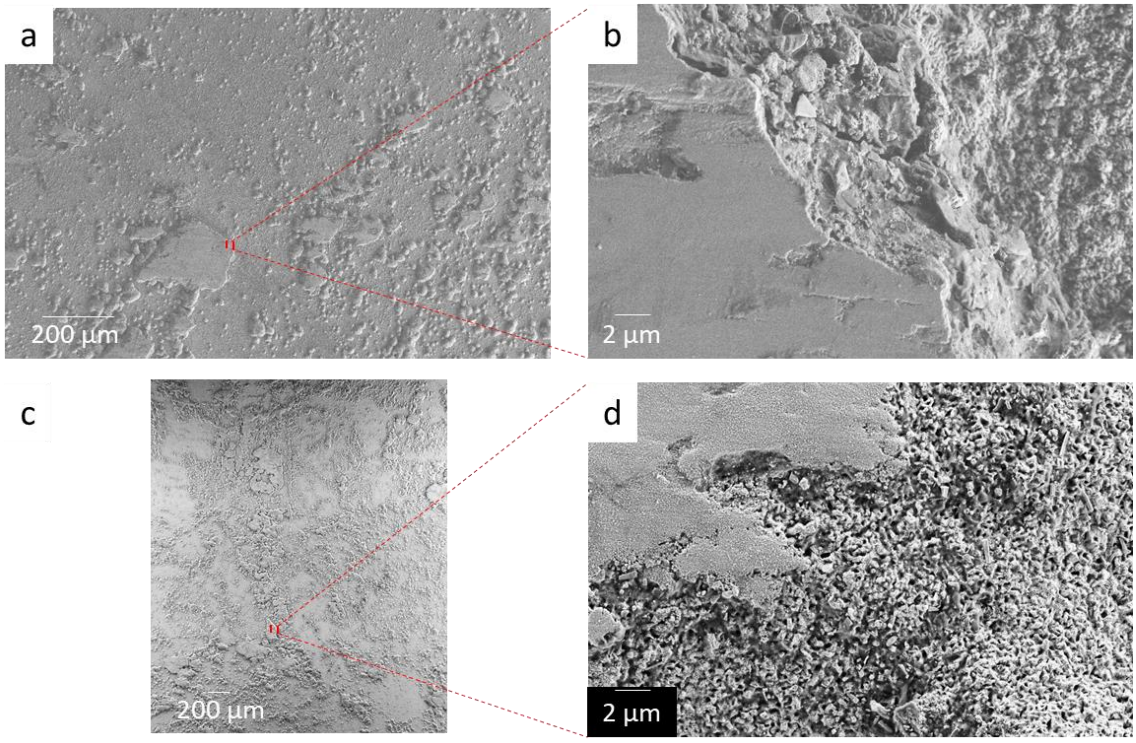

Figure 32: Morphology of the 800HT wear tracks after conditioning in air for (a, b) a 1N load at 750 °C for (c, d) a 5N load at 750 °C.

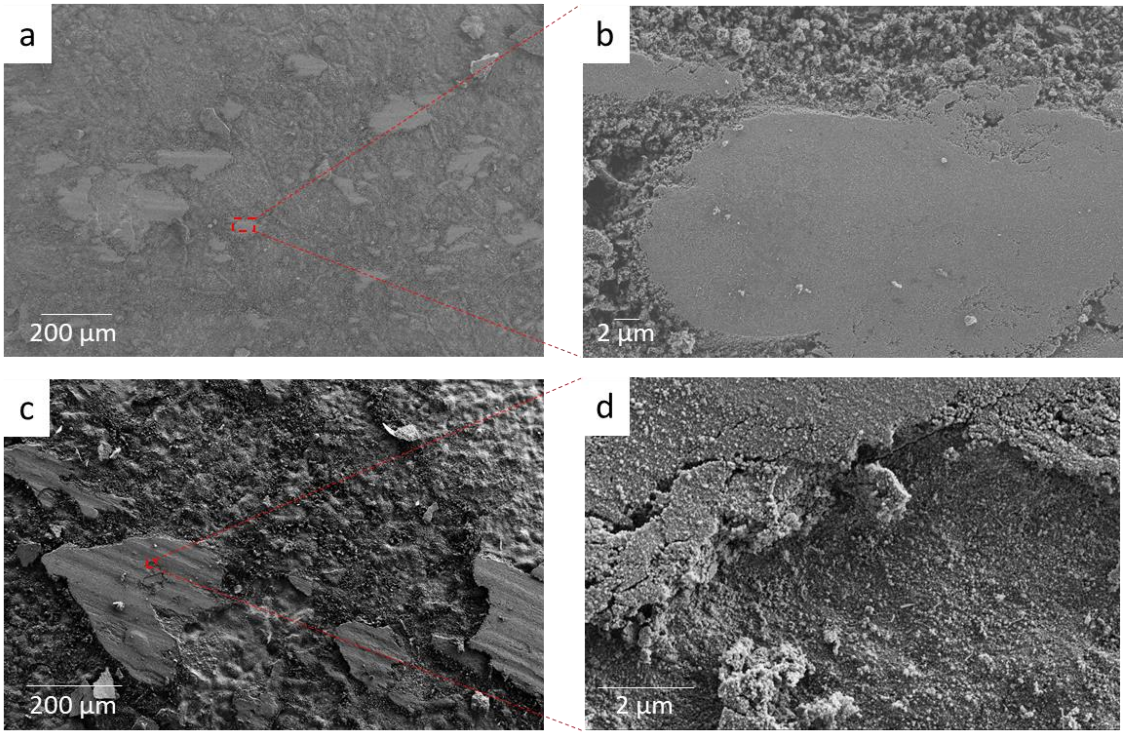

Figure 33: Morphology of the 617 wear tracks after conditioning in air for (a, b) a 1N load at 850 °C and for (c, d) a 5N load at 850 °C.

For alloy 800HT, the formation of iron oxide during the tribotest is much different than that of Regime II where a uniform chromium oxide was present across the entire surface. For samples conditioned in air, the presence of thick patches of oxide promoted the formation of a glaze layer at every load, except for a few cases at a 5N load, and caused its area fraction to be lower than that of Regime II samples. Since topographically higher areas are load-bearing, the composition of the glaze layer shows an iron-rich oxide as indicated in Figure 34.

For alloy 617, although it is difficult to identify the location of grain boundaries because of the high degree of oxidation, it seems the wear tracks consist in glaze patches located at grain boundaries for every load. Similar to Regime II, the composition of the glaze layer for alloy 617 presents the same metallic proportions as the bulk material as shown in Figure 35.

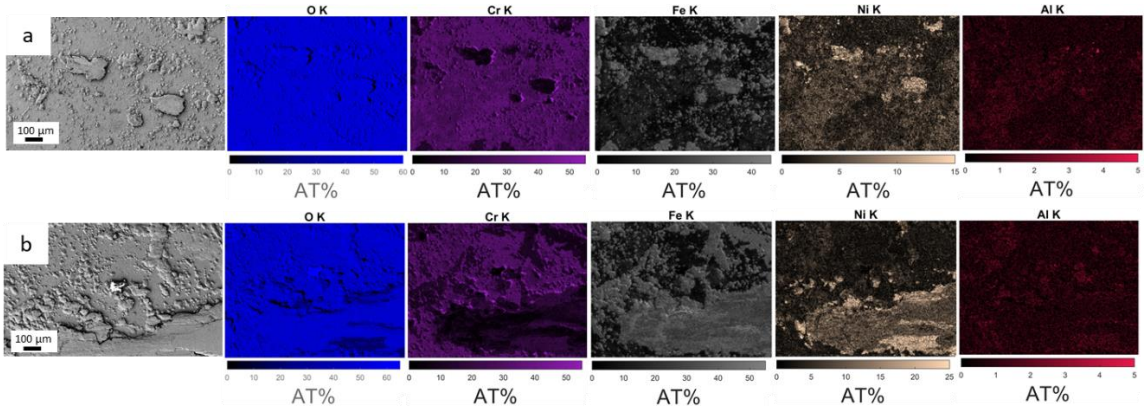

Figure 34: Top-down SEM and EDS maps of 800HT wear tracks after conditioning in air for (a) a 1N load at 750 °C and (b) a 5N load at 750 °C.

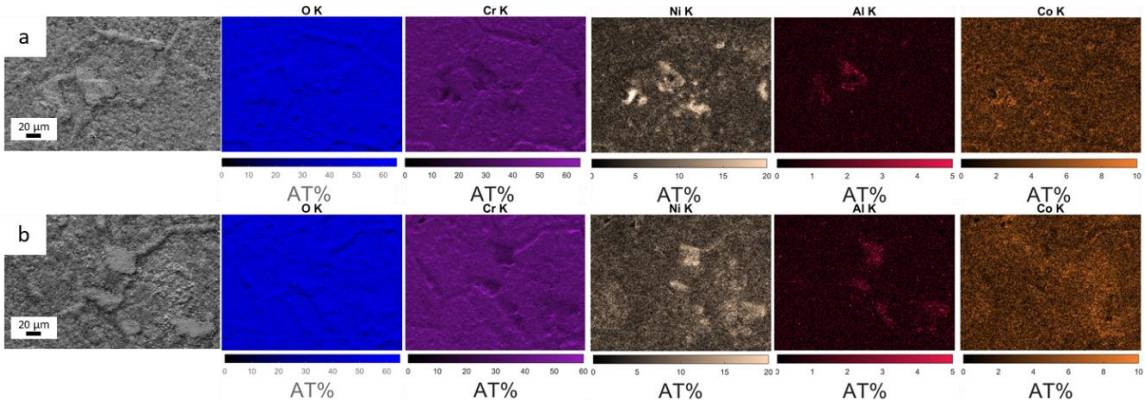

Figure 35: Top-down SEM and EDS maps of 617 wear tracks after conditioning in air for (a) a 1N load at 900 °C and (b) a 5N load at 900 °C.

Figure 36 presents the profilometry images for alloys 800HT and 617. For alloy 800HT, when a glaze layer formed, profilometry results indicate much less severe wear than Regime I but only slightly less severe when the oxide was broken through. Thick iron oxide patches are also visible in profilometry images. For alloy 617, these results do not indicate any difference in wear severity compared to that of Regime II. No sample conditioned in air presented oxide breakthrough even at high load, which supports the superiority of samples conditioned in air in terms of wear resistance.

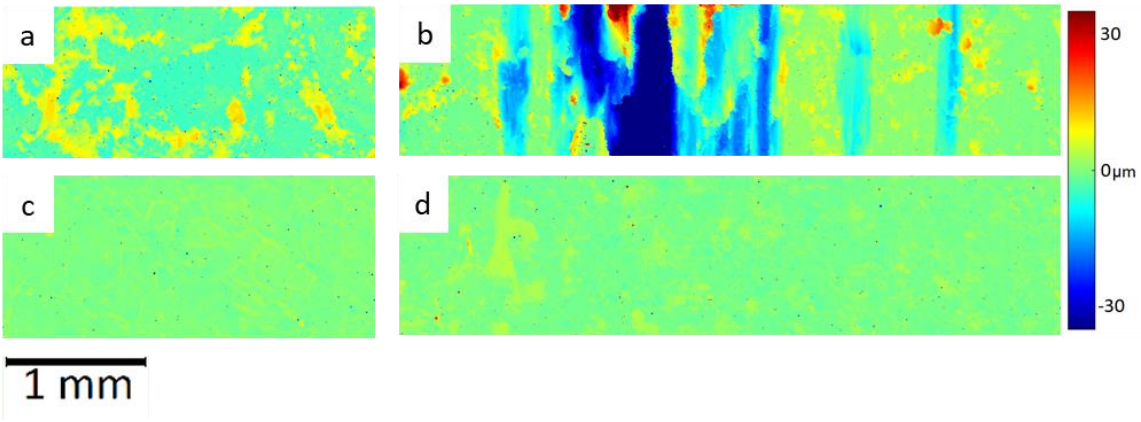

Figure 36: Wear track profilometry for (a, b) 800HT conditioned in air and tested at 1N, 750 °C and 5N, 750 °C, respectively and (c, d) 617 conditioned in air and tested at 1N, 900 °C and 5N, 900 °C, respectively.

Figure 37 presents the values of the wear volumes and initial friction coefficients for samples conditioned in Regime II and samples conditioned in air. For alloy 800HT, the initial friction coefficient values are higher than that of Regime II and slightly lower than that of as-received samples because the patches are spread and smoothened before the formation of the glaze layer. However, shorter run-in periods compared to Regime I (1689 ± 786 cycles) are consistent with much lower wear volumes when a protective layer

formed. For alloy 617, the glaze layer formation being similar to that of samples conditioned in Regime II, the wear volumes and initial friction coefficients values are also comparable with those of Regime II.

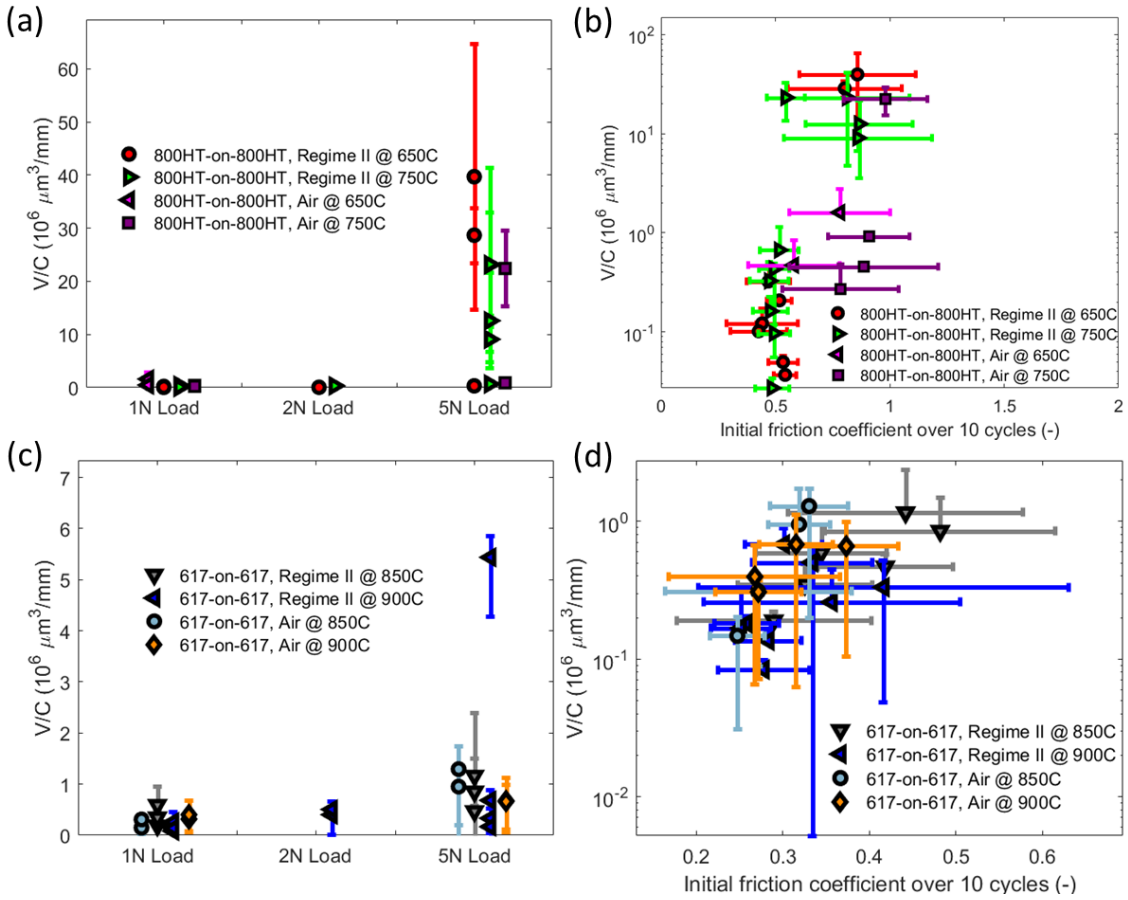

Figure 37: Wear volumes as a function of load (a, c) and initial friction coefficient (b, d) for self-mated 800HT and 617 conditioned in Regime II and conditioned in air.

Nanohardness of the 'glaze' formed on the surfaces of alloys 800HT and 617 after conditioning in Regime II was quantified via nanoindentation. The low wear rates of the oxidized alloys, relative to those of the as-received alloys, are attributed to the formation

of this ‘glaze’ that has found to be a protective, smooth, and compacted surface oxide. Figure 38 shows nanoindentation force-displacement curves used to quantify the elastic modulus and nanohardness of the low-wear glaze layer formed within the wear tracks of 800HT samples conditioned in Regime II and as-received 800HT. Results reveal that the nanohardness of the glaze is higher than that of the as-received surface by a factor of approximately three (14.7 ± 0.9 GPa versus 4.9 ± 0.3 GPa, respectively). The reduced elastic modulus of the low-wear glaze is slightly lower than that of the as-received sample (157 ± 6 GPa versus 200 ± 9, respectively).

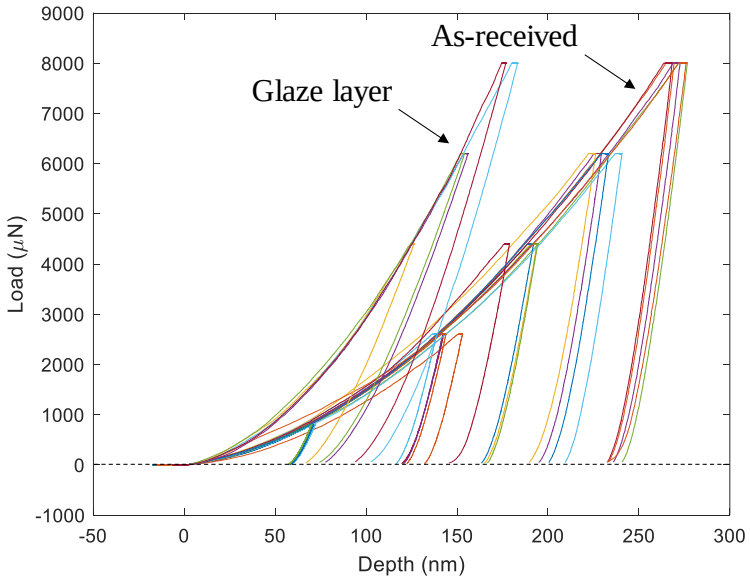

Figure 38. A series of nanoindentation force-depth curves obtained on the as-received surface of alloy 800HT and the low-wear glaze layer formed within the wear track generated by self-mated 800HT-on-800HT testing after conditioning the samples oxidizing conditions of Regime II. The increased hardness of the glaze is evident by the shallower depths of those curves compared to those of the as-received sample.

Figure 39 the shows nanoindentation force-displacement curves for as-received alloy 617 and the glaze formed on alloy 617 after wear testing in Regime II. The nanohardness of the 617 glaze is higher than that of the as-received surface by a factor of approximately two (13 ± 2 GPa versus 6.7 ± 0.5 GPa, respectively). The reduced elastic modulus of the low-wear glaze is slightly higher than that of the as-received sample (220 ± 30 GPa versus 200 ± 10, respectively). Compared to 800HT, the nanohardness of as-received 617 is higher than that of as-received 800HT (6.7 ± 0.5 GPa versus 4.9 ± 0.3, respectively), whereas their elastic moduli are effectively the same (200 ± 10 GPa versus 200 ± 9 GPa). The glazes formed on the alloys exhibit similar hardnesses (13 ± 2 GPa versus 14.7 ± 0.9 GPa), however the stiffness of the 617 glaze is substantially higher than that of the 800HT glaze (220 ± 30 GPa versus 157 ± 6 GPa).

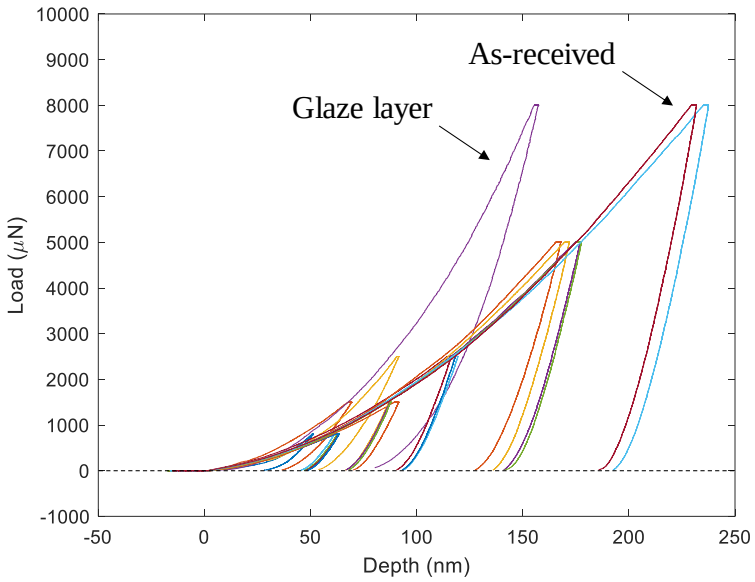

Figure 39. A series of nanoindentation force-depth curves obtained on the as-received surface of alloy 617 and the low-wear glaze layer formed within the wear track generated by self-mated 617-on-617 testing after conditioning the samples under the oxidizing conditions of Regime II. The increased hardness of the glaze is evident by the shallower depths of those curves compared to those of the as-received sample.

The mechanism of glaze formation under high-temperature tribotesting of alloys 800HT and 617 after conditioning in Regime II has been characterized and quantified. SEM cross-sectional images of the wear tracks generated on the surfaces of alloys 800HT and 617 were obtained via FIB milling at locations that reveal both a cross-sectional view of the wear track and a cross-sectional view of the background oxide within the same field of view.

Figure 40 shows SEM cross-sectional images of wear tracks generated on conditioned alloy 800HT and conditioned alloy 617 disks. The yellow profiles drawn on the SEM images

highlight the surfaces of the samples, with the rough background-oxide profile on the left and the smooth wear-track profile on the right. The smooth profile is the surface of the compacted glaze formed during tribotesting. As seen in both images, the smooth, compacted oxide is seen to be intact and continuous with the underlying oxide, demonstrating that the glaze formation is characterized by a short period of wear where the 'glaze' consists of and is formed on top of the oxide layer created by conditioning the sample under the conditions of Regime II. Thus, the oxide created by conditioning is not removed, (i.e., not broken through) by the wear process. With a stable oxide thus established, the high temperature and localized contact pressure can trigger the sintering of oxide particles thereby creating a 'glaze' layer. This indicates that the oxide is crucial in the protective feature of the corrosion process. In addition, the surface of the 800HT glaze looks smoother than that of the 617.

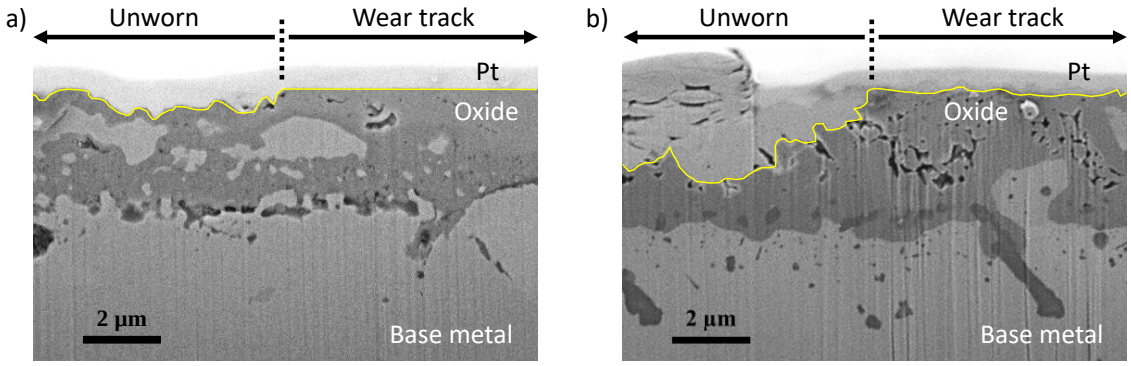

Figure 40. (a) SEM cross-sectional image at the edge of an alloy 800HT wear track obtained via FIB milling. The 800HT disk was conditioned in Regime II and worn at 750 °C at 1 N applied load. A portion of the wear track is visible along the right half of the surface below the Pt coating, and the unworn sample is on the left (yellow profile). (b) SEM cross-sectional image at the edge of an alloy 617 wear track obtained via FIB imaging. The 617 disk was conditioned in Regime II and worn at 900 °C at 1 N applied load. A portion of the wear track is visible along the right half of the surface below the Pt coating, and the unworn sample is on the left (yellow profile).

AFM imaging was used to quantify the background roughness of the Regime-II oxidized surfaces and the smoothness of the compacted glaze. Figure 41 shows 3D AFM images of the background oxide and glaze of alloy 800HT and alloy 617. All images are 10x10 μm^2 in area, and the z-ranges of the images are displayed in the colorbars. The conditioned 800HT background oxide has a 277 nm RMS roughness measured over a 10x10 um^2 area, whereas the 800HT glaze has a roughness of 14.9 nm, both measured over a 10x10 um^2 area. The conditioned 617 background oxide has a 296 nm RMS roughness measured over a 10x10 um^2 area, whereas the 617 glaze has a roughness of 51 nm. The roughnesses of the background oxides are comparable, however the 800HT glaze was significantly smoother than that of 617. The smoother glaze of the conditioned 800HT indicates a higher degree of oxide smoothening by the process of wear, which was observed qualitatively by

comparing Figure 41(a) and Figure 41(b). This suggests that the conditioned 800HT surface required a higher degree of oxide compaction and sintering during wear in order to reach steady-state.

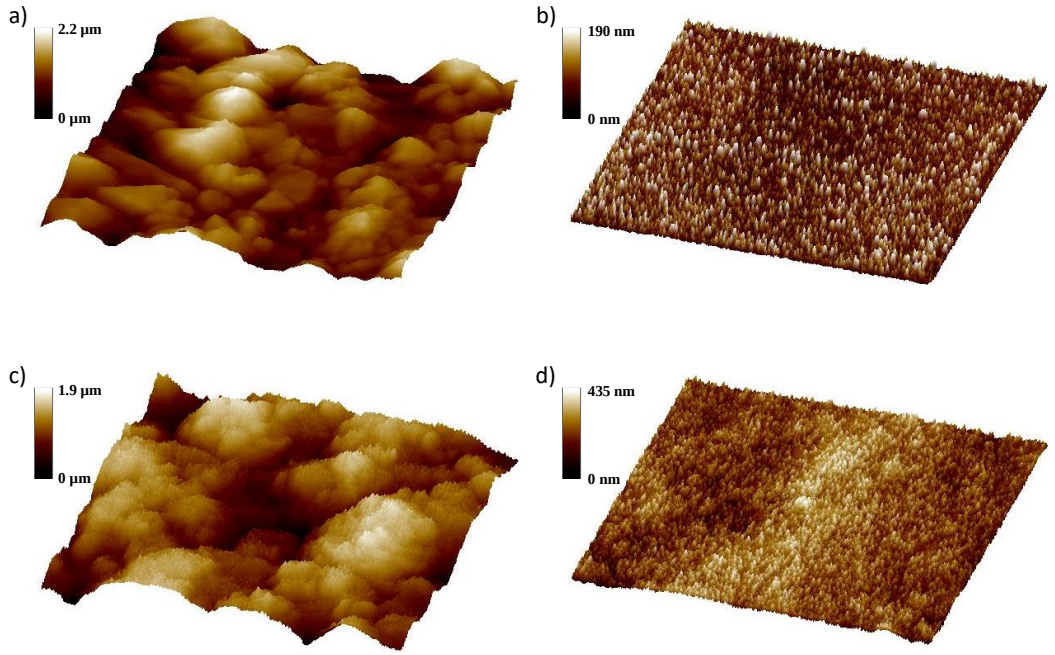

Figure 41. 10x10 µm^2 AFM images. (a) Unworn surface of an alloy 800HT disk conditioned in Regime II. (b) Compacted glaze layer formed on the surface alloy 800HT conditioned in Regime II after wear testing at 750 °C under 1 N load. (c) Unworn surface of an alloy 617 disk conditioned in Regime II. (d) Compacted glaze layer formed on the surface alloy 617 conditioned in Regime II after wear testing at 900 °C under 1 N load.

To investigate the load-bearing capacity of the glaze quantitatively, a custom Matlab® image-analysis program was developed to quantify the area of contact ex-situ between the tribopins and the disks. The program was designed to enable the user to identify the worn regions of a wear track imaged via SEM imaging using a combination of feature detection and manual-area drawing. The program extrapolates the worn area quantified over a single

SEM image over the full extent of the wear track, and then approximates both the apparent area of contact and the true area of contact between the pin and the disk. The routine allows for an approximation of the mean contact stress achieved between the pin and disk to reach steady-state, under the assumption that the majority of wear happens during the run-in period. Figure 42 shows a plot of the mean contact stress supported by the interface at steady-state ($\sigma_{avg,\ ss}$), where the mean contact stress is defined as the ratio of the applied force to the true area of contact between the pin and disk. For all results shown in Figure 42, the applied load was 1 N, and the initial mean contact stress was 115 MPa (calculated using Hertzian contact mechanics). Thus, the stress levels shown in Figure 42 depict those required of the various interfaces in order to achieve a stable, low-wearing contact. For example, for Alloy 617 bare metal (i.e., as-received), the mean contact stress reduced from 115 MPa to 5.7 MPa over the course of the wear test, representing a 95% decrease. However, after Regime-II conditioning, the mean contact stress reduced to 34.8 MPa, representing a 69.7% reduction in stress, or a ~25% improvement in the capacity of the glaze to support the contact stress. For as-received alloy 800HT, the reduction in mean contact stress below that of the initial stress was more significant, with a 99.5% decrease (down to 0.6 MPa). The 800HT glaze also has inferior performance compared to that of the 617 glaze, with a mean steady-state contact stress of 8.8 MPa achieved for 800HT compared to the 34.8 MPa achieved for 617. These results establish two conclusions quantitatively (1) as-received alloy 617 is able to achieve steady-state sliding with a lower degree of contact-stress reduction compared to as-received alloy 800HT, and (2) the 617

glaze is able to support a higher level of contact stress compared to that of the 800HT glaze. Thus, the harder surface along with the more-robust chromium oxide of alloy 617 are able to provide a higher degree of wear resistance. Furthermore, these results corroborate both with the wear volumes presented in previous reports and the supporting evidence provided in Figure 40 and Figure 41.

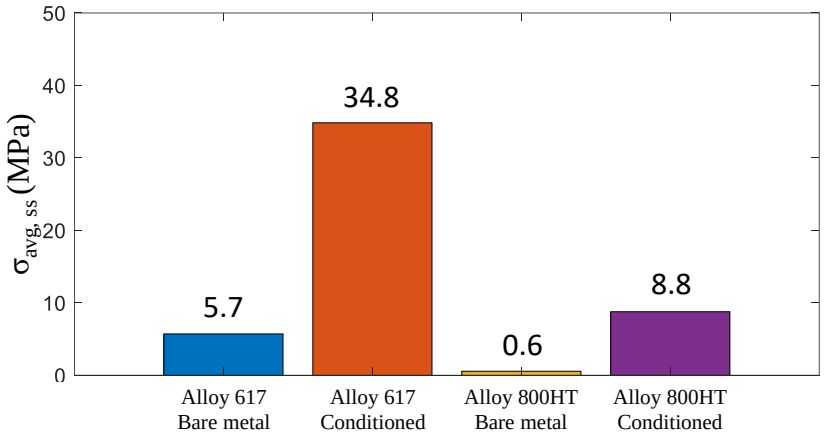

Figure 42. Plot of the mean steady-state contact stress ($\sigma_{avg, ss}$), reached after wear testing alloys 800HT and 617 for 1 hr. under the following conditions - Alloy 617, bare metal: as-received sample wear tested at 900 °C; Alloy 617, conditioned: sample conditioned in Regime II and wear tested at 900 °C; Alloy 800HT, bare metal: as-received sample wear tested at 750 °C; Alloy 800HT, conditioned: sample conditioned in Regime II and wear tested at 750 °C. The initial mean contact stress was 115 MPa for all cases.

4.2. Regime III and IV

4.2.1. Corrosion results

Kolsterising® is a low-temperature carbon diffusion process (< 500 °C) which enhances the mechanical properties of austenitic stainless steel and nickel-based alloys such as 800HT and 617. As a result, the surface gets harder which may lead to an increase in

galling, erosion and fretting wear resistance, and increase in fatigue life [33]. Since the process is conducted at low temperature, the formation of carbides is suppressed, and the corrosion resistance should be preserved [42]. Surface hardnesses of greater than 1000 HV can be achieved in most common austenitic and duplex stainless steels and Ni-based and Co-Cr alloys. Case depths typically range from 10-40 μm.

Figure 43 and Figure 44 show cross-sectional SEM images and GDOES composition profiles for Kolsterised 800HT and Kolsterised 617 respectively. The carbon content appears to be as high as 20% and 10% on the surface for alloys 800HT and 617, respectively. XPS was used to confirm the carbon concentration at the surface of Kolsterised alloy 800HT to be 22.6 +/- 1.6 at. % averaged over the top ~20 nm (excluding the adventitious surface carbon). This value is consistent with the carbon supersaturation observed in 316SS, another austenitic steel [43]. That process, developed by Swagelok Company, increased the typical high-temperature solubility limit of 0.015 at% of carbon in the solid solution. For Kolsterised 800HT and Kolsterised 617 studied herein, the enriched carbon profile decays down to the baseline value after 23 μm and 9 μm for alloys 800HT and 617, respectively. Additionally, neither GDOES scan indicates the presence of an oxide due to the Kolsterising® treatment

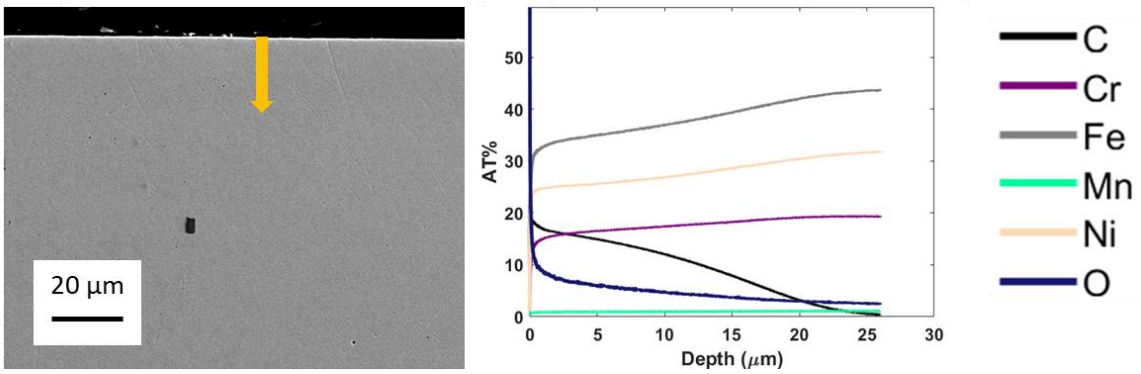

Figure 43: Cross-sectional SEM image and GDOES profile of Kolsterised 800HT.

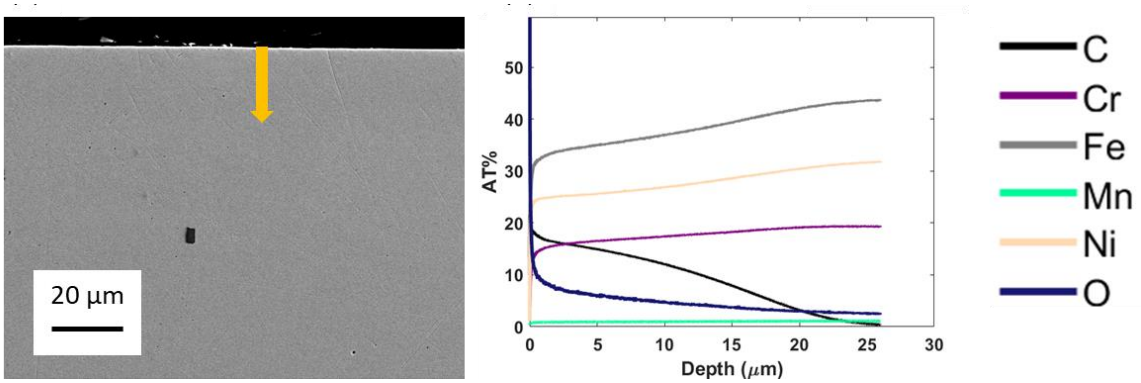

Figure 44: Cross-sectional SEM image and GDOES profile of Kolsterised 617.

The XRD scans of the Kolsterised samples presented in Figure 45 and Figure 46 indicate that no additional phase was formed after Kolsterising®. The only noticeable difference is the shift of the peaks, which is due to the higher lattice parameter caused by the entrapment of carbon atoms in interstitial sites of the alloy.

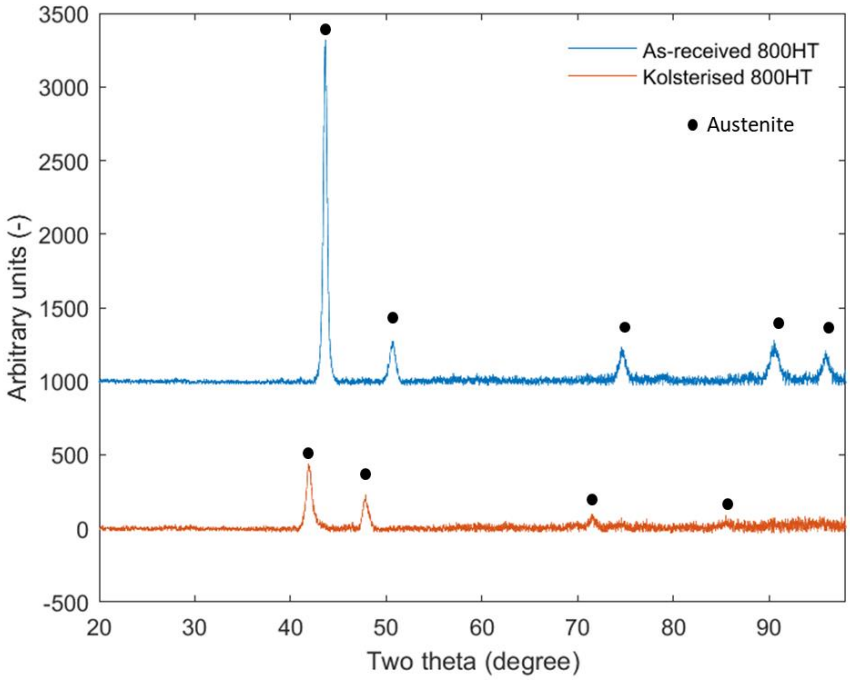

Figure 45: XRD scans for as-received and Kolsterised alloy 800HT.

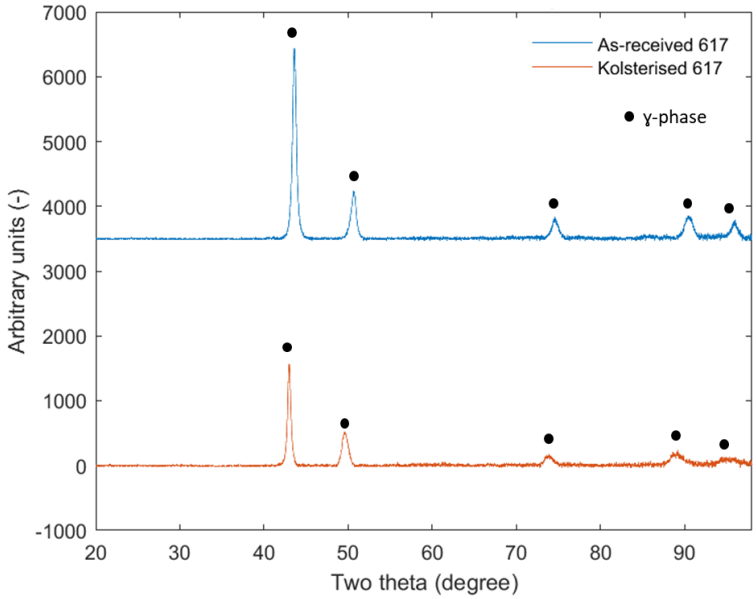

Figure 46: XRD scans for as-received and Kolsterised alloy 617.

Figure 47, Figure 48, Figure 49, and Figure 50 feature SEM images, EDS line scans and GDOES profiles presenting the cross-sectional compositions of alloys 800HT and 617 after conditioning in Regime III.

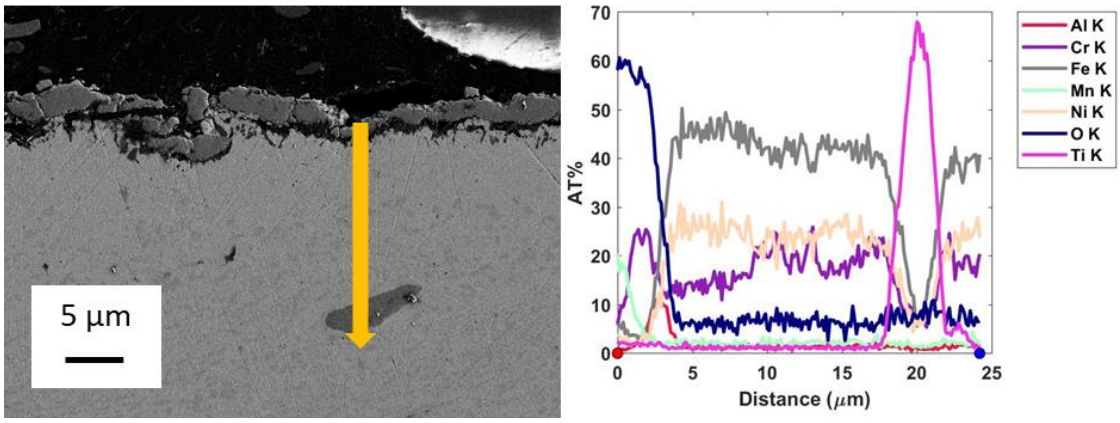

Figure 47: Cross-sectional SEM image and EDS line scan of 800HT conditioned in Regime III.

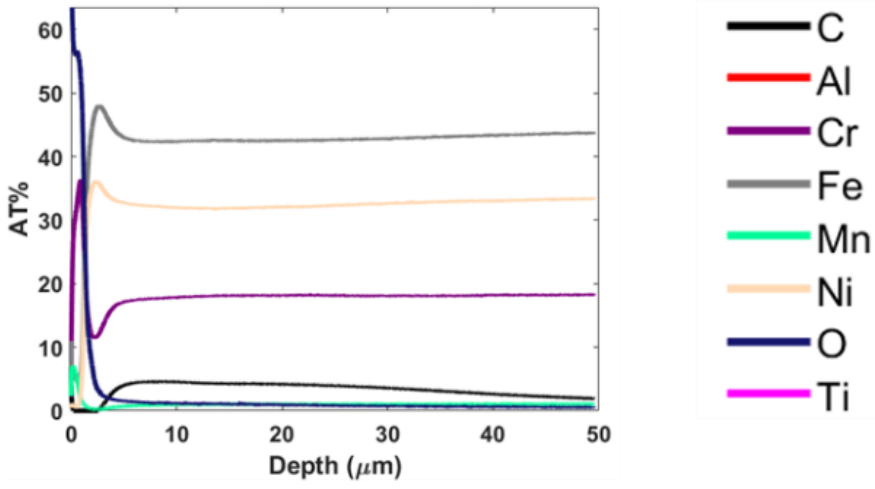

Figure 48: Cross-sectional GDOES profile of 800HT conditioned in Regime III.

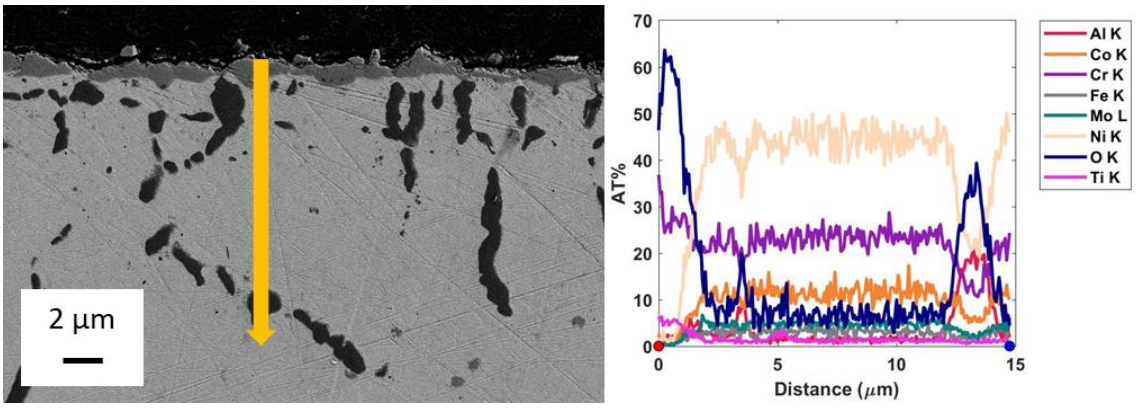

Figure 49: Cross-sectional SEM image and EDS line scan of 617 conditioned in Regime III.

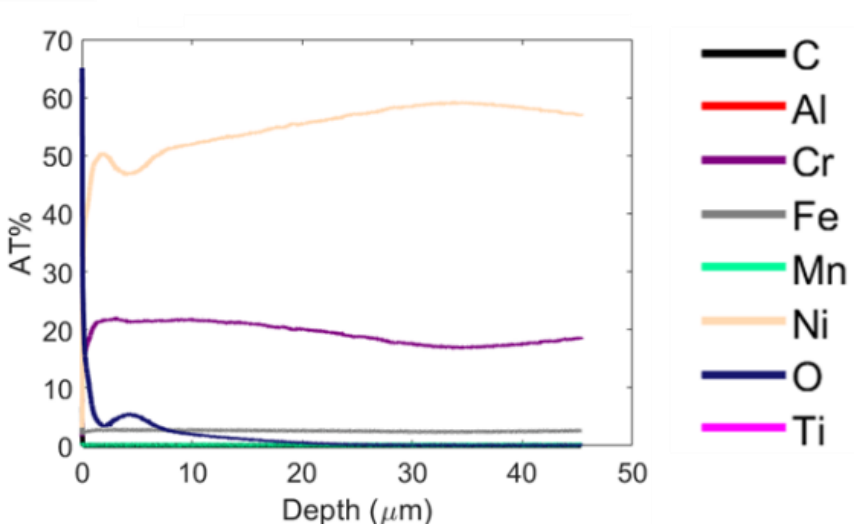

Figure 50: Cross-sectional GDOES profile of 617 conditioned in Regime III.

Alloy 800HT developed a mixed Mn-Cr oxide and an underlying aluminum oxide on the entire surface. The increased thickness (3.98 ± 0.62 µm) and higher content of manganese in the oxide indicate that the diffusion of carbon in the near surface has an unexpected impact on the corrosion of the samples. Additionally, Figure 48 indicates that the carbon

content was reduced from ~20 at% to ~5 at% in the sample during exposure at 750 °C for 22 days.

Conditioning of alloy 617 in Regime III leads to the formation of a chromium oxide on the surface in addition to internal aluminum oxide at the grain boundaries. This external oxide scale is approximately equal in thickness (0.98 ± 0.37 μm) to that developed during Regime II. Figure 50 shows that the carbon in solid solution sublimated from the sample during exposure at 900 °C for 22 days.

4.2.2. Tribological test results

Figure 51 presents the wear track morphology for Kolsterised 800HT. At low load, Kolsterised 800HT develops a glaze layer on the load-bearing surfaces. When a higher load is applied, oxide wear followed by scuffing occurs.

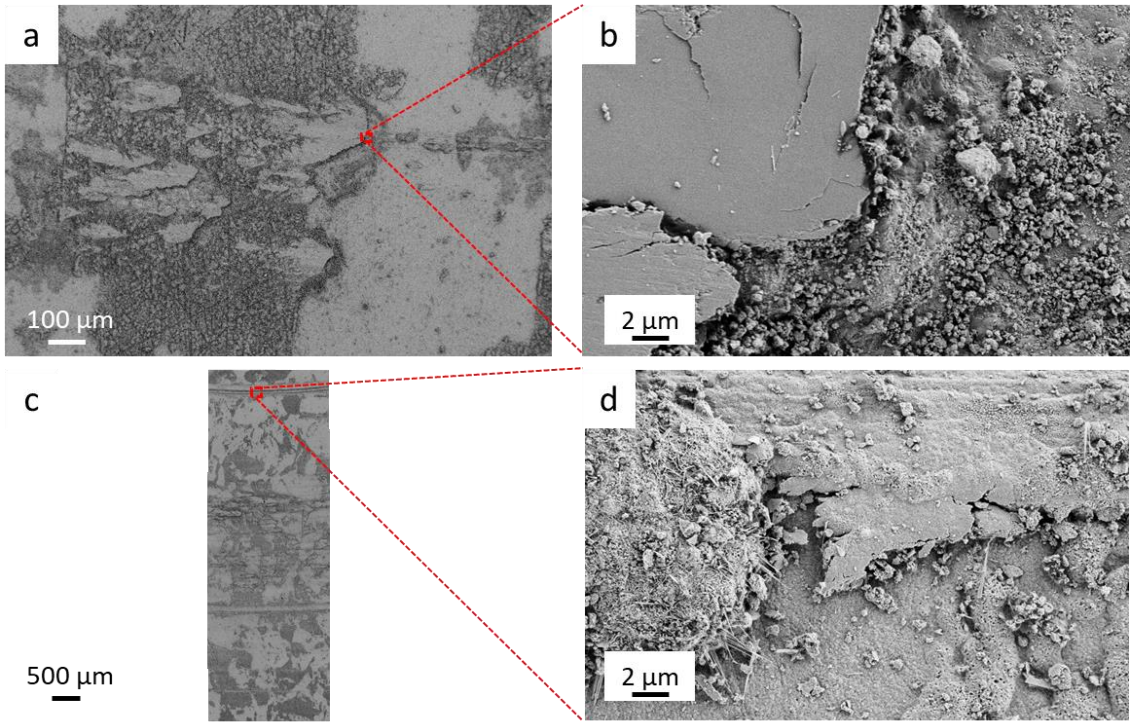

Figure 51: Morphology of the 800HT wear tracks after Kolsterising® for (a, b) a 1N load at 750 °C for (c, d) a 5N load at 750 °C.

Figure 52 shows that patches of iron oxide are formed, surrounded by a thinner Cr-Ni oxide, as was the case for samples conditioned in air. In addition, Figure 53 shows that the oxide developed during tribotest is much thicker for Kolsterised 800HT than for of as-received 800HT. These observations support the notion that Kolsterising® increases the oxidation rate for alloy 800HT. The presence of manganese on the surface after tribotesting is consistent with the cross-sectional composition analysis of 800HT samples conditioned in Regime III.

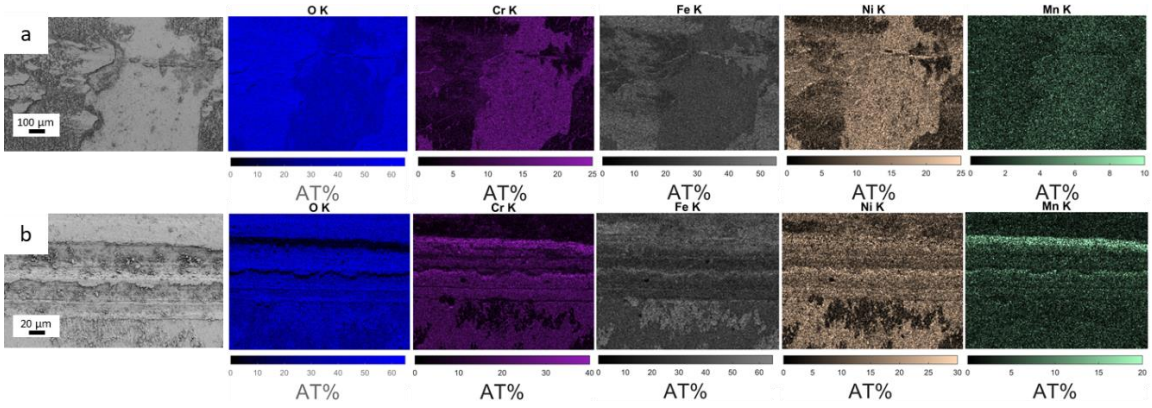

Figure 52: Top-down SEM and EDS maps of 800HT wear tracks after Kolsterising® for (a) a 1N load at 750 °C and (b) a 5N load at 750 °C.

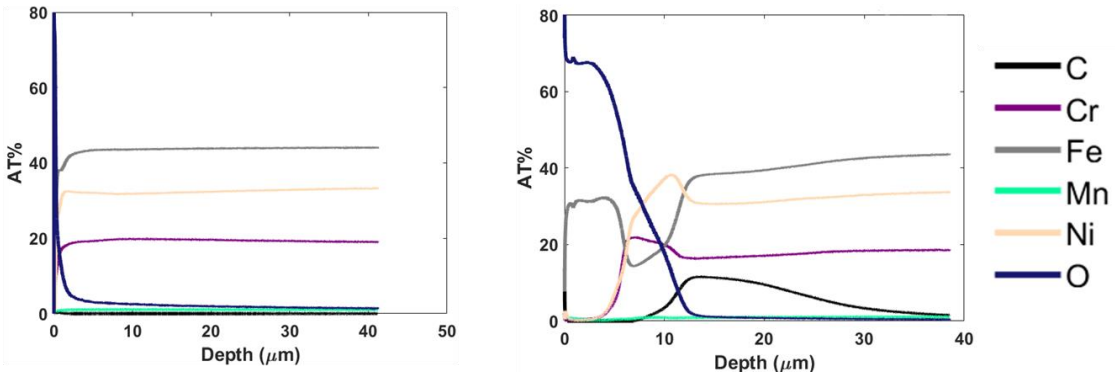

Figure 53: GDOES profiles of (a) as-received 800HT and (b) Kolsterised 800HT after wear testing at 750 °C.

The morphology of Kolsterised 617 is shown in Figure 54. At both loads, mild scuffing and material removal happen first. As debris are created, they build up and get compacted to become the load-bearing areas of the wear tracks.

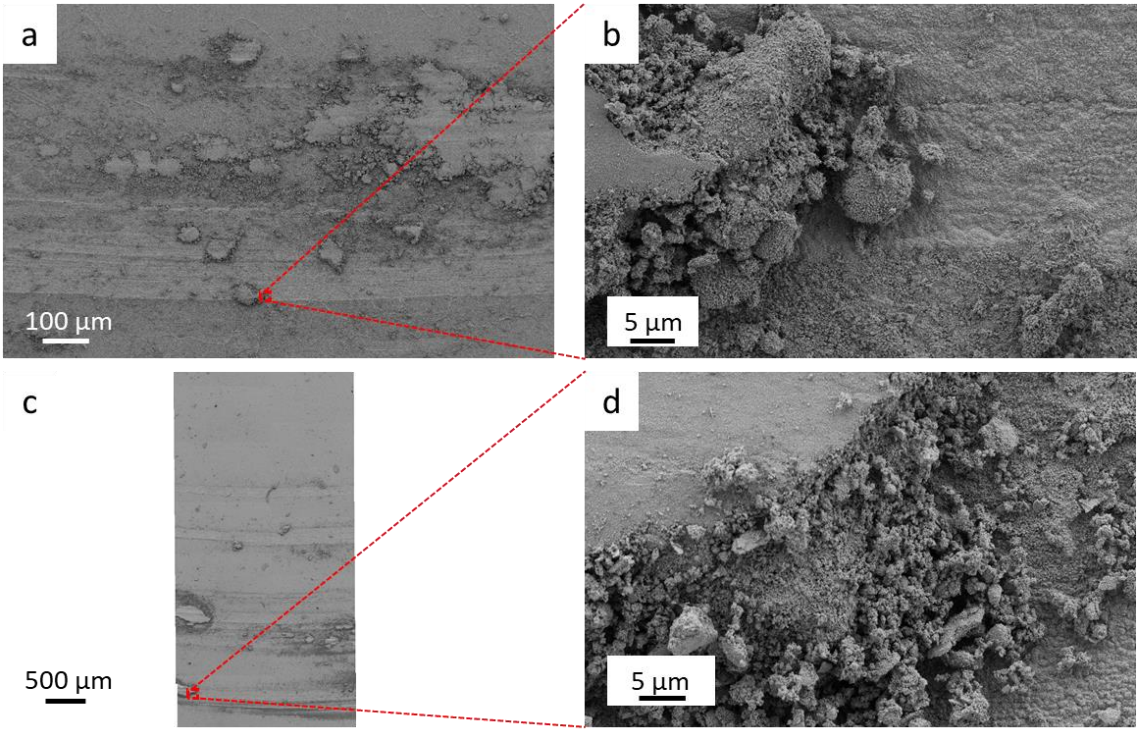

Figure 54: Morphology of the 617 wear tracks after Kolsterising® for (a, b) a 1N load at 900 °C and for (c, d) a 5N load at 900 °C.

During tribotesting, chromium oxide forms in the background while it is being removed in the wear track as shown in Figure 55. The oxidation rate of the load-bearing areas is too low to enable the formation of a glaze layer and therefore consist of worn debris compacted together with a bulk-like composition. As indicated by Figure 56, the oxide that develops in the background is twice as thick as the one developing during the tribotest for as-received 617, which indicates that the oxidation rate is also increased for alloy 617 when exposed to high-temperature air.

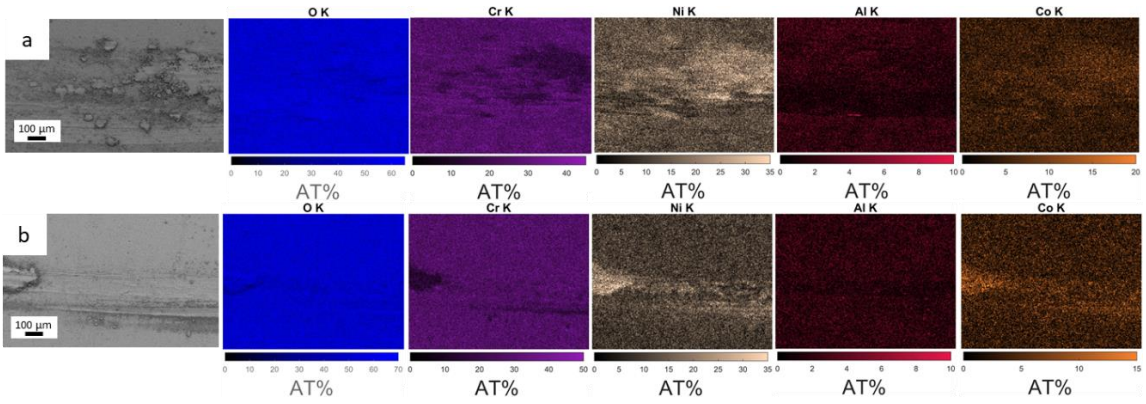

Figure 55: Top-down SEM and EDS maps of 617 wear tracks after Kolsterising® for (a) a 1N load at 900 °C and (b) a 5N load at 900 °C.

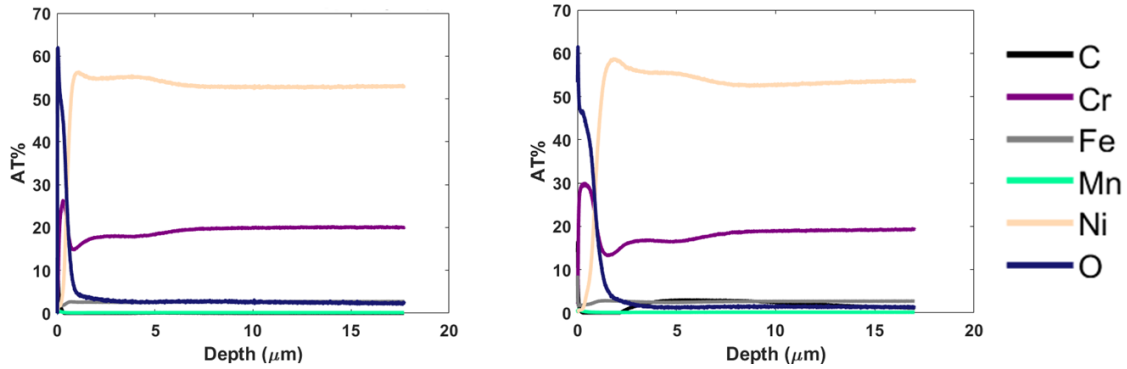

Figure 56: GDOES profiles of (a) as-received 617 and (b) Kolsterised 617 after wear testing at 900 °C.

The profilometry results for both alloys after Kolsterising® are presented in Figure 57. The wear appears much less severe than that of as-received samples, especially at higher load. The wear track is narrower, and grooves are shallower than those of as-received samples for both alloys. In addition, wear tracks seem deeper for alloy 800HT than for alloy 617.

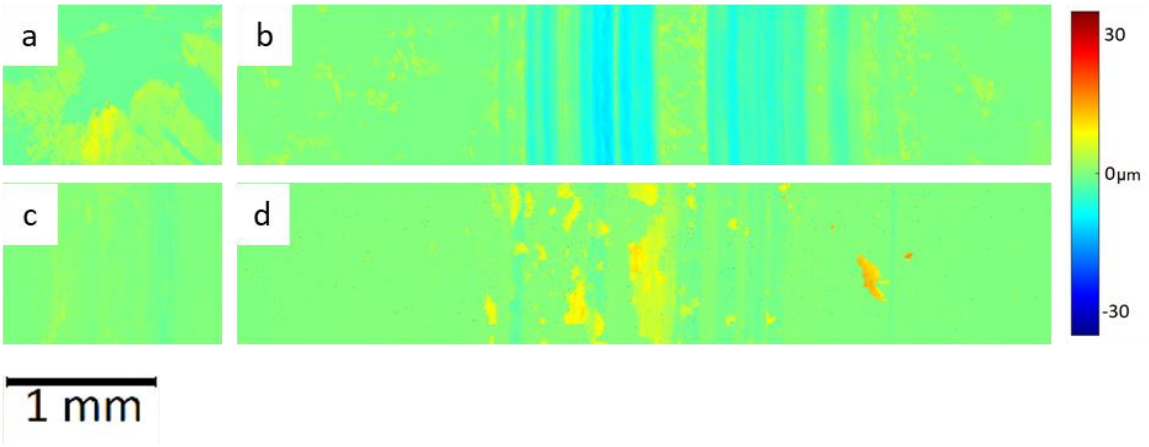

Figure 57: Wear track profilometry for (a, b) 800HT after Kolsterising® and testing at 1N, 750 °C and 5N, 750 °C, respectively and (c, d) 617 after Kolsterising® and testing at 1N, 900 °C and 5N, 900 °C, respectively.

The wear volumes and initial friction coefficients presented in Figure 58 are consistent with the profilometry and morphology results. The amount of material removed from alloy 800HT after Kolsterising® is much lower than that of as-received samples. In addition, the initial friction coefficient values are twice as low as those of as-received samples, which also indicates milder wear. This reduction is likely due to the formation of a protective oxide on the surface during temperature ramp up. Alloy 617 experiences the same behavior in terms of wear volumes with a sharp decrease at higher load. Yet, since the sliding contact is metal-on-metal, the values presented for the initial friction coefficients are similar to those of as-received samples. The decrease in wear volume can be explained by a shorter run-in period likely due to a hardened surface.

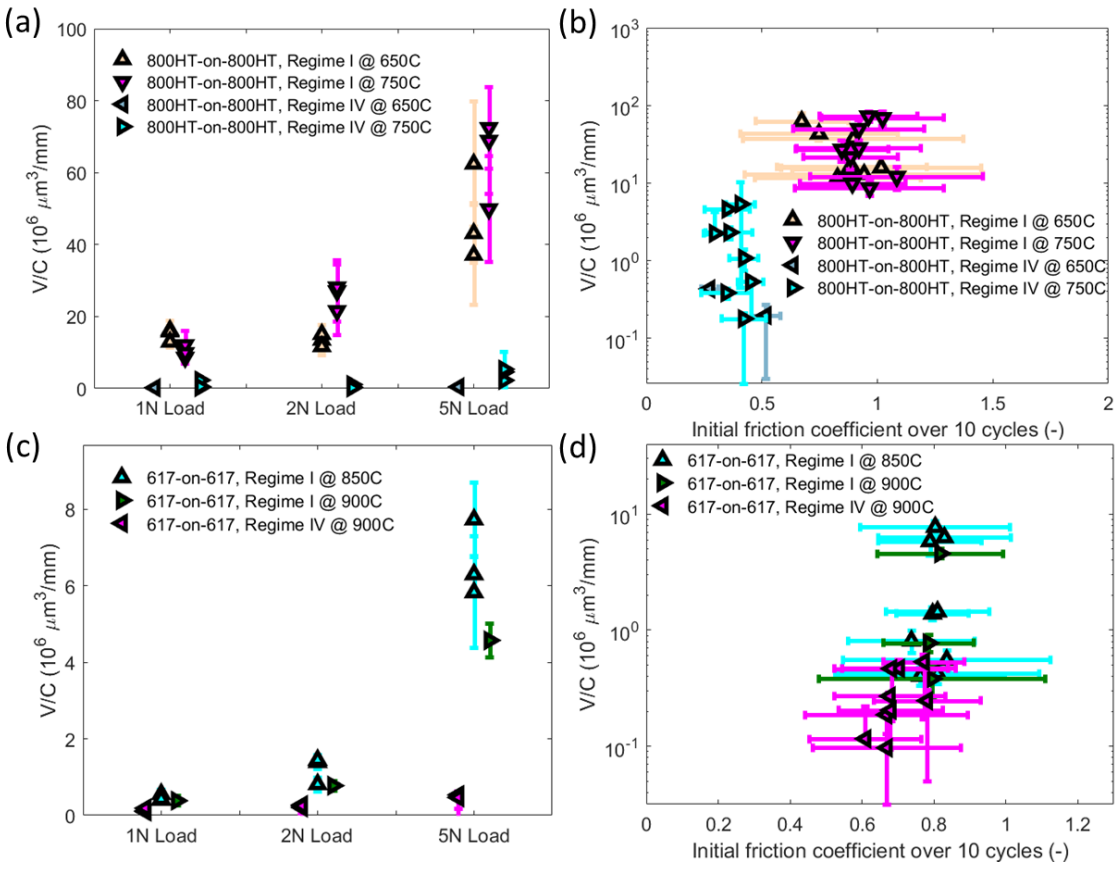

Figure 58: Wear volumes as a function of load (a, c) and initial friction coefficient (b, d) for as-received and Kolsterised self-mated 800HT and 617 tested at elevated temperatures.

The wear track morphologies of 800HT conditioned in Regime III are presented in Figure 59. At higher load, imaging indicates that the oxide has been worn through and that scuffing of the metal-on-metal contact took place thereafter. Stochastic variation at lower load prevented the oxide from being worn through in some cases as shown in Figure 59 (a, b) where the oxide resisted wear. In such cases, the wear appears less severe than as-received material.

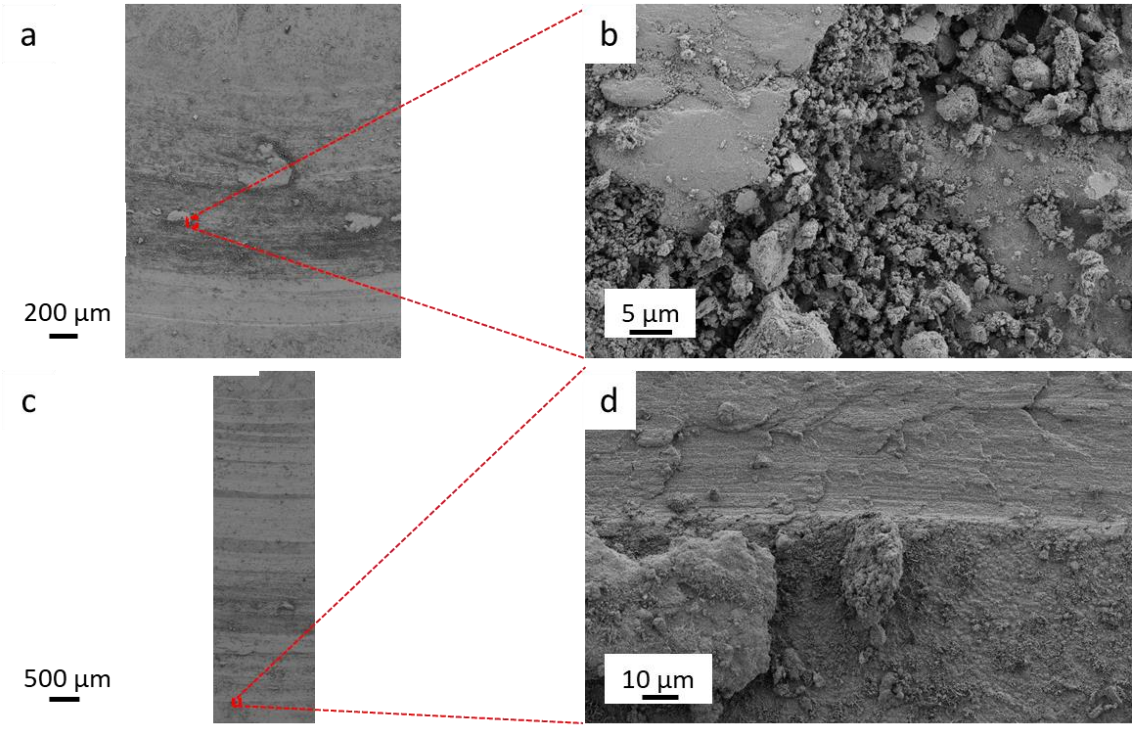

Figure 59: Morphology of 800HT wear tracks after conditioning in Regime III for (a, b) a 1N load at 750 °C for (c, d) a 5N load at 750 °C.

The wear track compositions presented in Figure 60 are consistent with the wear mechanisms described previously. In the background, the Mn-Cr oxide that formed during conditioning at high temperature is still present, while the oxide in the wear track has been worn through and replaced by a metal-on-metal contact, hence the bulk-like composition.

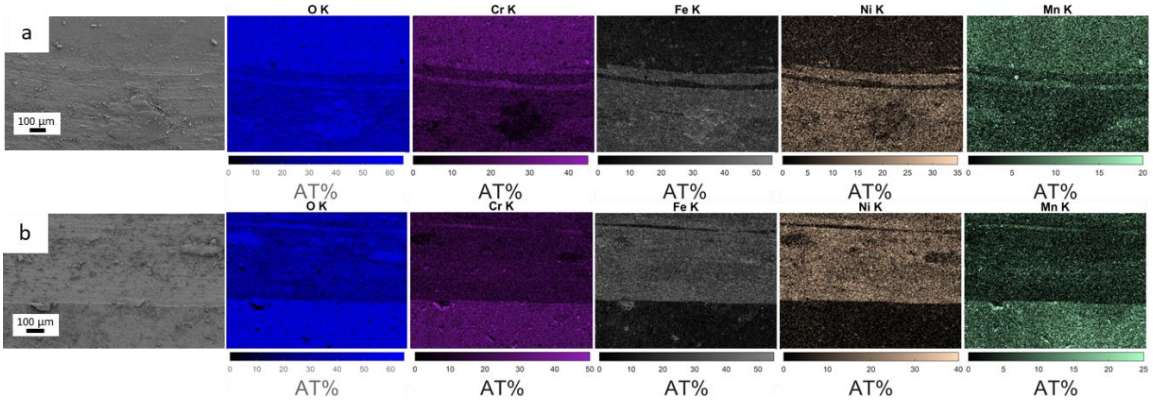

Figure 60: Top-down SEM and EDS maps of 800HT wear tracks after conditioning in Regime III for (a) a 1N load at 750 °C and (b) a 5N load at 750 °C.

With regards to profilometry, Figure 61 indicates less severe wear than samples conditioned in Regime II that experienced oxide breakthrough at higher load, and slightly more severe wear at lower load. These results are consistent with the wear volumes and initial friction coefficients values presented in Figure 62. Wear volumes are slightly higher than those of samples conditioned in Regime II at low load and lower on average than those of samples conditioned in Regime II that experienced oxide breakthrough. Since no glaze layer was developed, and the oxide was always worn for samples conditioned in Regime III, the initial friction coefficients results are consistent with the Regime II cases where the oxide was broken through.

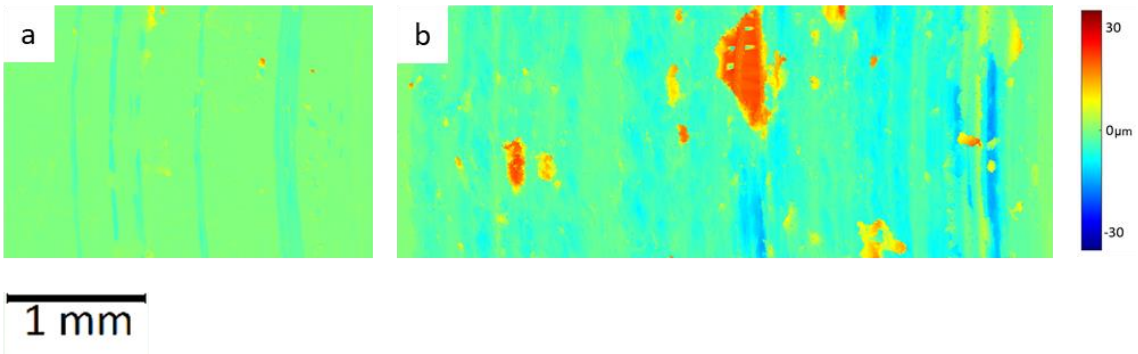

Figure 61: Wear track profilometry for (a, b) 800HT conditioned in Regime III and tested at 1N, 750 °C and 5N, 750 °C, respectively.

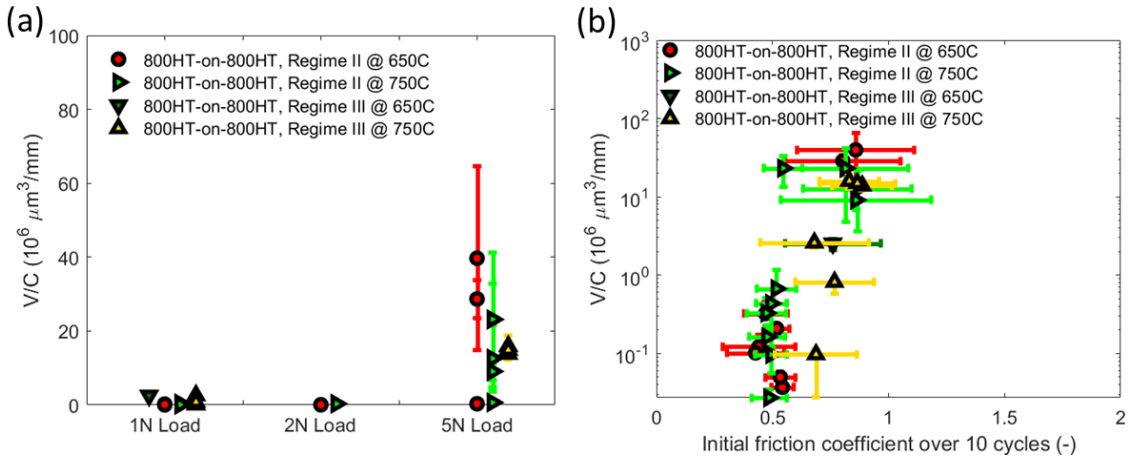

Figure 62: Wear volumes as a function of load (a) or initial friction coefficient (b) for self-mated 800HT conditioned in Regimes II and Regime III and tested at elevated temperatures.

4.3. Aluminization

4.3.1. Corrosion results

Figure 63 presents a cross-sectional SEM image and an EDS line scan of 800HT after aluminization for 36 hrs.

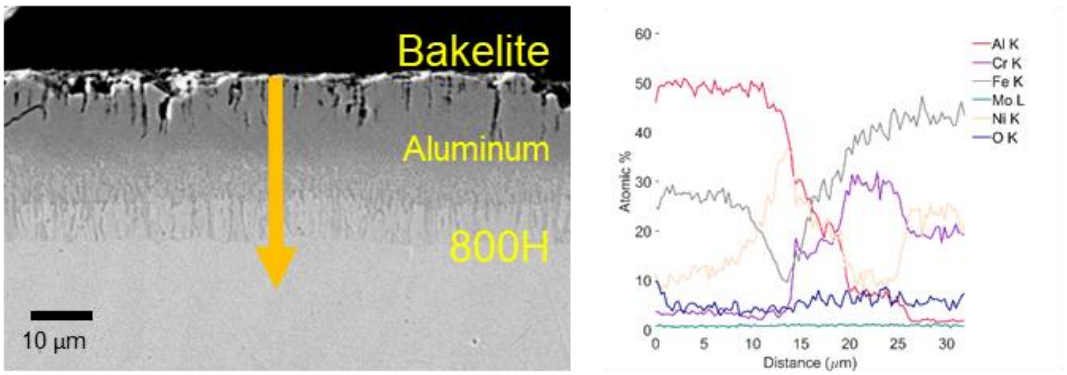

Figure 63: Cross-sectional SEM image and EDS line scan of aluminized 800HT.

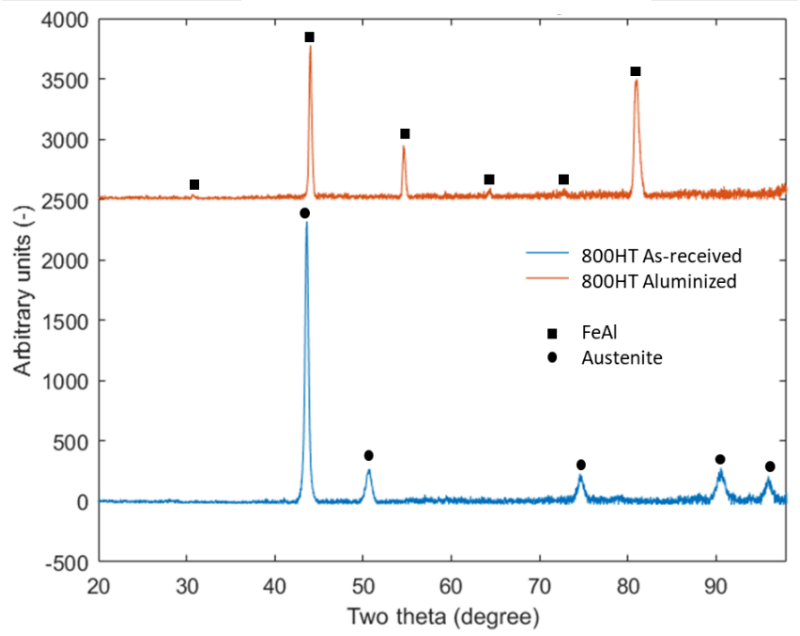

Figure 64: XRD patterns for as-received and aluminized 800HT.

The aluminized region was measured to be 24.66 ± 3.13μm for 800HT. For Incoloy® 800HT, cracking of the aluminized layer is observed, which was also observed in previous work by other researchers in Incoloy 800HT samples pack aluminized at 850 °C [44]. As shown in the XRD scans presented in Figure 64, the Al-rich surface region is comprised of FeAl intermetallic phases.

Aluminization resulted in three distinct zones in the near-surface regions of the alloy. The top zone was 11.38 ± 3.11 μm thick and rich in Fe and Al, with at least 20 at% Al and 10 at% Fe [labeled Fe-Al in Figure 69(c)]. The second zone was 6.60 ± 1.31 μm thick and rich in Ni and Al, with at least 10 at% Ni and 20 at% Al. The third and the bottom zone was 5.52 ± 0.97 μm thick and consists of Cr-rich columns with at least 25 at% Cr. The regions rich in Ni and Al extend between the Cr-rich columns at the top of the third zone, and the base metal extended as protrusions between the Cr-rich columns from the at the bottom.

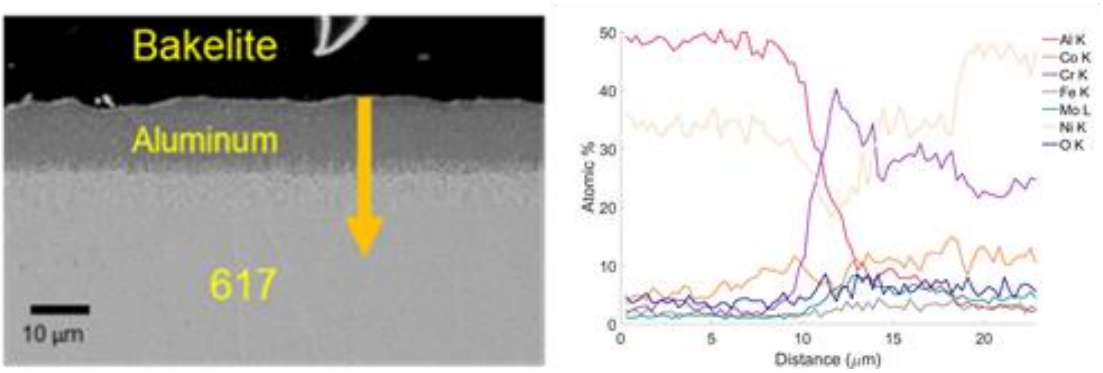

Figure 65: Cross-sectional SEM image and EDS line scan of aluminized 617.

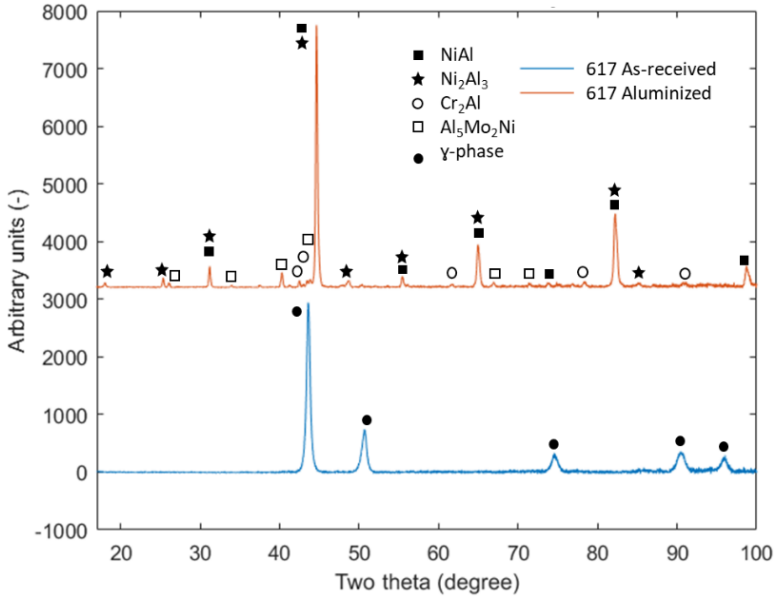

Figure 66: XRD patterns for as-received and aluminized 617.

Figure 65 shows a cross-sectional SEM image and an EDS line scan of alloy 617 after aluminization for 36 hrs. The aluminized region was measured to be 17.62 ± 1.36µm for 617. The upper Al-rich zone is comprised of multiple Ni-, Cr- and Mo-Al intermetallic phases for alloy 617 as shown in the XRD scans shown in Figure 66. The intermetallic compounds for alloy 800HT and alloy 617 as shown in the XRD scans are confirmed by

the literature [35, 45]. For Inconel® 617, similar to alloy 800HT, three distinct zones developed in alloy 617 upon aluminization. The first zone was 9.41 ± 0.92 μm thick and contained at least 10 at% Ni and 20 at% Al, as shown in Figure 70(c). The second zone was 2.64 ± 0.56 μm thick and consisted of at least 10 at% Cr and 20 at% Al. The third zone was 5.57 ± 0.60 μm and consisted of regions rich in both Cr (at least 30% Cr) and Cr and Mo (at least 8% Mo). This elemental profile is typical for alloy 617 [35]. Cross-sectional nanohardness profiles (discussed below) indicate that the intermetallic phases on the surface lead to a higher hardness than the bulk base material. This observation is consistent with the literature [37].

Cross-sectional nanohardness profiles of aluminized alloy 800HT, shown in Figure 69(a), indicate that these intermetallic phases on the surface have a higher hardness than the base material, with a value at the uppermost indent of 7.33 $\pm$ 0.40 GPa compared to the base-alloy value of 3.63 $\pm$ 0.34 GPa. This intermetallic hardness is higher than previously reported hardness values for FeAl intermetallics [46], but previously reported values were still higher than the base-metal hardness of 800HT. The Ni- and Al-rich regions are higher in hardness than the base alloy, with a value of 5.04 $\pm$ 0.43 GPa. The Cr-rich columns were the hardest regions with a value of 8.44 $\pm$ 2.76 GPa.

Cross-sectional nanohardness profiles of aluminized alloy 617, shown in Figure 70(a), indicate that intermetallic phases on the surface lead to a higher hardness. The hardness at

the uppermost indent is 7.58 ±0.28 GPa, and the hardness of the base metal is 4.18 ± 0.36 GPa. The zone rich in Cr and Mo has hardness of 8.64 + 1.03 GPa, although with a larger error bar due to the presence of columns of base metal within the zone which increases the scatter in nanohardness.

Figure 67 and Figure 68 show the cross-sectional images and EDS line scan of aluminized samples conditioned in Regime II for alloys 800HT and 617 respectively.

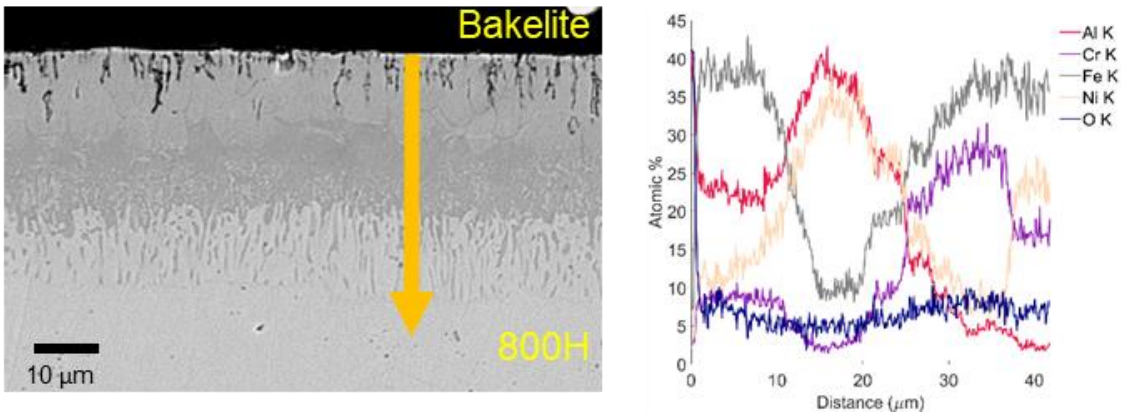

Figure 67: Cross-sectional SEM image and EDS line scan of aluminized 800HT conditioned in Regime II.

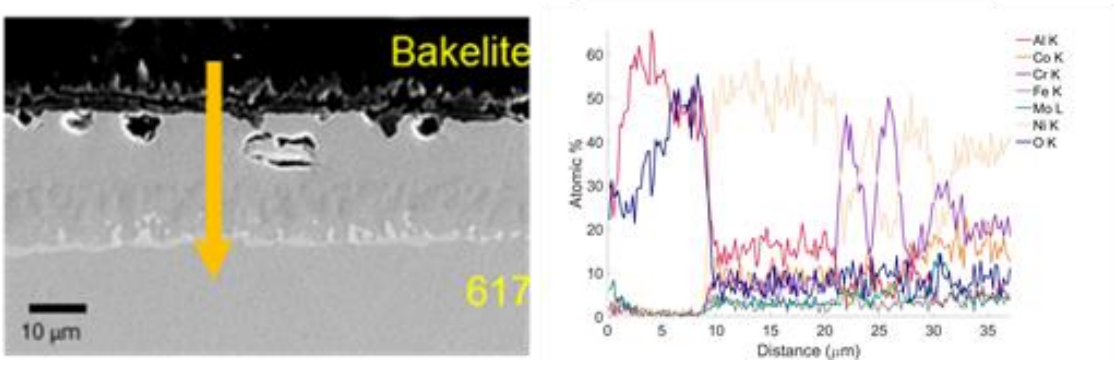

Figure 68: Cross-sectional SEM image and EDS line scan of aluminized 617 conditioned in Regime II.

After conditioning aluminized alloy 800HT, the aluminum-modified region was measured to be 40.79 ± 1.17 μm thick, and an aluminum oxide layer 0.79 ± 0.30 μm in thickness formed on the surface of the samples. The elemental composition of the near-surface regions changed significantly upon conditioning. Aluminum diffused both towards the surface due to oxidation and further into the bulk of the sample. The aluminum content in the FeAl zone decreased due to oxide formation, as shown in Figures 5(b) and 5(e). This caused the hardness to decrease as shown in Figure 5(d), to 4.55 ± 0.68 GPa. The thickness of the Fe-Al zone, which contains at least 20 at% Al and 10 at% Fe, is comparable to its thickness before conditioning, at 12.55 ± 2.21 μm. Additionally, both lower zones increased in thickness by a factor of two. The Ni- and Al-rich zone had a hardness of 5.54 ±0.76 GPa and increased in thickness to 13.44 ± 2.04 μm. The Cr-rich columnar zone has a hardness of 9.78 ± 0.79 GPa and increased in thickness to 14.12 ± 0.93μm.

After conditioning aluminized alloy 617, the aluminum-modified region for the aluminized sample was measured to be 25.09 ± 1.53 μm thick, and an aluminum oxide layer of 10.54 ± 2.64 μm thickness formed on the surface. The oxide formed on alloy 617 appears flaky and not firmly adherent to the surface, and the elemental composition at the surface changed significantly, as shown in Figure 70(c) and Figure 70(f). The thickness of the Ni- and Al-rich zone increased to 12.66 ± 1.60 μm, and the aluminum content decreased due to Al diffusion into the oxide and internal Al diffusion into the bulk. This caused the hardness to decrease to 4.63 ± 1.24 GPa at the uppermost indent. The Cr- and Al-rich zone

disappeared, and Cr became segregated from the Al. This caused a columnar zone to form, with at least 30 at% Cr, that is 6.74 ± 0.90 μm thick and is interspersed with either base-metal columns or Ni- and Al-rich columns, seen in Figure 70(f). The hardness of this zone was 7.90 ± 3.1 GPa. A second columnar zone formed below the above zone, with a thickness of 5.69 ± 0.99 μm. This zone consisted of regions with at least 30 at% Cr and 10 at% Mo. A Cr-rich, Mo-enriched zone also developed at the interface with the base-alloy and had hardness of 12.15 ± 2.15 GPa. The large error bars for the hardness of this zone [Figure 70(d)] are due to the inclusion of the softer Ni- and Al-rich and base-metal columns within the zone.

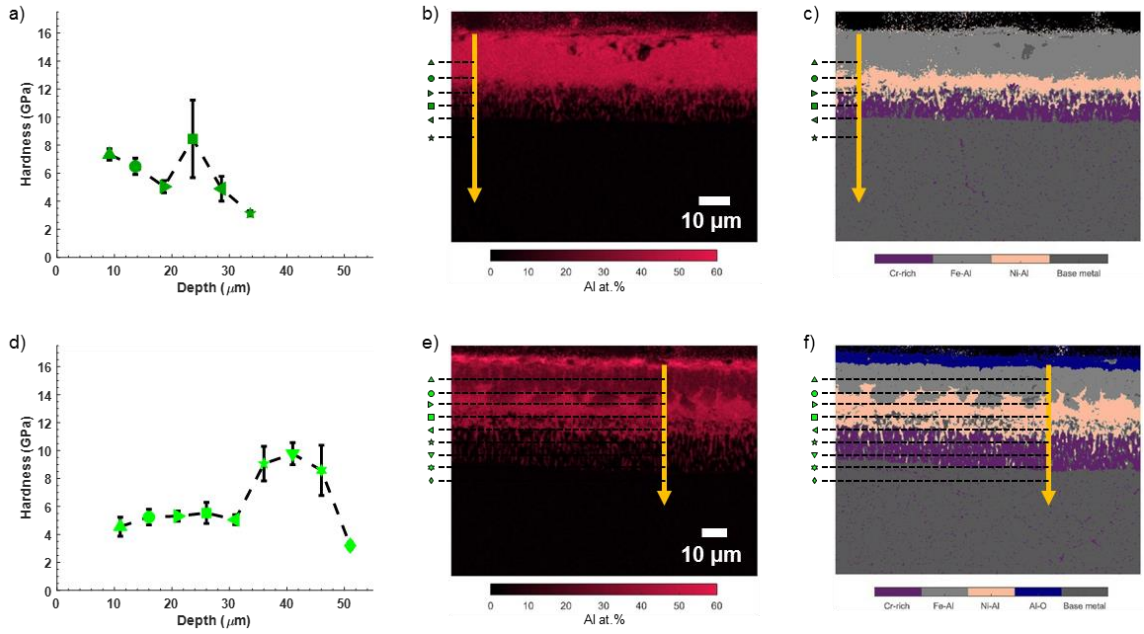

Figure 69. Cross-sectional nanohardness measurements of aluminized alloy 800HT samples. (b) EDS cross-sectional aluminum map of the aluminized 800HT coupon. The yellow arrow corresponds to the depth of the plot in (a), and the symbols alongside the arrow indicate the depths from which the nanohardness measurements were obtained. (c) EDS cross-sectional

layered image revealing the dominant elements and their combinations in the aluminized coupon. (d) Cross-sectional nanohardness measurements of aluminized alloy 800HT sample after conditioning. (e) EDS cross-sectional aluminum map of the coupon after aluminization followed by conditioning. (f) EDS cross-sectional layered image revealing the dominant elements and their combinations in the sample after aluminization followed by conditioning.

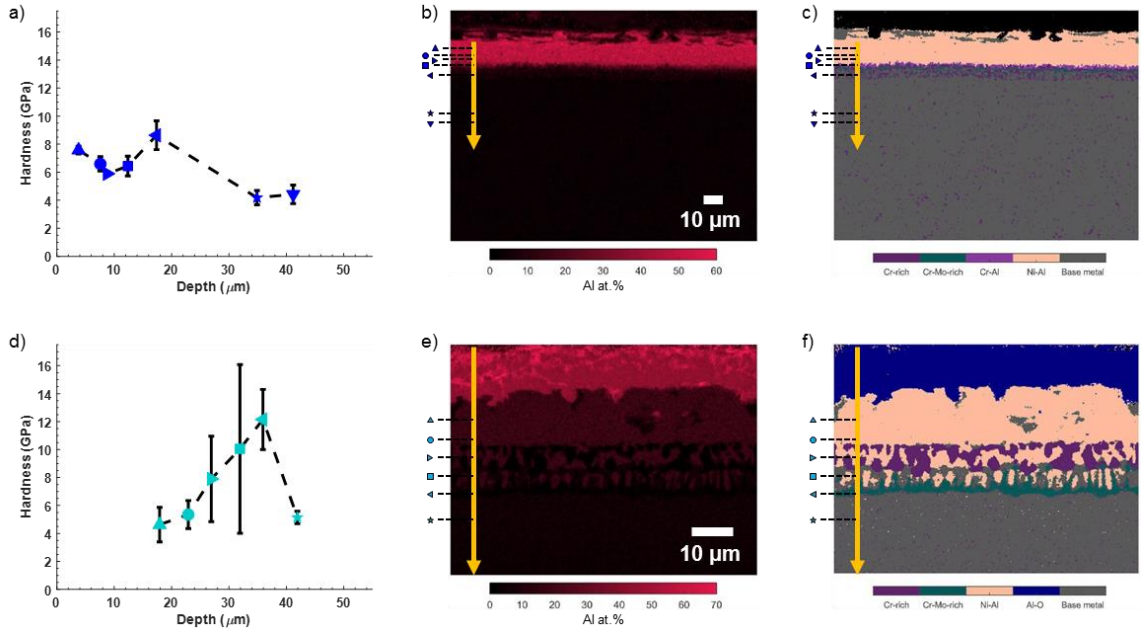

Figure 70. Cross-sectional nanohardness measurements from an aluminized alloy 617, (b) EDS cross-sectional aluminum elemental map of the aluminized alloy 617 sample. The yellow arrow in (b) corresponds to the depth-axis of the plot in (a), and the symbols alongside the arrow indicate the depths from which the nanohardness measurements were obtained, (c) EDS cross-sectional layered image revealing the dominant elements and their elemental combinations in the aluminized sample, (d) Cross-sectional nanohardness measurements of alloy 617 after aluminization followed by conditioning, (e) EDS cross-sectional aluminum map of the sample after aluminization followed by conditioning, (f) EDS cross-sectional layered image revealing the dominant elements and their elemental combinations in the aluminized and conditioned sample.

4.3.2. Tribological test results

The morphological and compositional analyses of aluminized 800HT wear tracks presented in Figure 71 and Figure 72 indicate mild scuffing at both loads with worn regions

and background approximately of the same composition. A thin aluminum oxide developed on the samples' surface. However, wear prevented this oxide from be consistent throughout the worn surface. The EDS analysis confirmed the presence of an Fe-Al rich layer beneath the aluminum oxide at both loads and also the presence of a Ni-Al sub-layer for more severely scuffed cases at high load.

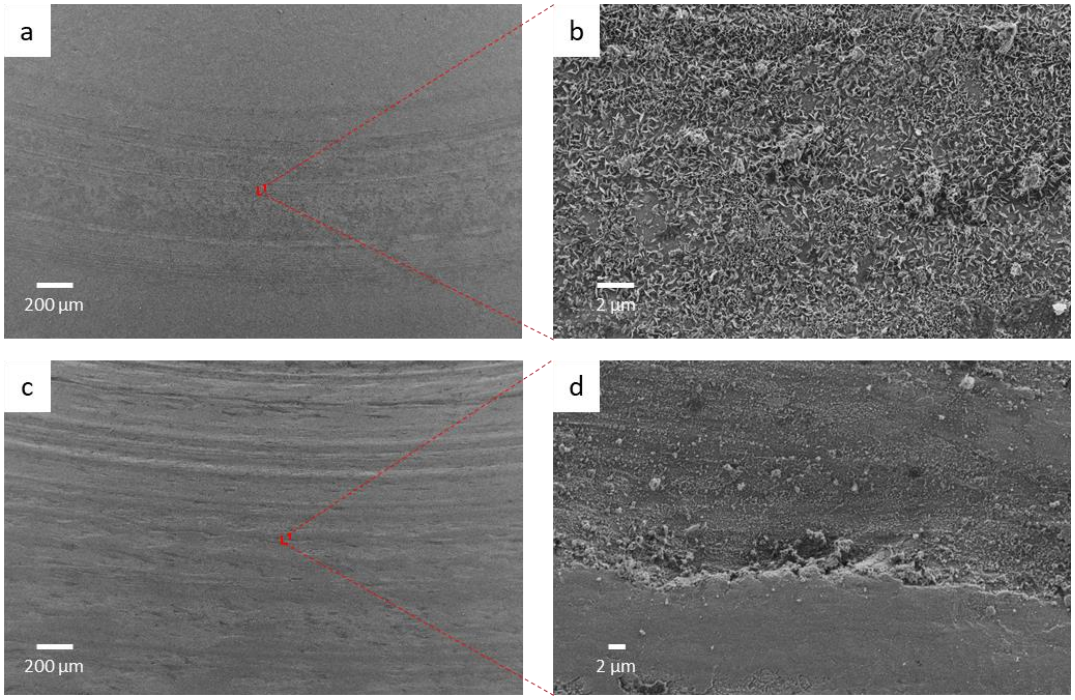

Figure 71: Morphology of the aluminized 800HT wear tracks for (a, b) a 1N load at 750 °C and for (c, d) a 5N load at 750 °C.

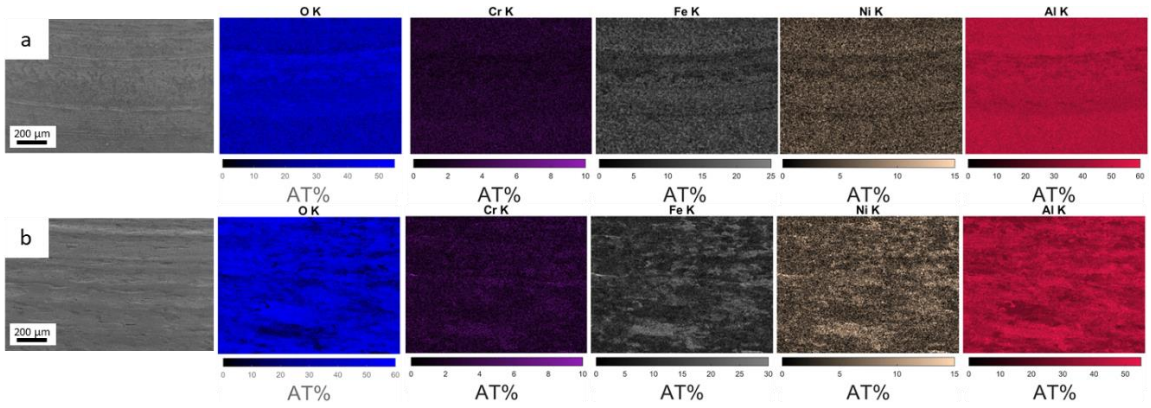

Figure 72: Top-down SEM and EDS maps of aluminized 800HT wear tracks after (a) a 1N load at 750 °C and (b) a 5N load at 750 °C.

For aluminized 617 samples, the sliding contact spans over the whole wear track where grooves and patches were created as shown in Figure 73. The extensive presence of cracks in the surface of aluminized 617 led to scuffing and gouging in the wear tracks. Cracks in load-bearing patches provide evidence of ceramic wear due to debris compaction. These debris were created in the first stages of the sliding process and were built up to form higher patches. The depth of the wear track measured via optical profilometry along with the EDS cross-sectional line scan of aluminized samples indicate that the debris are Cr- and Mo-depleted. Since the debris are small, diffusion does not play a significant role, and the oxide formed has a metallic composition closer to the first Ni-Al-Co layer rather than an exclusive aluminum oxide. Being protected from further scuffing, the background and the trenches in the wear tracks developed an aluminum oxide as shown in Figure 74.

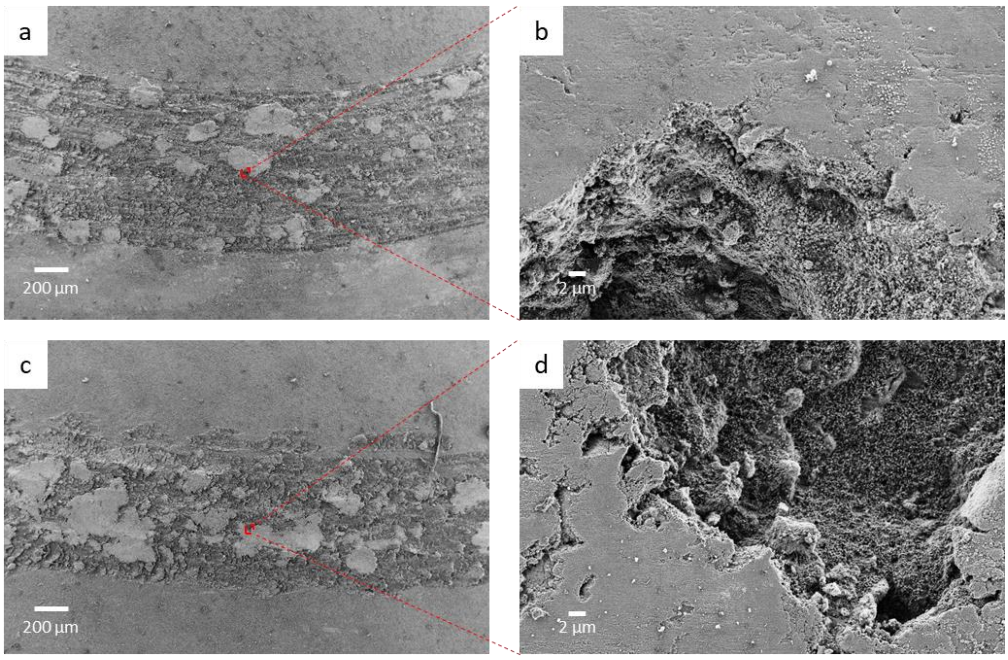

Figure 73: Morphology of the aluminized 617 wear tracks for (a, b) a 1N load at 900 °C and for (c, d) a 5N load at 900 °C.

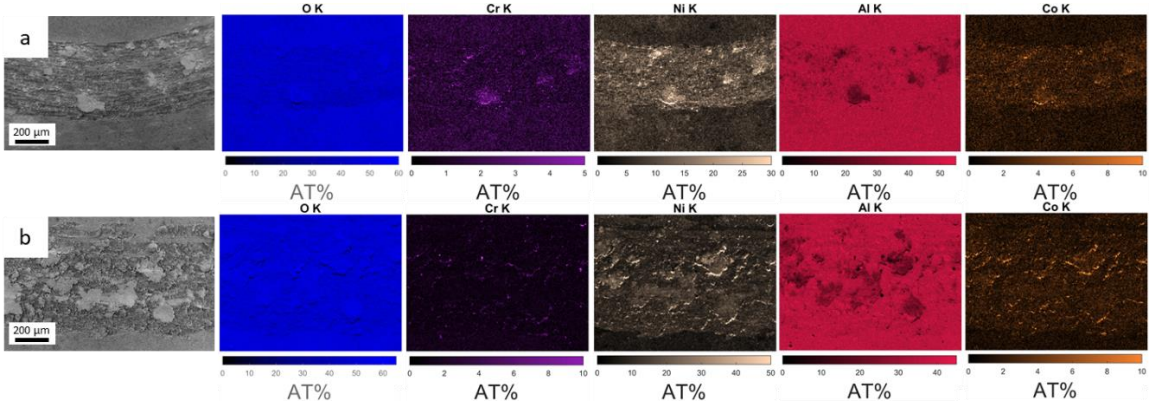

Figure 74: Top-down SEM and EDS maps of aluminized 617 wear tracks for (a) 1N wear testing at 900 °C and (b) 5N wear testing at 900 °C.

Profilometry imaging, wear volumes and initial friction coefficient values for both alloys after aluminization are presented in Figure 75 and Figure 76. The results indicate much less severe wear than as-received samples for alloy 800HT. These observations are

confirmed by order-of-magnitude lower wear volumes consistent with lower initial friction coefficient values. This improvement in wear performance is likely due to the increase in the surface hardness due to the formation of a FeAl intermetallic phase. Indeed, Fe-Al intermetallic compounds possess an excellent high-temperature wear resistance in spite of their poor wear resistance at room temperature [37].

For alloy 617, profilometry results indicate similar wear severity for both loads. Moreover, wear appears more aggressive than that of as-received samples at low load, but less aggressive at higher load. These observations are supported by wear volume values higher than that of as-received samples at low load and lower than that of as-received samples at high load. Additionally, width and depth of the wear tracks of aluminized samples are comparable at both loads. This phenomenon can be explained by a poor mechanical integrity of the near surface with the cracks created during aluminization rendering the near-surface regions brittle. This layer is broken through during the initial stages of the contact, and the wear stops when the mechanically stable harder NiAl intermetallic phase is reached. While high-load tribotests present higher initial friction coefficients because more material is being removed in the first stages of the sliding contact, they also present shorter run-in periods, which is consistent with comparable wear volumes at both loads.

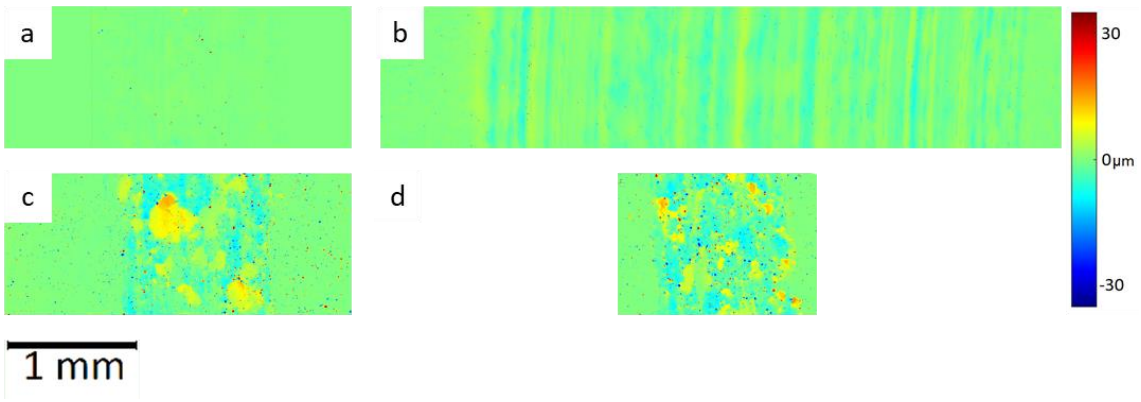

Figure 75: Wear track profilometry for (a, b) aluminized 800HT tested at 1N, 750 °C and 5N, 750 °C, respectively and (c, d) aluminized 617 tested at 1N, 900 °C and 5N, 900 °C, respectively.

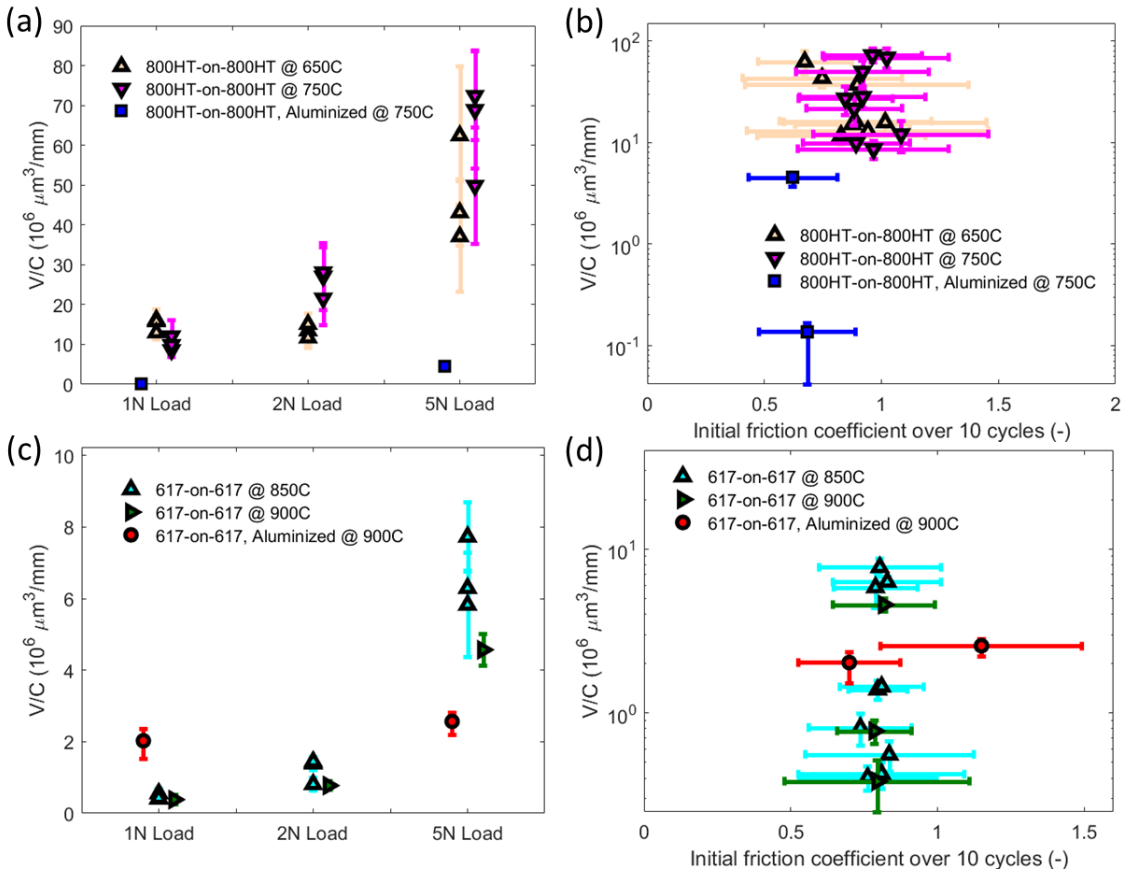

Figure 76: Wear volumes as a function of load (a, c) and initial friction coefficient (b, d) for as-received and aluminized self-mated 800HT and 617 tested at elevated temperatures.

Figure 77 and Figure 78 present the morphologies and compositions of the wear tracks of aluminized 800HT conditioned in Regime II. The background of the samples consists in the aluminum oxide that formed during conditioning. For most of the tribotests, this oxide was removed, and the composition of the first Fe-Ni-Al layer is revealed. The debris created were compacted together to form load-bearing patches that experienced ceramic wear behavior.

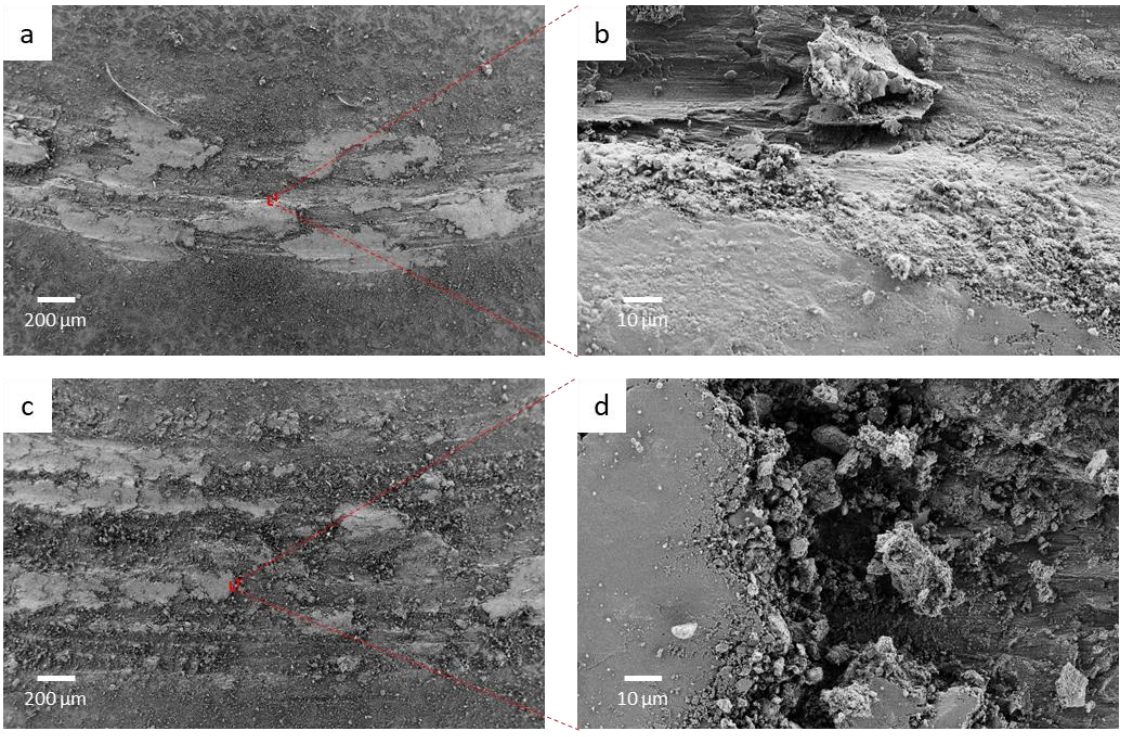

Figure 77: Morphology of aluminized 800HT wear tracks after conditioning in Regime II for (a, b) a 1N load at 750 °C and for (c, d) a 5N load at 750 °C.

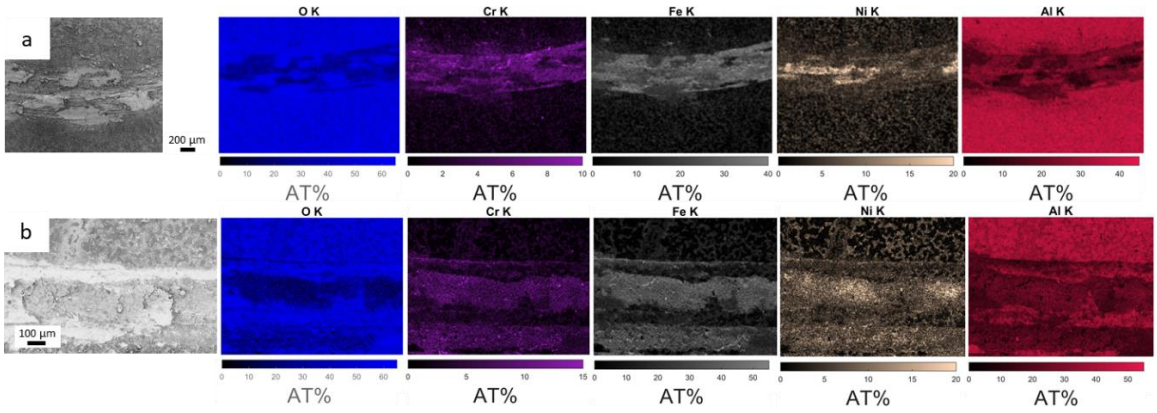

Figure 78: Top-down SEM and EDS maps of aluminized 800HT wear tracks after conditioned in Regime II for (a) a 1N load at 750 °C and (b) a 5N load at 750 °C.

The wear track morphologies and compositions of aluminized 617 conditioned in Regime II are presented in Figure 79 and Figure 80. The wear appears to be quite aggressive at both loads. The oxide has been removed, hence the aluminum content in the wear track is depleted and the composition is closer to that of the first Ni-Al-Co layer. The aluminum oxide is still present in the background of the samples. The morphology of the wear tracks indicates ceramic wear, with low content of aluminum and chromium once the external flaky oxide is removed.

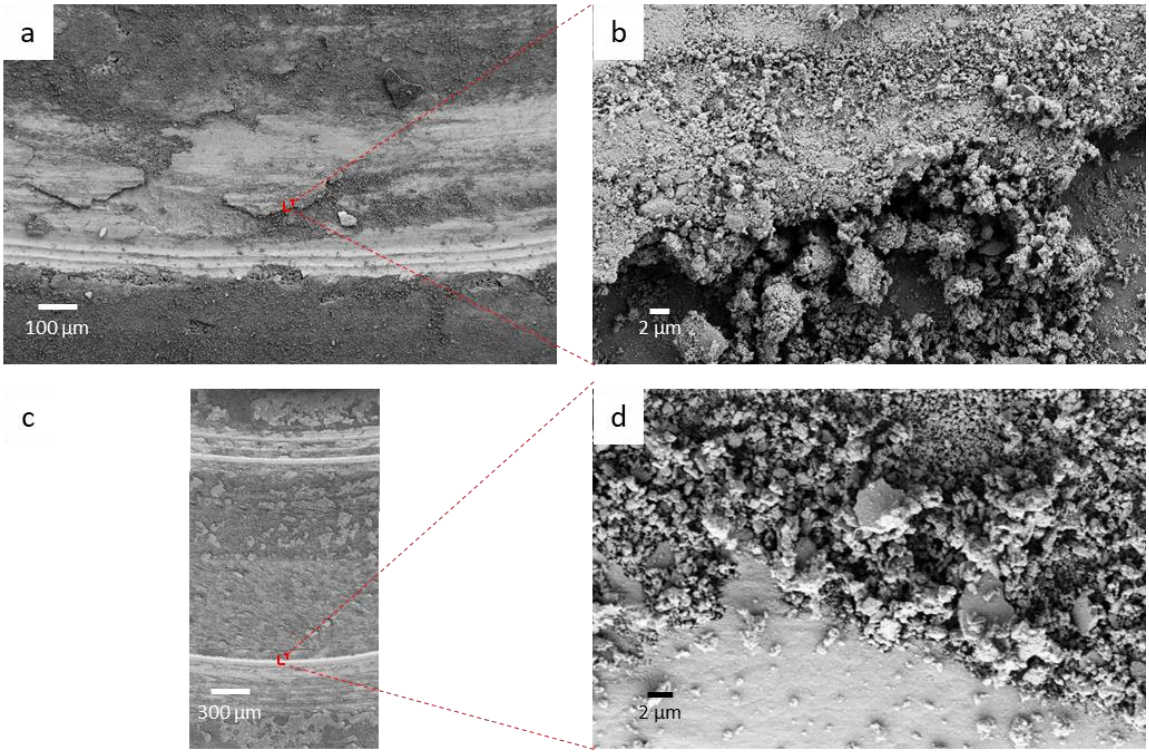

Figure 79: Morphology of the aluminized 617 wear tracks after conditioning in Regime II for (a, b) a 1N load at 900 °C and for (c, d) a 5N load at 900 °C.

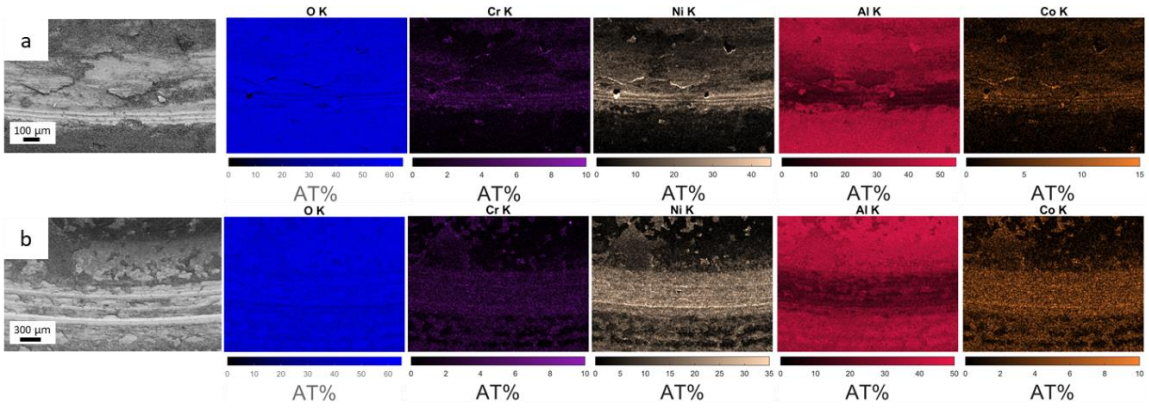

Figure 80: Top-down SEM and EDS maps of aluminized 617 wear tracks after conditioning in Regime II for (a) a 1N load at 900 °C and (b) a 5N load at 900 °C.

Profilometry imaging, wear volumes and initial friction coefficients of the wear tracks for both alloys are presented in Figure 81 and Figure 82. For alloy 800HT, these results

indicate that the wear is more severe than that of Regime II at 1N, but less severe at higher loads. At low load, when the oxide was removed, the wear volumes and initial friction coefficients were higher than those of Regime II samples. When the oxide was still present, these values were comparable to those of Regime II samples. For alloy 617, profilometry results indicate that aluminized samples conditioned in Regime II present much more severe wear than Regime II samples. Additionally, the wear tracks of high-load tribotests are deeper and wider than those of low loads tribotests. Both observations are supported by wear volumes five times as high as those of Regime II samples and increased initial friction coefficient values.

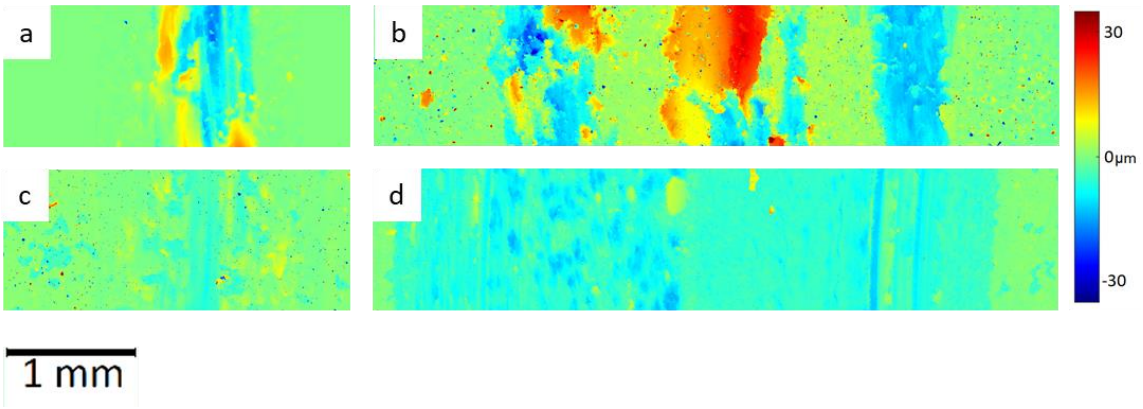

Figure 81: Wear track profilometry for (a, b) aluminized 800HT conditioned in Regime II and tested at 1N, 750 °C and 5N, 750 °C, respectively and (c, d) aluminized 617 conditioned in Regime II and tested at 1N, 900 °C and 5N, 900 °C, respectively.

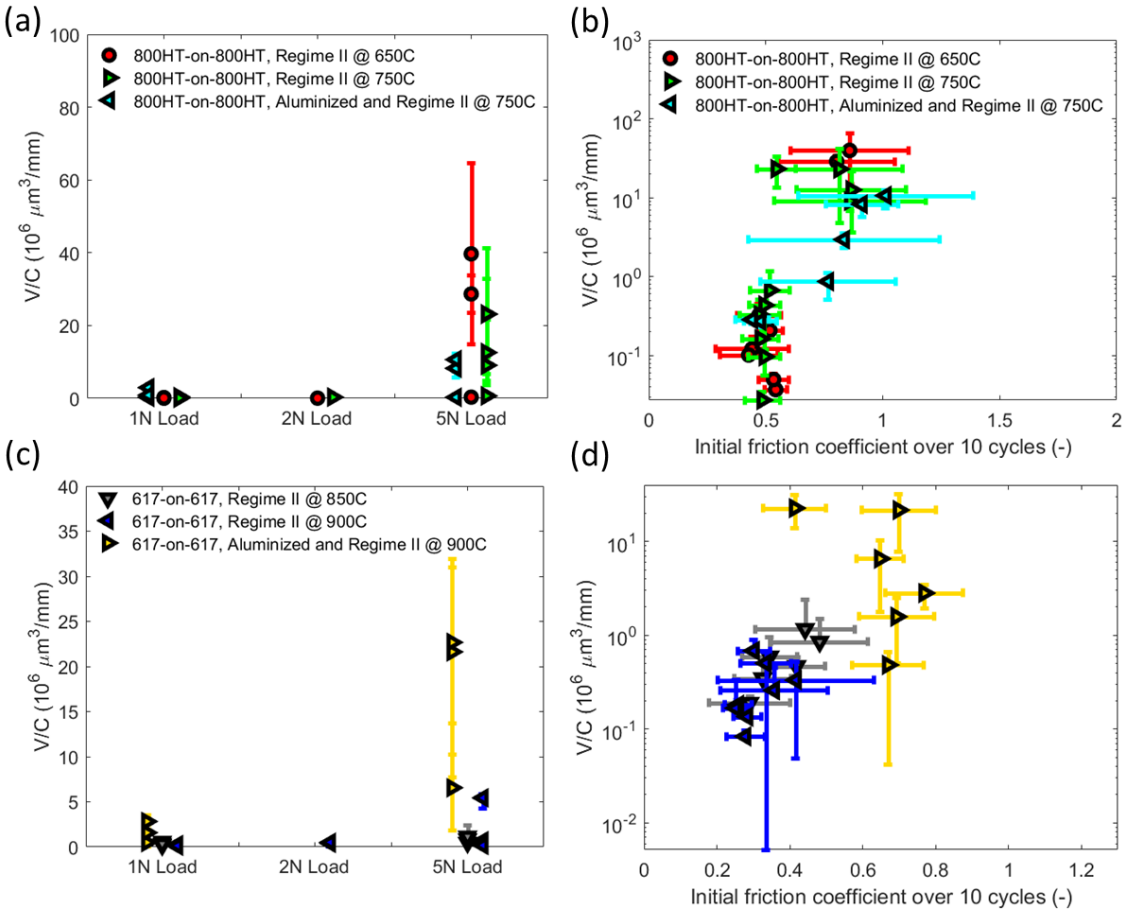

Figure 82: Wear volumes as a function of load (a, c) and initial friction coefficient (b, d) for self-mated 800HT and 617 after conditioning in Regime II, after aluminization, and after aluminization followed by conditioning in Regime II.

Table III shows a comprehensive summary of the chemical compositions of the unworn and worn regions of both alloys after wear testing. Table entries listed as N/A reflect the fact that wear testing did not generate worn patches, worn grooves, or wear debris.

Table III. Atomic concentrations (%) of elements detected in select regions both inside and outside the wear tracks formed via high-temperature pin-on-disk wear testing of alloys

800HT and 617. Values for atomic concentrations were extracted from EDS mapping of the alloy 800HT and alloy 617 wear tracks shown in Figure 11 and Figure 12, respectively.

Material	Condition	Regions																												
		Unworn							Worn patches							Worn grooves							Wear debris						
		Al	Co	Cr	Fe	Mn	Ni	O	Al	Co	Cr	Fe	Mn	Ni	O	Al	Co	Cr	Fe	Mn	Ni	O	Al	Co	Cr	Fe	Mn	Ni	O
800HT	As-received	2	-	17	35	3	20	19	N/A							1	-	21	34	5	16	19	1	-	10	25	2	11	49
	Conditioned in $He+H_2O$*	1	-	4	28	3	16	46	1	-	12	22	6	9	50	N/A							N/A						
		1	-	27	8	11	4	48																					
	Aluminized	46	-	3	13	1	5	31	N/A							42	-	2	12	1	5	37	N/A						
	Aluminized & conditioned in $He+H_2O$	45	-	2	9	1	47	39	N/A							31	-	3	16	1	6	42	N/A						
617	As-received	3	5	24	2	-	16	45	N/A							1	3	34	2	-	8	51	1	5	15	2	-	20	55
	Conditioned in $He+H_2O$	1	2	34	1	-	6	51	1	2	45	1	-	4	44	N/A							N/A						
	Aluminized	44	2	2	1	-	7	44	N/A							42	2	1	1	-	10	43	28	3	2	1	-	17	48
	Aluminized & conditioned in $He+H_2O$	42	1	1	1	1	3	52	N/A							18	5	3	1	1	22	49	25	3	2	1	1	14	53

*Domains with distinct chemistries

4.4. Shot peening

4.4.1. Corrosion results

Grain refinement is a crucial aspect of shot peening and since the tribotests are conducted at elevated temperatures, recrystallisation effects must be considered. However, the exposure to high temperature during tribotesting (2 hours maximum) may not effectively recrystallize the near-surface regions, as indicated in Figure 83 and Figure 84, which show cross-section SEM images of shot-peened 800HT and 617, respectively, before and after exposure to elevated temperatures in argon. Aqua Regia was used as the etchants for 60s to reveal the grain structure.

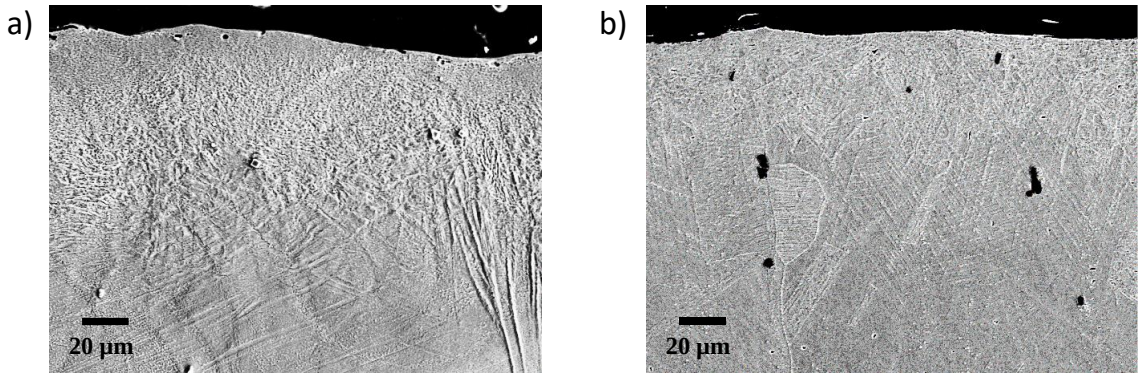

Figure 83. (a) SEM cross-sectional image of an alloy 800HT coupon after shot peening at 4.1 bar for 30s. (b) SEM cross-sectional image of an alloy 800HT coupon after shot peening followed by heating to 750 °C in Ar for 2 hrs.

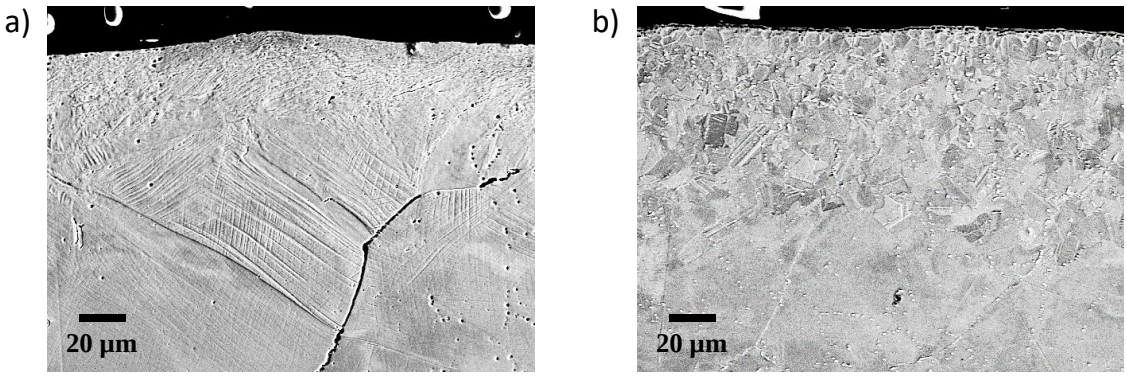

Figure 84. (a) SEM cross-sectional image of an alloy 617 coupon after shot peening at 4.1 bar for 75s. (b) SEM cross-sectional image of an alloy 617 coupon after shot peening followed by heating to 900 °C in Ar for 2 hrs.

In Figure 83, it appears that shot-peened alloy 800HT undergoes some deformation of the near surface with grain refinement. In literature, the mean grain size for 800HT is reduced from 70 µm to sub-micron after shot-peening with a 70-µm-deep deformation zone [40]. These values are consistent with the results presented in Figure 83. For alloy 617, the deformation is less severe, but the grain refinement is still observed in Figure 84. Since

recrystallization will not occur during tribotesting, it is expected that the oxidation rate will be increased.

SEM cross-sectional images and composition profiles of shot-peened samples after conditioning in Regime II are presented in Figure 85 and Figure 86.After conditioning, shot-peened 800HT samples developed a flaky chromium oxide on top of an aluminum oxide. The oxide scale developed is equal in thickness (1.50 ± 0.26 μm) to that developed in Regime II 800HT (1.33 ± 0.44 μm). The weak adherence of the external oxide is likely to diminish the mechanical integrity of the oxide scale. The cross-sectional analysis of shot-peened 617 samples conditioned in Regime II reveals a chromium oxide thicker and more uniform than that of Regime II samples due to enhanced chromium diffusion – the average thickness (3.68 ± 0.88 μm) is higher than that of the background oxide for Regime II samples (1.00 ± 0.20 μm) and similar to that of the oxide developed on top of the grain boundaries for Regime II samples (3.50 ± 0.17 μm) – which is consistent with the increase in grain boundary distribution at the surface after shot peening. This observation indicates that the kinetics of chromium outward diffusion was faster than recrystallisation for alloy 617. The benefit of shot-peening to develop more uniform oxide scale has been observed previously in super-critical water environments [38].

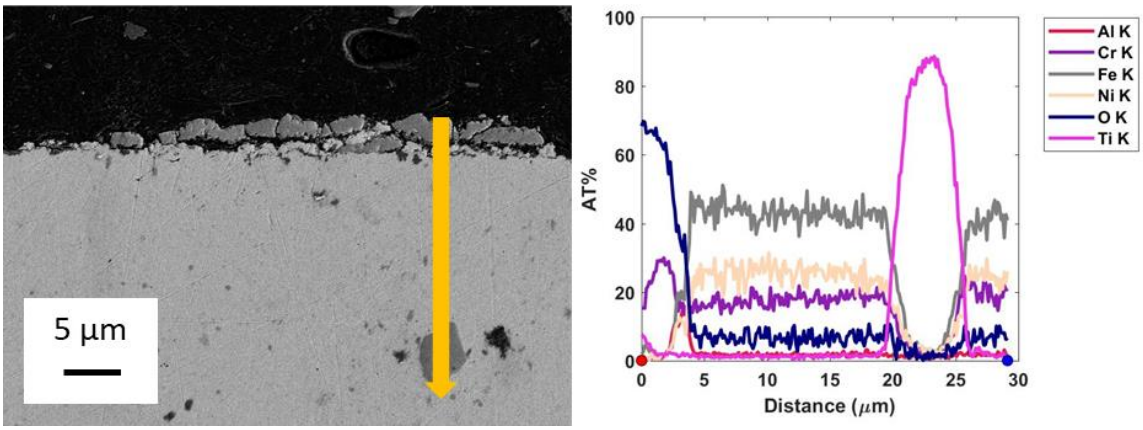

Figure 85: Cross-sectional SEM image and EDS line scan of shot-peened 800HT conditioned in Regime II.

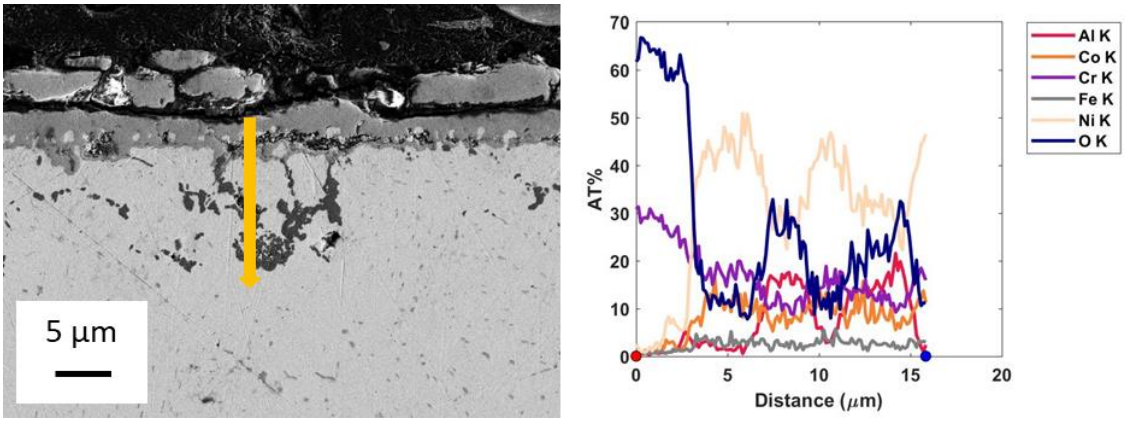

Figure 86: Cross-sectional SEM image and EDS line scan of shot-peened 617 conditioned in Regime II.

4.4.2. Tribological test results

Figure 87 and Figure 88 present the morphologies and compositions of the shot-peened 800HT wear tracks. Scuffing and gouging appear as the two main wear mechanisms at both loads. The background of the samples consists in a mixed Fe-Cr-Ni oxide rather than a simple iron oxide because of the enhanced chromium diffusion and the aggressive air-

oxidizing environment. Debris and patches are enriched in iron because the reactive broken bonds tend to favor iron oxidation over chromium that requires diffusion.

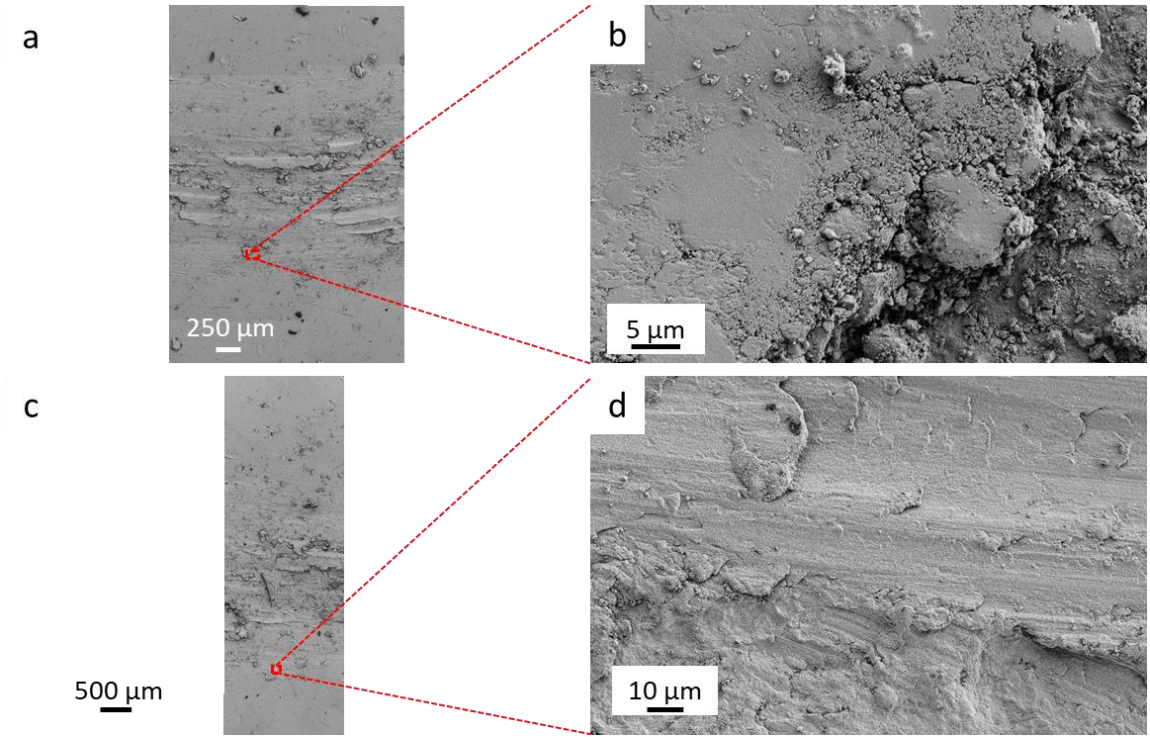

Figure 87: Morphology of the shot-peened 800HT wear tracks for (a, b) a 1N load at 750 °C and for (c, d) a 5N load at 750 °C.

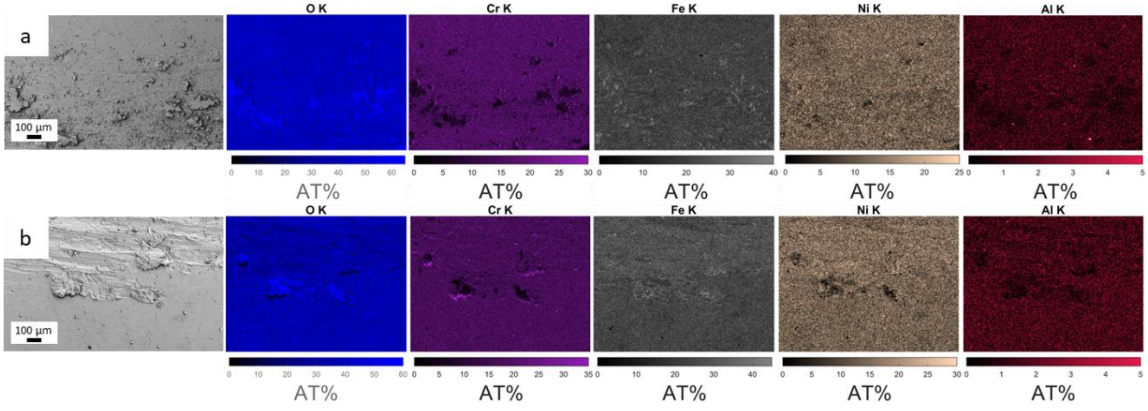

Figure 88: Top-down SEM and EDS maps of shot-peened 800HT wear tracks for (a) a 1N load at 750 °C and (b) a 5N load at 750 °C.

The morphologies and composition of the shot-peened 617 wear tracks are presented in Figure 89 and Figure 90. Mild scuffing is the wear mechanism observed at both loads. The compositional analysis of the background reveals the formation of chromium oxide because of the enhanced chromium diffusion, unlike as-received samples that only presented bulk composition. Debris and patches consist in oxide with metallic proportions similar to bulk material. This phenomenon is due to the reactive broken bonds that capture oxygen before chromium can diffuse through grain boundaries.

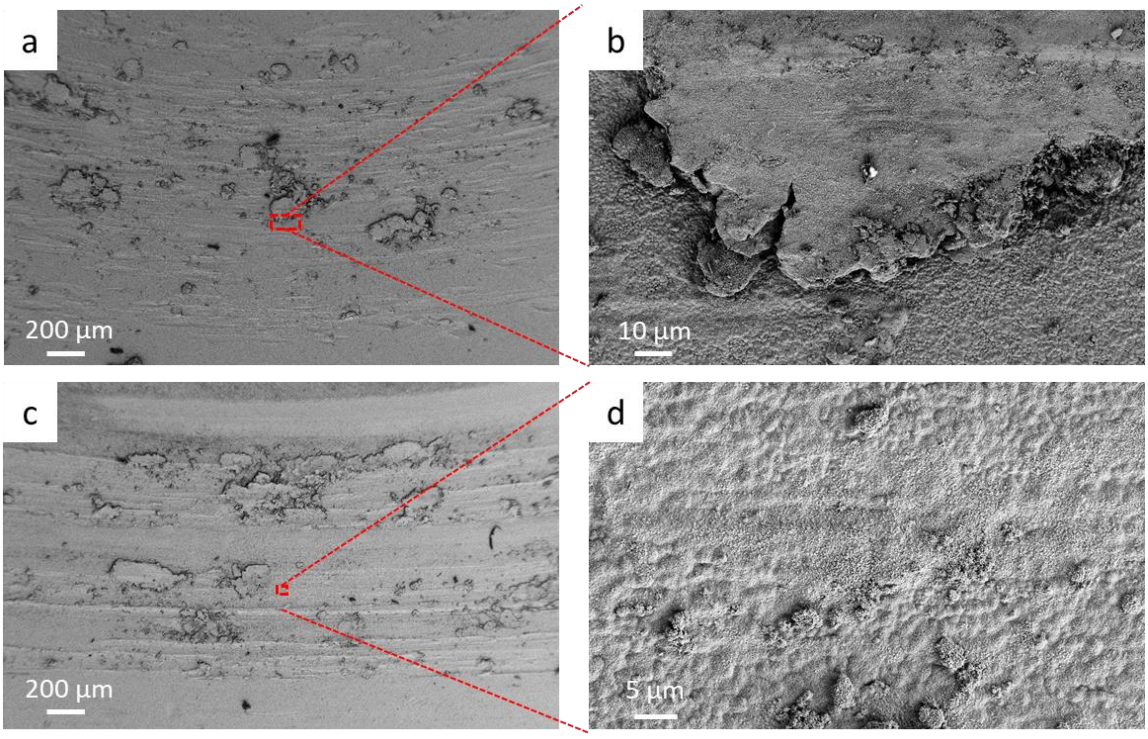

Figure 89: Morphology of the shot-peened 617 wear tracks for (a, b) a 1N load at 900 °C and for (c, d) a 5N load at 900 °C.

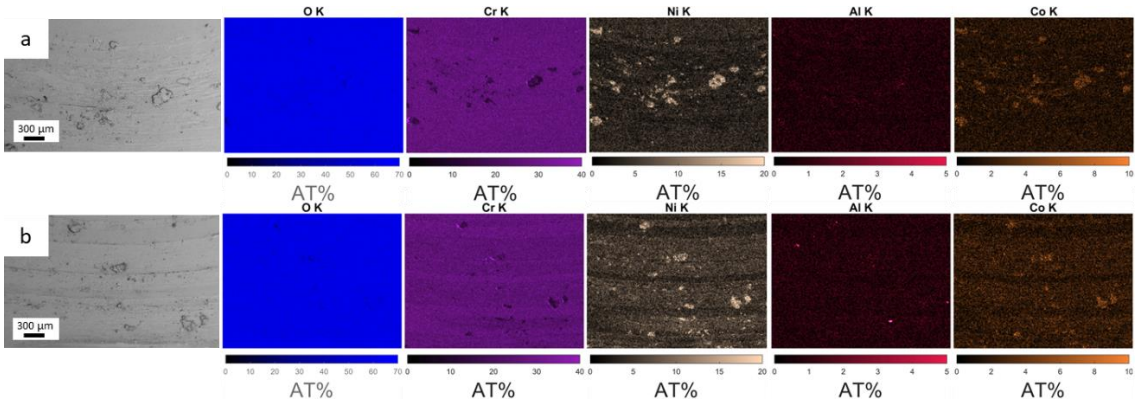

Figure 90: Top-down SEM and EDS maps of shot-peened 617 wear tracks for (a) a 1N load at 900 °C and (b) a 5N load at 900 °C.

Profilometry images, wear volumes and initial friction coefficients for both alloys are presented in Figure 91 and Figure 92. For alloy 800HT, profilometry results indicate slightly more severe wear than that for as-received samples. However, the wear volumes and initial friction coefficient values do not show any significant difference compared to Regime I samples. Shot-peened 617 samples present the same wear severity and initial friction coefficient values as that of as-received samples except at higher load where the wear volume was reduced by 60%. According to profilometry images, higher-load tribotests present deeper but more scattered grooves than tested in Regime I. These observations are consistent with the wear volume results that show slightly lower wear and shorter run-in periods for shot-peened samples.

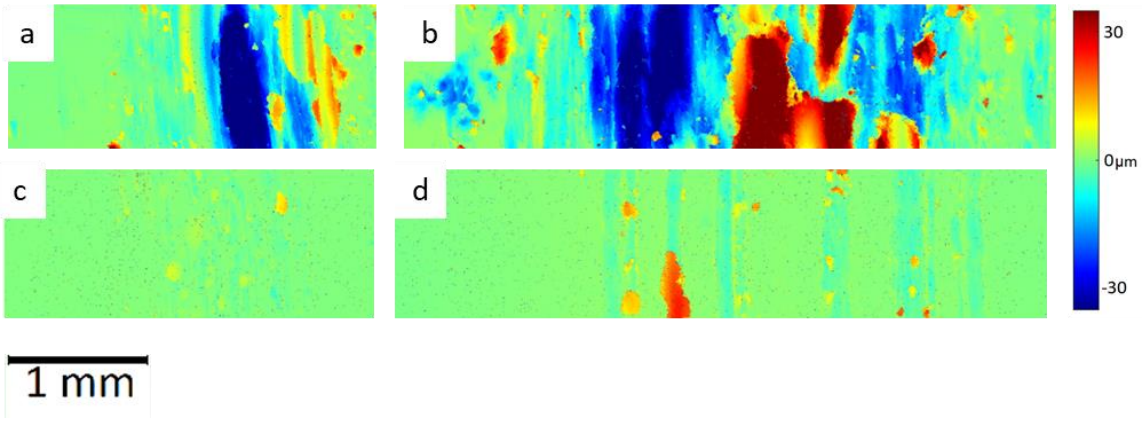

Figure 91: Wear track profilometry for (a, b) shot-peened 800HT tested at 1N, 750 °C and 5N, 750 °C, respectively and (c, d) shot-peened 617 tested at 1N, 900 °C and 5N, 900 °C, respectively.

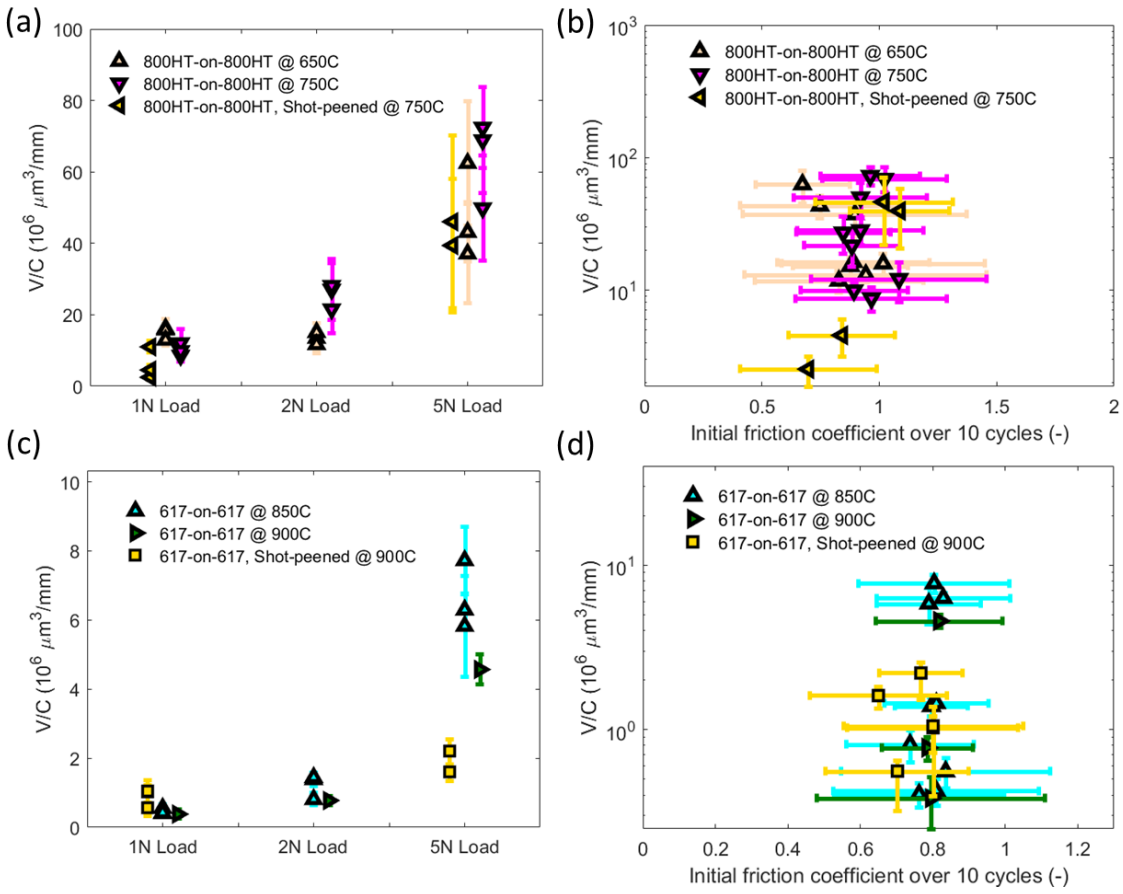

Figure 92: Wear volumes as a function of load (a, c) and initial friction coefficient (b, d) for shot-peened and as-received self-mated 800HT and 617 tested at elevated temperatures.

Figure 93 and Figure 94 show the wear track morphologies and compositions of shot-peened 800HT conditioned in Regime II. In terms of wear mechanisms, oxide breakthrough, scuffing and gouging occur at both loads. The compositional analysis of the samples' background reveals patches of chromium oxide when the flaky external oxide was not removed and aluminum oxide and/or Ni-Fe bulk composition otherwise. The wear track consists in Ni-Fe-rich patches, consistent with the notion of oxide breakthrough.

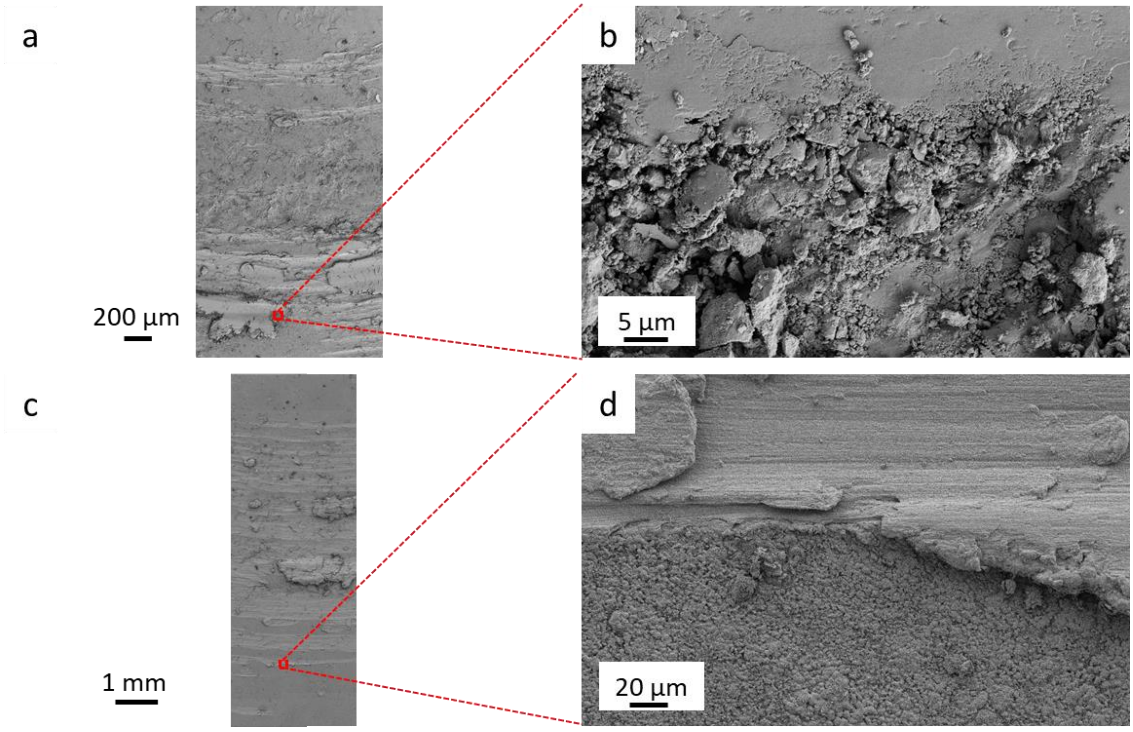

Figure 93: Morphology of the shot-peened 800HT wear tracks after conditioning in Regime II for (a, b) a 1N load at 750 °C and for (c, d) a 5N load at 750 °C.

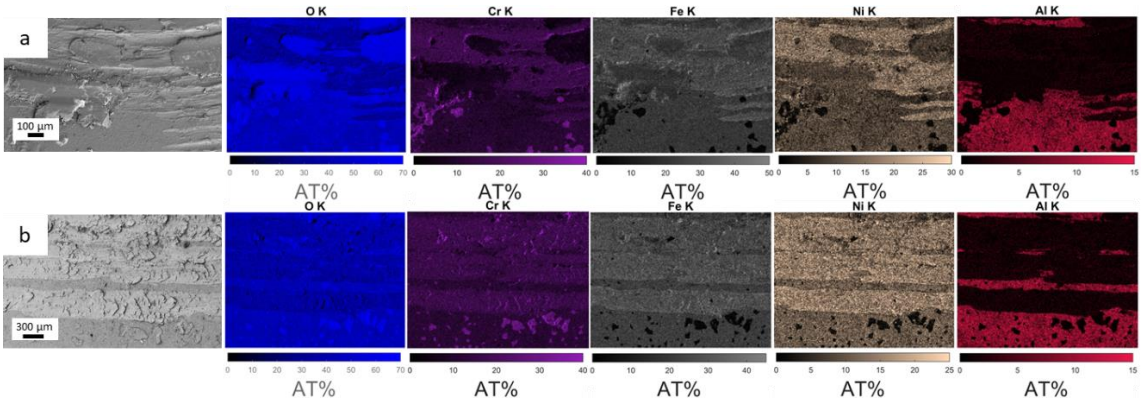

Figure 94: Top-down SEM and EDS maps of shot-peened 800HT after conditioning in Regime II for (a) a 1N load at 750 °C and (b) a 5N load at 750 °C.

The wear track morphologies and compositions of shot-peened 617 conditioned in Regime II presented in Figure 95 and Figure 96 indicate the formation of a protective glaze layer

at both loads. The glaze consists in the pre-existing chromium oxide, unlike in Regime II where its composition comprised the same metallic proportions as the bulk. This difference is likely due to the enhanced chromium diffusion that favored a thicker and more uniform oxide scale on the surface. For the same reason, the area fraction of the glaze is higher than that of Regime II.

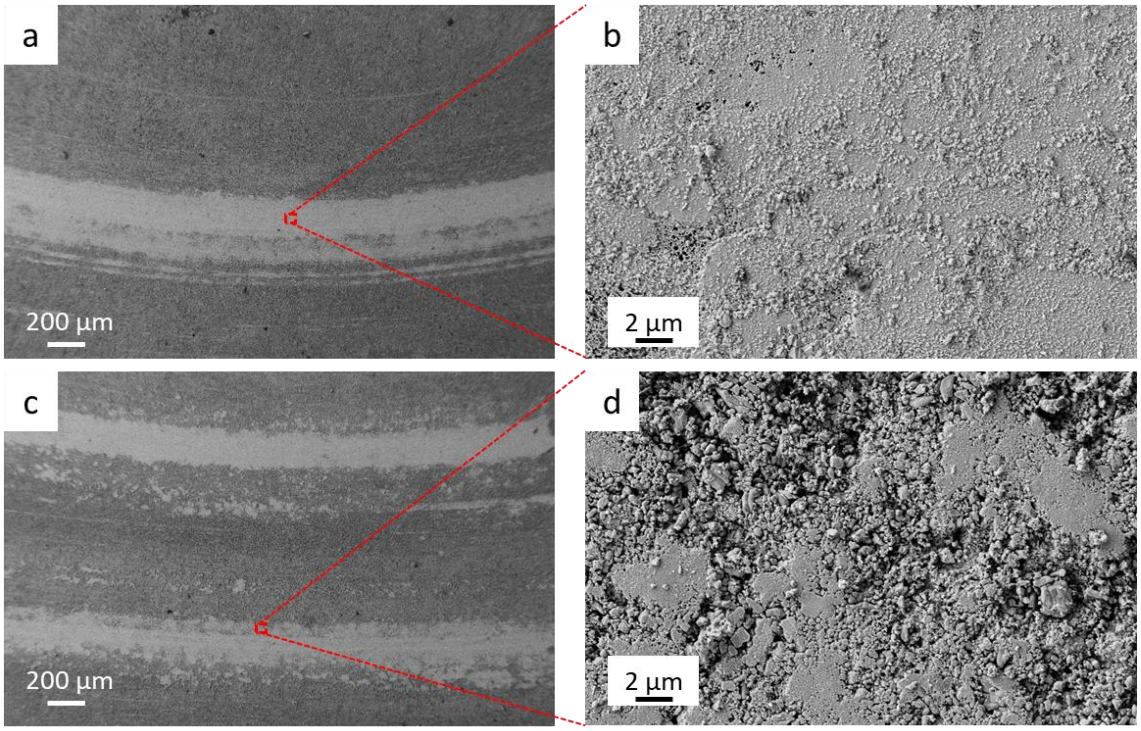

Figure 95: Morphology of the shot-peened 617 wear tracks after conditioning in Regime II for (a, b) a 1N load at 900 °C and for (c, d) a 5N load at 900 °C.

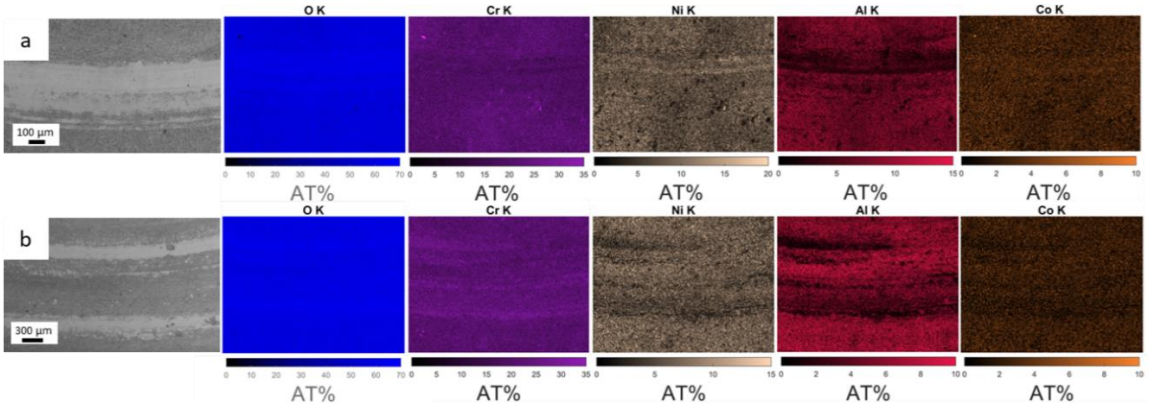

Figure 96: Top-down SEM and EDS maps of shot-peened 617 wear tracks after conditioning in Regime II for (a) a 1N load at 900 °C and (b) a 5N load at 900 °C.

Figure 97 and Figure 98 present the profilometry topographical images as well as the wear volumes and initial friction coefficients values of shot-peened samples conditioned in Regime II for both alloys. For alloy 800HT, the profilometry analysis reveals more severe wear than that of Regime II at low load and similar wear at higher load. The initial friction coefficients are as high as that of shot-peened samples and higher than that of samples conditioned in Regime II which confirms that the oxide did not play a role in the wear behavior of the samples. Similarly, wear volumes are comparable to that of shot-peened samples and samples conditioned in Regime II that experienced oxide breakthrough. For alloy 617, no noticeable difference is observed for shot-peened 617 samples conditioned in Regime II compared to samples conditioned in Regime II in terms of wear volumes, initial friction coefficients or wear severity.

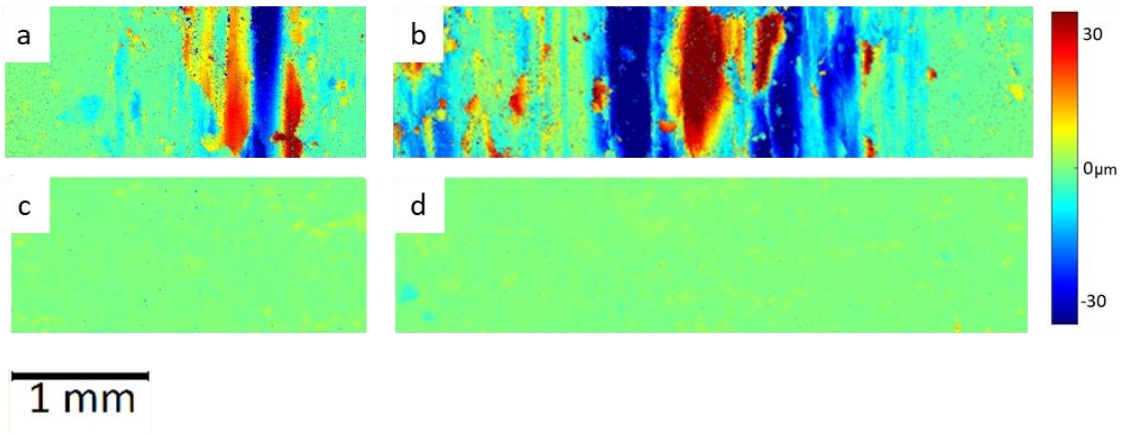

Figure 97: Wear track profilometry for (a, b) shot-peened 800HT after conditioning in Regime II and tested at 1N, 750 °C and 5N, 750 °C, respectively and (c, d) shot-peened 617 after conditioning in Regime II and tested at 1N, 900 °C and 5N, 900 °C, respectively.

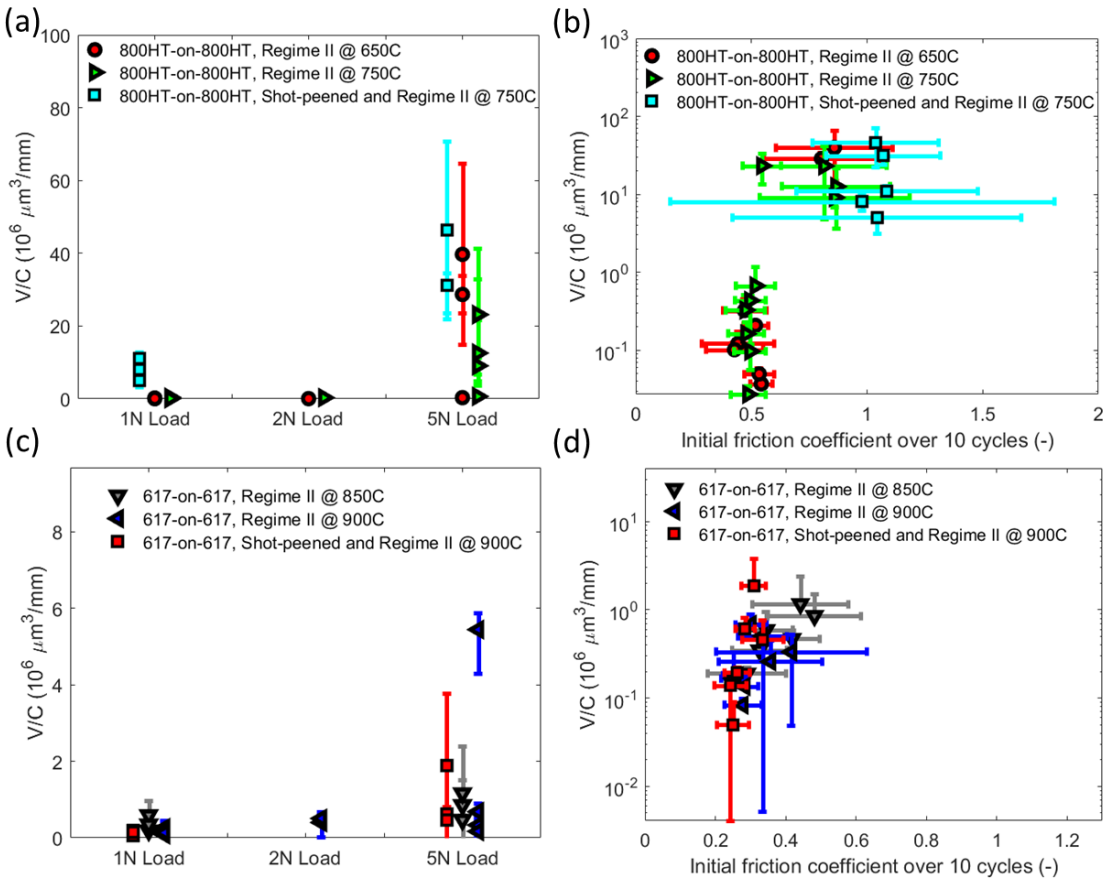

Figure 98: Wear volumes as a function of load (a, c) and initial friction coefficient (b, d) for self-mated 800HT and 617 after conditioning in Regime II, after shot peening, and after shot peening followed by conditioning in Regime II.

4.5. Steady-state friction coefficients

In addition to initial friction coefficients, the values of the steady-state friction coefficients for each tribotest was measured. The steady-state friction coefficients give indications regarding the resistance to sliding after the run-in period. Figure 99 presents the steady-state friction coefficients for all the regimes presented in this study.

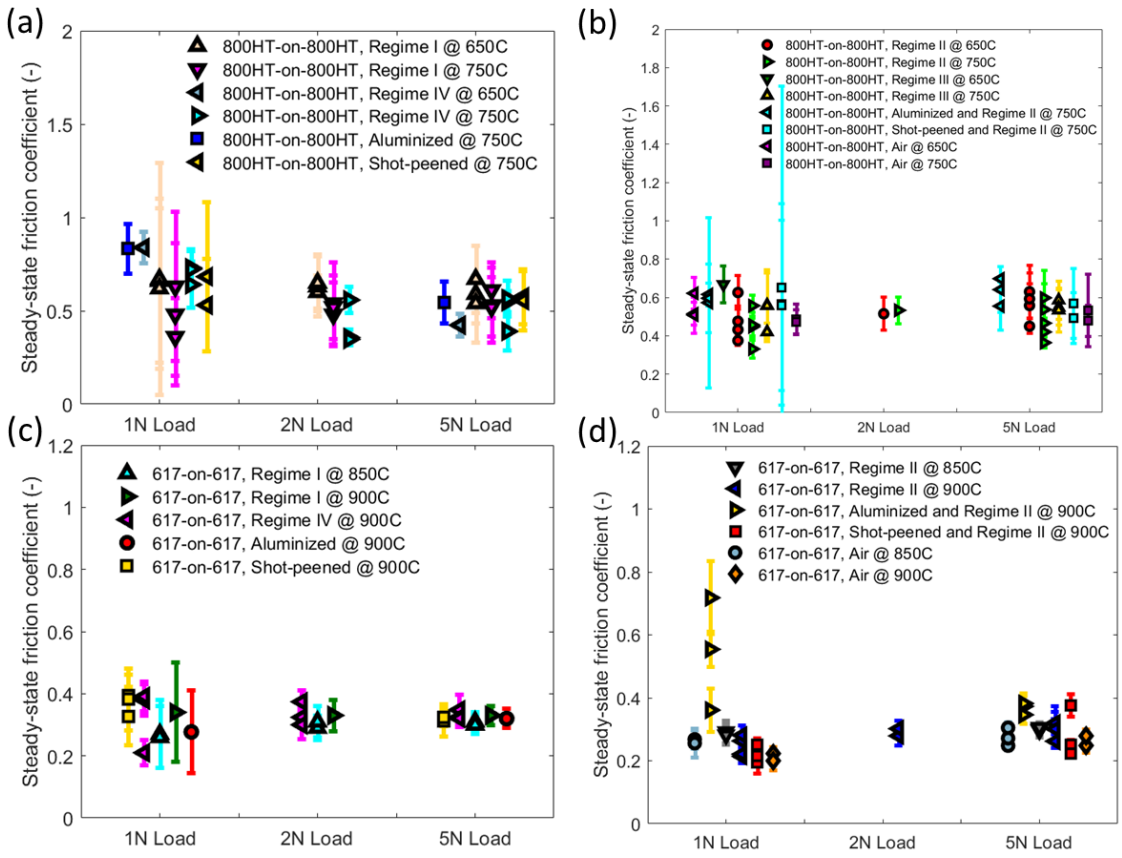

Figure 99: Steady-state friction coefficients for (a) 800HT without exposure to oxidizing conditions prior to tribotesting, (b) 617 without exposure to oxidizing conditions prior to tribotesting, (c) 800HT after exposure to elevated-temperature oxidizing conditions, and (d) 617 after exposure to elevated-temperature oxidizing conditions.

While the initial friction coefficients values can vary dramatically as a function of the regime and the loading level, it appears that the steady-state friction coefficients present similar values for almost all regimes. For many cases, this result is not unexpected since, even if the initial stages of the sliding contact are sensitive to the conditioning, the surfaces can develop similar resistance to shear after the run-in period within the ambient environment of the THT.

In the case of alloy 800HT, the final interacting surfaces have comparable chemistries. The layers in contact might be glaze, debris or bulk material with varying degrees of chromium and nickel, but they all consist of Fe-rich layers with different degrees of oxidation. The average steady-state friction coefficient is 0.55 ± 0.10.

Alloy 617 tends to develop interacting surfaces with bulk composition that can be oxidized to different degrees. Aluminized samples conditioned in Regime II are the only group of tribotests that present a significant difference with the average steady-state friction coefficient for alloy 617. This discrepancy is due to the presence of the flaky aluminum oxide that formed during conditioning that may still be present in the wear tracks in several cases. On average, the steady-state friction coefficient is 0.31 ± 0.08.

The standard deviation of the steady-state friction coefficients also gives indication regarding the stick-slip behavior of the contact. If the surface has not been extensively oxidized prior to or during the tribotest, solid state bonding may occur, leading to local welding. This phenomenon adds significant variation in the friction coefficient, hence an increased standard deviation of the result as shown in **Figure** 100.

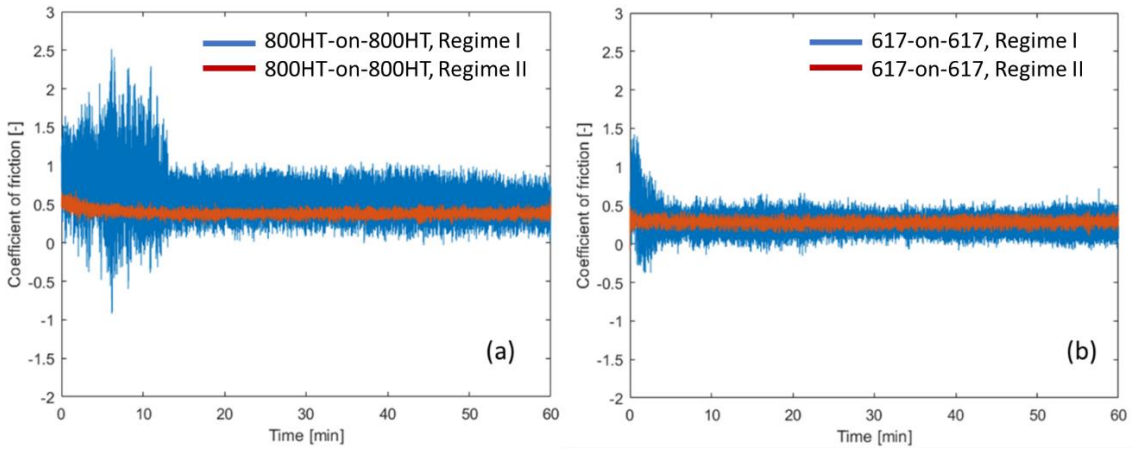

Figure 100: Coefficient of friction vs. time for (a) as-received 800HT and 800HT after conditioning in Regime II and (b) as-received 617 and 617 after conditioning in Regime II.

For alloy 800HT, this feature is visible for Regime I, shot-peened and shot-peened samples conditioned in Regime II which failed to completely develop a protective oxide scale during the test. The standard deviations for these regimes are on average twice as large as those of other regimes such as Regime II and IV that developed a protective oxide layer due to pre-conditioning or enhanced oxidation rate during the tribotest. For alloy 617, this phenomenon is not as visible as for alloy 800HT, but it is also present.

5. DISCUSSION

For both alloys 800HT and 617, the wear volumes and the initial friction coefficients provide information on both the resistance to wear volume loss and the initial state and strength of the surface, respectively. The initial friction coefficient correlates with the severity of wear immediately upon contact and provides insight into the wear mechanism.

The wear volume reflects the extent to which the surface was damaged during the process of reaching steady state. The wear mechanisms can be identified by examining the SEM-EDS maps, ranging in wear severity from high to low as follows: (i) base-metal wear characterized by gouging, scuffing, and debris formation followed by debris redeposition within the wear track; (ii) oxide breakthrough followed by wear of the base alloy; (iii) oxide wear without breakthrough; (iv) oxide compaction leading to the formation of a protective glaze-oxide, with no wear of the underlying base metal.

Alloy 617 presents order-of-magnitude lower wear volumes, 12% lower initial friction coefficients and 44% lower steady-state friction coefficients than those of alloy 800HT, demonstrating its superior wear resistance. This result is supported by previous studies that investigated the tribological performance of as-received samples in high-temperature air and high-temperature HTGR-like environments [14]. That same study showed that tribotesting the samples in an aggressively oxidizing environment such as air tends to lower the friction coefficient of the sliding contact. Previous studies also stated that some oxides are harder and more brittle than others, and that moderate strains can crack and rupture iron oxide [47]. In addition to lower high-temperature strength, this phenomenon provides an explanation for why alloy 800HT presents lower wear resistance than alloy 617 since it develops an iron oxide when exposed to air at high temperature.

The wear volume results demonstrate that the most efficient way to mitigate wear is to form a mechanically stable oxide on the sample surface that becomes a glaze layer if the correct conditions are met. This protective scale has been obtained for three different cases: Regime II, Regime IV and Regime II after shot peening. When the surfaces of conditioned alloys remained undamaged due to the formation of a protective glaze-oxide layer, the initial friction coefficients were half, on average, of those of both as-received samples and conditioned samples that experienced oxide breakthrough. For example, for alloy 800HT, the initial coefficient of friction for conditioned alloy 800HT that did not experience oxide breakthrough was 0.494 +/- 0.044, whereas the initial as-received coefficient of friction was 0.904 +/- 0.126, and the initial coefficient of friction for conditioned 800HT that experienced oxide breakthrough was 0.820 +/- 0.122. Similarly, for alloy 617, the initial coefficient of friction for conditioned alloy 617 that did not experience oxide breakthrough was 0.341 +/- 0.075, whereas the initial as-received coefficient of friction was 0.804 +/- 0.077 and the initial coefficient of friction for conditioned 617 that experienced oxide breakthrough was 0.867 +/- 0.255. Thus, the differences in the initial coefficient are due to the degree to which the surface oxide can support the contact stresses without being broken through. The SEM-EDS maps confirm the oxide-breakthrough mechanism suggested by the trends in initial friction coefficient. Wear volumes within the same order of magnitude for as-received samples and conditioned samples with oxide breakthrough demonstrate that the strength of the base metal strongly influences the resistance to volume loss either when no protective oxide is present or when the surface oxide that is present is not of sufficient

mechanical integrity. For example, at 5 N applied load, the wear volume for as-received 800HT was 55.65 +/- 15.45 x 10^6 μm^3/mm, and the wear volume for as-received 617 was 6.10 +/- 1.39 x 10^6 μm^3/mm. These values are within the same order of magnitude as those found by Rahman et al. when assuming a wear track diameter of 17.5mm: ~11 x 10^6 μm^3/mm and ~8 x 10^6 μm^3/mm for alloy 800HT at 750°C under a 5N load with a sliding velocity of 0.04 m/s and alloy 617 at 950°C under a 5N load with a sliding velocity of 0.1 m/s, respectively [48], [49]. For conditioned alloys that experienced oxide breakthrough, also at 5 N load, the wear volume for conditioned alloy 800HT was 22.63 +/- 14.00 x 10^6 μm^3/mm, and the wear volume for conditioned alloy 617 was 5.44 +/- 0.87 x 10^6 μm^3/mm. The yield strength of 617 at 850-900 °C is higher than that of 800HT at 650-750 °C (256 – 169 MPa versus 120-123 MPa, respectively), which explains the relatively higher wear volumes of 800HT compared to 617 when the base metal is worn (discussed in more detail in [50]). When the oxide is protective, and glaze-oxide-layer formation occurs, wear volumes are negligible.

For Regime IV (Kolsterised), only alloy 800HT developed a glaze layer on its surface at lower load, and the enhanced oxidation rate was high enough such that a thick oxide could form during tribotesting, which was not the case for as-received samples. Initial friction coefficients for Kolsterised alloy 800HT were half, on average, of those of as-received alloy 800HT despite the surfaces of both samples being unoxidized initially - $\mu_{initial}$ = 0.385 +/- 0.078 for Kolsterised 800HT; $\mu_{initial}$ = 0.904 +/- 0.126 for as-received 800HT. This

difference is due to the rapid oxide formation on the Kolsterised alloy 800HT surface during the temperature ramp of the tribometer. Similar initial friction coefficients for all Kolsterised samples indicate that oxide wear was the dominant mechanism at the start of the tribotests for every load. At low load, the oxidation rate enhanced by the Kolsterising process led to the formation of a glaze-oxide layer, with wear volumes similar to those of conditioned samples with a glaze-oxide. At high load, the oxide was worn but was still able to support the contact stresses and prevent wear of the underlying base metal which is consistent with the strong influence of substrate strength on the resistance to volume loss described above. The wear volumes of the Kolsterised samples were between those of the conditioned samples that experienced glaze-oxide-layer formation and conditioned samples that experienced oxide breakthrough. For example, at 5 N load, wear volume was 3.15 +/- 2.64 x 10^6 μm^3/mm for Kolsterised alloy 800HT.

Unlike alloy 800HT, initial friction coefficients for Kolsterised alloy 617 have comparable values (0.693 ± 0.077) to those of as-received alloy 617, which is consistent with scuffing of the base metal observed in the SEM-EDS maps for both conditions. For alloy 617, the oxidation rate was only slightly enhanced by the Kolsterising® process; therefore, any oxide formed during temperature ramp-up of the tribometer was insufficient to protect the base alloy from experiencing wear. The wear volumes for Kolsterised samples compared to as-received samples are significantly lower, likely due to the increased strength of the

surface caused by the increased carbon content. For example, at 5 N load, wear volume was 0.49 +/- 0.18 x 10^6 μm^3/mm for Kolsterised alloy 617.

At every load tested, alloy 800HT after Kolsterising® followed by conditioning (Regime III) exhibited initial friction coefficients similar to those of conditioned samples that experienced oxide breakthrough, which is consistent with scuffing and debris being present for both conditions. At 5 N load, μinitial was 0.861 +/- 0.086 for 800HT after Kolsterising® followed by conditioning, and μinitial was 0.820 +/- 0.122 for conditioned 800HT with oxide breakthrough. Surface chemistries were slightly different between the two types of samples due to the increased Mn content in the oxide induced by Kolsterising®, but friction coefficients were similar because of similar wear mechanisms. The lower wear volumes of samples after Kolsterising® followed by conditioning compared to those of conditioned samples with oxide breakthrough are due to the enhanced strength of the substrate from the increased carbon concentration. For example, at 5 N load, wear volume was 14.87 +/- 1.57 x 10^6 μm^3/mm for alloy 800HT after Kolsterising® followed by conditioning, and wear volume was 22.63 +/- 14.00 x 10^6 μm^3/mm for conditioned 800HT with oxide breakthrough. The lack of robustness of the interface between the internal and external oxide formed on the Kolsterised samples prevented the formation of a protective glaze-oxide layer, and a mild degree of base metal wear still occurred.

Regarding the aluminization treatment, with aluminized alloy 800HT, aluminization improved hardness from 3.63 GPa to 7.33 GPa and therefore improved wear resistance

over that of as-received 800HT. The degree of scuffing was significantly lower than that of as-received alloy 800HT due to the harder aluminized surface. Any oxide that formed during temperature ramp-up of the tribometer failed to support the contact stresses, as evidenced by both the scuffing-type morphology of the worn region and the higher value of the initial friction coefficient compared to the cases where the oxide layer persisted. For aluminized alloy 800HT after conditioning (Regime II), the oxide produced was unable to support the contact stresses, and ceramic wear occurred. The underlying Fe-Al and Ni-Al zones have a hardness that is higher than that of the base alloy (4.63 GPa vs 3.63 GPa) but lower than that of the aluminized surface prior to conditioning. Therefore, although the oxide produced by conditioning the aluminized samples was unable to support the contact stresses, wear is improved over that of the conditioned alloy 800HT samples that experienced oxide breakthrough followed by base-metal wear. For aluminized alloy 617, neither the increase in surface hardness from 4.18 GPa to 7.58 GPa, nor the oxide formed during temperature ramp-up of the tribometer, were able to improve the wear resistance of aluminized 617 significantly over that of as-received 617. The oxide that formed during temperature ramp-up was worn through during tribotesting, and regions of the aluminized zone was worn through as well, as evidenced by Cr-rich patches within the wear track. The oxide wore via ceramic wear. The harder underlying Ni-Al zone was exposed, and wear volumes reflect the volume of surface oxide material that was removed by the wear process. With aluminized alloy 617 after conditioning (Regime II), the oxide produced was unable to support the contact stresses, and ceramic wear occurred. Because the oxide formed on

aluminized 617 from the conditioning process was thick (10.54 ± 2.64 μm thickness), wear volumes reflect the removal of this layer down to the underlying Ni-Al zone, which resulted in worn volumes that are larger than those measured for aluminized 617 without conditioning. Wear volumes increased by a factor of five compared to those measured with oxide-breakthrough cases of conditioned alloy 617 without aluminization.

It appears that aluminization treatment is beneficial for alloy 800HT, especially before conditioning in Regime II. However, the wear behavior for aluminized 617 was not improved relative to that of as-received 617 and was even worse when the samples were conditioned. This result suggests that the aluminization process could be further optimized for 617. Figure 101 shows that, if the exposure of the aluminization process is reduced from 36 to 24 hours, the Al-rich layer is smoother and appears more stable mechanically, which is likely to improve the wear behavior of the aluminized samples.

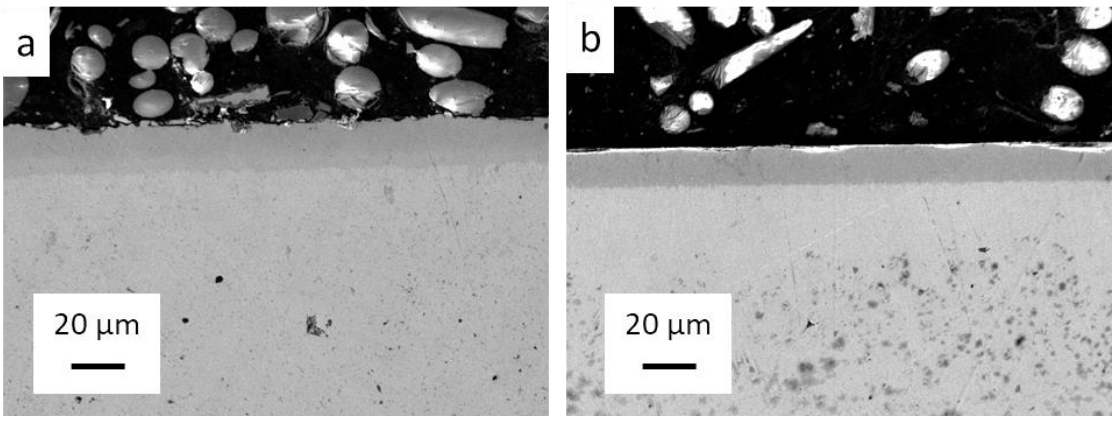

Figure 101: Cross-sectional SEM images of (a) 800HT aluminized for 24 hours and (b) 617 aluminized for 24 hours.

Tribological results for aluminized 800HT and 617 were limited to a single data point due to time constraints. Several tests revealed that similar testing conditions can lead to drastically different wear mechanisms and wear volumes. For example, some of the Regime II samples tested at higher load experienced oxide breakthrough, while others developed a low-wear glaze-oxide layer. Since such stochastic effects have been observed near threshold loads, it is important to consider the results presented for conditions with only a single point with caution.

Shot peening had the expected effect of promoting the formation of a more uniform chromium oxide on both alloys. This observation is likely due to grain refinement of the near surface, which increased the grain boundaries distribution and hence enabled a more uniform diffusion of chromium. For alloy 800HT, shot peening also promoted the formation of an aluminum oxide on the surface, which is likely to have affected the mechanical integrity of the chromium oxide that formed on top of it. The hardness of shot-peened samples might not be significantly higher than that of as-received samples due to a degree of annealing during tribotesting. The stress threshold to trigger wear is expected to be higher for harder materials, and run-in periods are expected to be shorter. Since the wear volumes and the run-in histories are comparable for as-received and shot-peened samples, it is likely that there is no significant difference in terms of surface hardness.

For conditioned shot-peened samples (Regime II), a glaze layer was formed only for alloy 617 because the mechanical integrity of the oxide formed on alloy 800HT was poor. These observations present several key results for mitigating the wear of high-temperature alloys. The formation of the glaze layer is a combination of sufficient oxidation rate, high-temperature strength and structural integrity of the oxide scale. If the oxidation rate is too low, it can be replaced by pre-conditioning of the samples, as in the case for alloy 617 conditioned in Regime II. If the high-temperature strength is too low, the oxide scale formed will break because the sub-layer bulk material is too soft, and this is what occurred with alloy 800HT conditioned in Regime II at higher load. The lack of high-temperature strength can be compensated by an increased oxide thickness as long as its integrity is not compromised. Additionally, if the mechanical integrity of the oxide is not adequate, it will be removed from the wear track before any oxide debris can start sintering together – this phenomenon occurred for shot-peened 800HT samples conditioned in Regime II.

The choice to conduct the tribological tests in ambient air is justified as follows. Initial tribotesting of as-received samples were conducted in inert environments including dry nitrogen and dry argon. However, due to the enclosure system of the THT, the moisture level was unable to be maintained such that oxidation of samples was prevented. Moreover, the friction curves and the wear volumes measured from the inert-environment tests were similar to those obtained from tests that were run in ambient air. Therefore, it was concluded that the systematic tribotesting would be performed in ambient air in order to

maximize throughput of the tribotesting. Although ambient air is not representative of HTGR environments, the tribological results have demonstrated that oxide layers as thin as 1 μm can be sufficient to protect the surface from intensive wear, thus reducing the importance of having a testing environment identical to that of HTGR conditions.

In HTGR environments, carburization of the materials will be the consequence of corrosion from species such as CH_4 and CO. Since this alteration of the surface is happening at high temperatures with ppmv levels of impurities, it is likely to be in the form of carbides created at the near surface. The original procedure chosen to carburize the samples was to condition them at high temperature for several days while exposing them to a mix of helium with 20 ppmv of CH_4. However, even with the level of oxidizing impurities (H_2O and O_2) below 0.5 ppmv, oxidation of the samples still occurred to some degree. Therefore, Kolsterising® was chosen as an innovative approach for carburization since no oxidation would occur during the Kolsterising® process. Although this process does not produce any carbides due to the lower process temperatures, it offers a good substitute for carburization because the hardness of the samples is increased. Additionally, Regime III samples are exposed to high temperature for several days after Kolsterising®. This conditioning enables the diffusion of carbon out of the samples, thus leading to surface atomic percentages of carbon that resemble those expected in HTGR, and also likely triggering the formation of carbides in the alloy. Therefore, Regime III is taken to be a good representation of how an oxidizing and carburizing HTGR environment would corrode the materials.

To determine whether or not the tribological behavior is governed by the applied load or the initial mean contact stress, a series of experiments were performed: a 0.25 N load with a 55.3-mm pin and a 5 N load with a 255.4-mm pin for a contact stress of 33 MPa, as well as a 1 N load with a 16.3-mm pin and a 11 N load with a 55.3-mm pin for a contact stress of 120 MPa. Figure 102 presents the dependence of the wear volume for 800HT conditioned in Regime II as a function of the applied load for the two different mean contact stresses. The results support the conclusion of Wang et al. where higher loads lead to higher wear rates, with mean contact stress not being the main driver of the wear behavior [29]. Therefore, all tribological results presented herein are shown as a function of the applied load as opposed to the mean contact stress. Additionally, the results do not indicate any clear differences in terms of wear mechanisms, wear volumes or friction coefficients as a function of the testing temperatures investigated. A potential decrease in wear volume with increasing temperature was observed in previous studies due to the increased oxidation rate [17]. Yet, the decrease in yield strength of the bulk materials may counter this phenomenon.

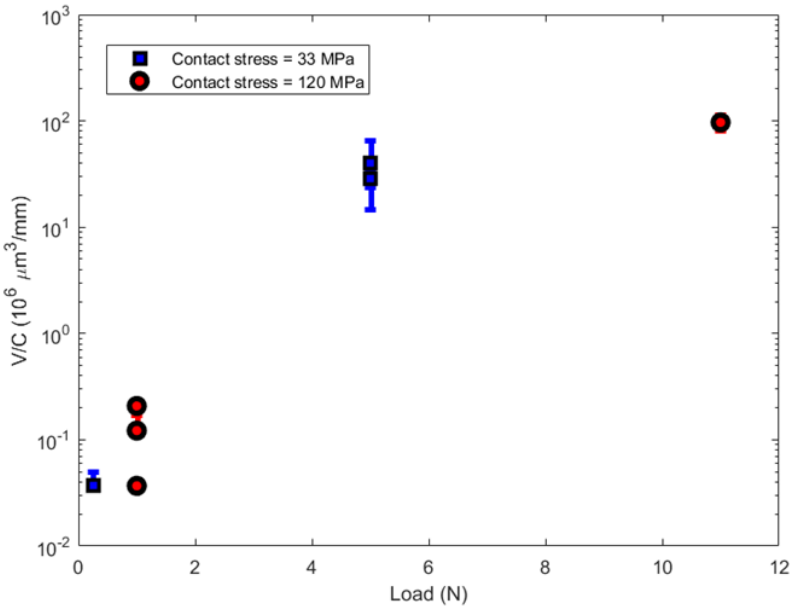

Figure 102: Wear volumes of 800HT samples conditioned in Regime II as a function of the load for two different initial mean contact stresses.

It is important to note that, in addition to initial coefficients of friction, steady-state coefficients of friction were also discussed. We showed that the steady-state friction coefficients of as-received and conditioned samples are similar for a given material and are independent of the wear mechanism. This similarity is due to the nature of the oxidation at the pin-disk interface that ultimately develops during wear testing at high temperatures in the ambient air environment of the tribometer. Different steady-state coefficients of friction were measured for as-received Inconel™ 617 [49] at 950 °C and Incoloy™ 800HT at 750 °C [48] in air and impure He environments under a 5N load. The vast majority of material removal due to the wear process occurs during the run-in period. For this reason, initial

coefficients of friction are emphasized herein as they provide the needed insight into the tribological behavior as the samples are experiencing wear.

6. CONCLUSION

The tribological behavior of Incoloy® 800HT and Inconel® 617 have been studied under four different regimes of corrosion, representative of the potential environments in HTGR. In addition, aluminization and shot peening were investigated as two possible surfaces treatments for improving the wear resistance of the two alloys. The wear behavior of the surface-treated samples was also studied before and after conditioning the alloys in an oxidizing HTGR environment.

Corrosion results demonstrated that 4 ppmv of H_2O in a pure helium background environment is sufficient to form an oxide scale on both alloys when exposed to elevated temperatures for 22 days – 750 °C for 800HT, and 900 °C for 617. In this oxidizing environment, a chromium oxide forms, and the oxides are about the same thickness for alloys 800HT and 617. This protective scale increased the wear resistance compared to that of as-received samples, especially when a compacted glaze layer formed during sliding, leading to wear volumes below the detection limits of the measurement technique. For alloy 800HT, the glaze layer consisted of iron oxide, and for alloy 617, it consisted of a mixed oxide with metallic elements present in the same proportions as those of the bulk material. Additionally, the initial friction coefficients were reduced by 45% and 54% for

alloys 800HT and 617, respectively, and the variability of the steady-state friction coefficients of the conditioned samples decreased appreciably. Conditioning the samples in air led to wear volumes and steady-state friction coefficients that were comparable to those measured after conditioning in Regime II. For alloy 800HT, initial friction coefficients were higher for samples conditioned in air compared to those for samples conditioned in Regime II because the patches of oxide had to be smoothened before the glaze layer was able to form.

After the samples were Kolsterised, the oxidation rate was enhanced for both alloys, as indicated by the thicknesses of the oxide after tribotesting. This phenomenon enabled the creation of a glaze layer for 800HT at low load without the presence of an oxide prior to tribotesting. In addition, the increased hardness of the near-surface regions drastically reduced the wear volumes compared to those of as-received samples for both alloys, rendering wear almost unmeasurable. The initial friction coefficients were unaffected by Kolsterising® for alloy 617, but they were reduced by 50% for alloy 800HT. After conditioning in Regime III, alloy 800HT formed a Mn-Cr oxide that gave rise to wear behavior similar to the oxide breakthrough seen with samples conditioned in Regime II. Aluminization decreased the wear volumes by an order of magnitude for alloy 800HT. The formation of a hard FeAl intermetallic phase is likely to be the cause of increased wear resistance. This increase in wear resistance after aluminization was not observed for alloy 617. Compared to as-received 617, an increase in wear volume at lower load and a decrease

in wear volume at higher load were measured. The same amount of material was removed at both loads and wear stopped when the harder intermetallic phase was reached. For alloy 800HT, the initial and steady-state friction coefficients of aluminized samples were lower than those of as-received samples. On the contrary, at higher load, alloy 617 exhibited higher initial friction coefficients than those of as-received samples due to significant material removal during the initial stages of sliding. In both cases, conditioning the samples in an oxidizing environment after aluminization decreased the wear performance of the alloys. For alloy 800HT, friction coefficients were comparable to those of Regime II cases where the oxide was broken through. Additionally, wear volumes were higher than those of Regime II cases where a glaze layer formed indicating that the oxide formed was not as protective as the glaze layer. Alloy 617 developed a thick and flaky aluminum oxide on the surface, causing the wear volumes to increase by a factor of five compared to those measured in the Regime II oxide-breakthrough cases. The initial friction coefficients and steady-state friction coefficients for alloy 617 were increased by 60% and 300%, respectively, compared to those measured after Regime II conditioning.

Shot peening the samples yielded results comparable with those for as-received samples in terms of wear volumes, initial friction coefficients, and steady-state friction coefficients, except for high-load testing of alloy 617, where the wear volume was decreased by 60% likely due to increased hardness. After conditioning in an oxidizing environment, shot-peened 800HT developed a mechanically unstable oxide scale on the surface that exhibited

wear resistance that was inferior to that measured with the Regime II samples that displayed oxide breakthrough. For alloy 617, the conditioned shot-peened samples consistently developed a glaze layer on the surface at both loads, and friction coefficients were comparable to those of alloy 617 conditioned in Regime II. Yet, it appears that the more uniform and thicker oxide developed for these samples compared to that of Regime II samples enhances the wear resistance of alloy 617 because of the formation of a more stable glaze layer.

The results presented for the shot-peened or aluminized samples suggest that further optimization can be done to improve the wear resistance of both alloys for HTGR applications. Indeed, both techniques involve tuning of several parameters in order to reach an optimized surface state prior to exposure to corroding and wearing conditions. Alloy 800HT benefited from the aluminization treatment, whereas alloy 617 did not; alloy 617 benefited from shot peening, whereas alloy 800HT did not. Thus, it can be hypothesized that both surface treatments can be optimized further to improve the wear behavior for both alloys under HTGR conditions.

The wear resistance of alloy 617 was found to be superior to that of alloy 800HT, with wear volumes an order of magnitude lower, initial friction coefficients 12% lower, and steady-state friction coefficients 44% lower on average compared to those of alloy 800HT.

Based on the results presented, it appears that a low-wear glaze layer will form only if several corrosion and testing conditions are met:

1. A rapidly forming or a pre-formed oxide must be present on the surface
2. The base alloy must have a good high-temperature strength
3. The interface between the oxide and the alloy must present a strong mechanical integrity
4. The contact stress during the sliding must not exceed the threshold of oxide breakthrough.

7. REFERENCES

[1] "U.S. Electricity Generation by Energy Source," U.S. Energy Information Administration, 1 March 2019. [Online]. Available: https://www.eia.gov/tools/faqs/faq.php?id=427&t=3. [Accessed 2 July 2019].

[2] "Electricity Statistics," International Energy Agency, [Online]. Available: https://www.iea.org/statistics/electricity/. [Accessed 1 July 2019].

[3] "Comparison of Lifecycle Greenhouse Gas Emissions of Various Electricity Generation Sources," World Nuclear Association.

[4] "U.S. Energy Information Administration - Table 6.7.A. Capacity Factors for Utility Scale Generators Primarily Using Fossil Fuels, January 2013-April 2019," 25 June 2019. [Online]. Available: https://www.eia.gov/electricity/monthly/epm_table_grapher.php?t=epmt_6_07_a. [Accessed 1 July 2019].

[5] "U.S. Energy Information Administration - Table 6.7.B. Capacity Factors for Utility Scale Generators Not Primarily Using Fossil Fuels, January 2013-April 2019," 25 June 2019. [Online]. Available: https://www.eia.gov/electricity/monthly/epm_table_grapher.php?t=epmt_6_07_b. [Accessed 1 July 2019].

[6] S. M. Goldberg & R. Rosner, Nuclear Reactors: Generation to Generation, American Academy of Arts and Sciences, 2011.

[7] "Generation IV Nuclear Reactors," World Nuclear Association, [Online]. Available: http://www.world-nuclear.org/information-library/nuclear-fuel-cycle/nuclear-power-reactors/generation-iv-nuclear-reactors.aspx. [Accessed 1 July 2019].

[8] "Very-High-Temperature Reactor (VHTR)," The Generation IV International Forum, 1 October 2013. [Online]. Available: https://www.gen-4.org/gif/jcms/c_9362/vhtr. [Accessed 1 July 2019].

[9] R. Wright, "Summary of studies of aging and environmental effects on Inconel 617 and Haynes 230," *INL/EXT-06-11750,* p. 27, 2006.

[10] C. A. Greene, "Materials Behaviour in HTGR Environments," *NUREG/CR-6824, ANL-02/37,* 2003.

[11] T. Burchell et al., "Next Generation Nuclear Plant Materials Research and Development Program Plan," Idaho National Laboratory, Idaho Falls, 2007.

[12] K. Staszewska and M. Scendo, "Mechanism and kinetics oxidation of Inconel 617 and 625 alloys," *Technical Issues,* vol. 1, pp. 82-89, 2016.

[13] R. Wright, "Kinetics of gas reactions and environmental degradation in NGNP helium," *INL/EXT-06-11494*, 2008.

[14] A. A. Polycarpou et al., "Elevated temperature tribology of Ni alloys under helium environments for nuclear reactor applications," *Tribology International,* no. 123, pp. 372-384, 2018.

[15] C. Jang et al., "Oxidation behavior of an Alloy 617 in very high-temperature air and helium environments," *Inter. Journal of Pressure Vessels and Piping,* no. 85, pp. 368-377, 2008.

[16] F. H. Stott et al., "The structure and mechanism of formation of the 'glaze' oxide layers produced on nickel-based alloys during wear at high temperatures," *Corrosion Science,* no. 13, pp. 449-469, 1973.

[17] F. H. Stott et al., "The Tribological Behavior of Nickel and Nickel-Chromium Alloys at Temperature from 20 °C to 800 °C," *Wear,* no. 36, pp. 147-174, 1976.

[18] W. J. Quadakkers et al., "Corrosion of High Temperature Alloys in the Primary Circuit Helium of High Temperature Gas Cooled Reactors. Part II: Experimental Results," *Werkstoffe und Korrosion,* no. 36, pp. 335-347, 1985.

[19] W. J. Quadakkers et al., "Thermodynamic and kinetic aspects of the corrosion of high-temperature alloys in high temperature gas-cooled reactor helium," *Nucl. Technol.,* no. 66, p. 383, 1984.

[20] C. Cabet and F. Rouillard, "Corrosion of high temperature metallic materials in VHTR," *Journal of Nuclear Materials,* vol. 392, pp. 235-242, 2009.

[21] C. Cabet et al., "High temperature corrosion of structural materials under gas-cooled reactor helium," *Mater. & Corrosion,* no. 57, p. 147, 2006.

[22] H.-J. Christ et al., "High Temperature Corrosion of the Nickel-based Alloy Inconel 617 in Helium Containing Small Amount of Impurities," *Materials Science and Engineering,* no. 87, pp. 161-168, 1987.

[23] P. J. Blau, "Elevated-temperature tribology of metallic materials," *Tribology International,* no. 43, pp. 1203-1208, 2010.

[24] R. Nieder, "Prediction on an HTR Coolant Composition After Operational Experience with Experimental Reactors," in *Specialists Meeting on Coolant Chemistry, Plate-out and Decontamination in Gas Cooled Reactors,* Juelich, Germany, 1980.

[25] R. D. Burnette and N. L. Baldwin, "Primary Coolant Chemistry of the Peach Bottom and Fort St. Vrain High Temperature Gas-Cooled Reactors," in *Specialists*

Meeting on Coolant Chemistry, Plate-out and Decontamination in Gas Cooled Reactors, Juelich, Germany, 1980.

[26] R. A. Simon and P. D. Capp, "Operating Experience with the Dragon High Temperature Reactor Experiment," in *Proceedings on High Temperature Reactors*, Petten, Netherlands, 2002.

[27] "Special Metals website," 2018. [Online]. Available: http://www.specialmetals.com/assets/smc/documents/alloys/incoloy/incoloy-alloys-800h-800ht.pdf.

[28] "Special Metals website," 2018. [Online]. Available: http://www.specialmetals.com/assets/smc/documents/alloys/inconel/inconel-alloy-617.pdf .

[29] S. Q. Wang et al., "Mild-to-severe wear transition and transition region of oxidative wear in steels," *Wear,* vol. 306, pp. 311-320, 2013.

[30] F. H. Stott, "High-temperature sliding wear of metals," *Tribology International*, vol. 35, pp. 489-495, 2002.

[31] F. H. Stott, "The role of oxidation in the wear of alloys," *Tribology International*, vol. 31, no. 1-3, pp. 61-71, 1998.

[32] Y. Birol, "High temperature sliding wear behavior of Inconel 617 and Stellite 6 alloys," *Wear,* no. 269, pp. 664-671, 2010.

[33] Bodycote, "Kolsterising," Bodycote, [Online]. Available: https://www.bodycote.com/technical-glossary/kolsterising/. [Accessed 7 July 2019].

[34] "Status report 96 - High Temperature Gas Cooled Reactor - Pebble-Bed Module (HTR-PM)," Tsinghua University, Beijing, 2011.

[35] Byeong Woo Lee, "Effect of diffusion coatings on the high-temperature properties of nickel-chromium superalloys," *International Journal of Modern Physics B,* vol. 32, no. 19, p. 1840056, 2018.

[36] J.-K. Chen et al., "Formation of Al and Cr Dual Coatings by Pack Cementation on SNCM439 Steel," *ISIJ International,* vol. 52, no. 1, pp. 127-133, 2011.

[37] Q. Y. Zhang et al., "Wear Behavior and Mechanism of Fe-Al Intermetallic Coating Prepared by Hot-Dip Aluminizing and Diffusion," *Metallurgical and Materials Transactions A,* vol. 47, no. 5, pp. 2232-2242, 2016.

[38] L. Tan, X.Ren, K. Sridharan and T. R. Allen, "Corrosion behavior of Ni-base alloys for advanced high temperature water-cooled nuclear plants," *Corrosion Science,* vol. 50, pp. 3056-3062, 2008.

[39] X. Ren, K. Sridharan and T. R. Allen, "Effect of grain refinement on corrosion of ferritic-martensitic steels in supercritical water environment," *Materials and Corrosion,* vol. 61, no. 9, 2010.

[40] L. Tan, X. Ren, K. Sridharan and T. R. Allen, "Effect of shot-peening on the oxidation of alloy 800H exposed to supercritical water and cyclic oxidation," *Corrosion Science,* vol. 50, pp. 2040-2046, 2008.

[41] G. Gulsoy and G. S. Was, "Surface oxidation of Alloy 617 in low oxygen partial pressure He-CO-CO2 environments at 750-850 °C," *Corrosion Science,* vol. 90, pp. 529-534, 2015.

[42] Bodycote, "Kolsterising - FAQ," Bodycote, [Online]. Available: http://blog.bodycote.com/2017/06/17/frequently-asked-questions-kolsterising/. [Accessed 26 July 2019].

[43] Y. Cao, F. Ernst and G. M. Michal, "Colossal carbon supersaturation in austenitic stainless steels carburized at low temperature," *Acta Materialia,* vol. 51, pp. 4171-4181, 2003.

[44] S. G. &. F. Stott, "Aluminizing of iron-nickel-base alloys for resistance to high-temperature gaseous environments," *Corrosion Scienc,* vol. 33, no. 3, pp. 345-35, 1992.

[45] J. Chin et al., "Compatibility of aluminide-coated Hastelloy X and Inconel 617 in a simulated gas-cooled reactor environment," in *International Conference on Metallurgical Coatings and Process Technology*, San Diego, 1982.

[46] Q. Y. Z. e. al., "Wear Behavior and Mechanism of Fe-Al Intermetallic Coating Prepared by Hot-Dip Aluminizing and Diffusion," *Metallurgical and Materials Transactions A,* vol. 47, no. 5, pp. 2232-2242, 2016.

[47] A. Cameron et al., "The relationship between oxide films and the wear of steels," *Wear,* vol. 113, pp. 203-223, 1986.

[48] J. D. A. B. X. Z. a. A. A. P. S. Rahman, "Tribology of incoloy 800HT for nuclear reactors under helium environment at elevated temperatures," *Wear,* no. 436–437, p. 1–11, 2019.

[49] J. D. A. B. X. Z. a. A. A. P. S. Rahman, "Helium Tribology of Inconel 617 at Elevated Temperatures up to 950°C: Parametric Study," *Nucl. Sci. Eng.*, vol. 193, p. 998–1012, 2019.

[50] V. P. e. al., "High-temperature tribological behavior of structural materials after conditioning in impure-helium environments for high-temperature gas-cooled reactor applications," *J. Nucl. Mater.*, vol. 522, p. 311–323, 2019.

[51] I. Green, "Poisson ratio effects and critical values in spherical and cylindrical Hertzian contacts," *Applied Mechanics and Engineering,* no. 10(3), p. 451, 2005.

[52] Baryshev et al., "Characterization of Surface Modifications by White Light Interferometry: Applications in Ion Sputtering, Laser Ablation, and Tribology Experiments," *Journal of Visualized Experiments,* no. 72-50260, 2013.

[53] A. Pauschitz et al., "Mechanisms of sliding wear of metals and alloys at elevated temperatures," *Tribology International,* vol. 41, pp. 584-602, 2008.

[54] "Generation IV reactor - Wikipedia," [Online]. Available: https://en.wikipedia.org/wiki/Generation_IV_reactor. [Accessed 2019].

[55] "Advanced Nuclear Power Reactors," World Nuclear Association, [Online]. Available: http://www.world-nuclear.org/information-library/nuclear-fuel-cycle/nuclear-power-reactors/advanced-nuclear-power-reactors.aspx. [Accessed 1 July 2019].

[56] "Molten-Salt Reactors," What is Nuclear, [Online]. Available: https://whatisnuclear.com/msr.html. [Accessed 1 July 2019].

[57] "AP1000 Pressurized Water Reactor," Westinghouse Electric Company, [Online]. Available: http://www.westinghousenuclear.com/new-plants/ap1000-pwr. [Accessed 1 July 2019].

[58] "European Pressurized Reactor," Framatome, [Online]. Available: http://www.framatome.com/EN/businessnews-136/framatome-large-projects--management-and-execution-of-nuclear-reactor-new-build-projects.html. [Accessed 1 July 2019].

[59] H. Cho and B. W. Lee, "High temperature properties of surface-modified Hastelloy X alloy," *Journal of Korean Crystal Growth and Crystal Technology*, vol. 22, no. 4, pp. 183-189, 2012.

8. APPENDIX

Contact stresses may play an important role in the tribological behavior of the two alloys. The initial mean contact stress was controlled by selecting both the radius of curvature of the pin and the load of the tribotest. An approximation of the initial contact stress was computed via Hertzian contact equations with the following assumptions:

1. The strains within the contacting bodies are small and within the elastic limit,
2. Each body can be considered an elastic half-space, i.e., the radius of contact is small compared to the radius of the tribopin,
3. The contacting bodies are homogeneous, isotropic, and linear elastic,
4. Friction is neglected in the calculations of contact stress. This assumption is reasonable since it concerns the initial contact stress.

Hertzian contact mechanics allows for the computation of the initial mean contact stress P_{mean} via Equations 12, 13 and 14:

$$P_{mean} = \frac{P}{\pi a^2} \tag{12}$$

$$a = \left(\frac{3 * P * R}{4 * E_p}\right)^{\frac{1}{3}} \tag{13}$$

$$E_p = \frac{1}{\frac{1-\nu_1^2}{E_1} + \frac{1-\nu_2^2}{E_2}} \tag{14}$$

With P being the applied load, a the contact radius, R the radius of curvature of the pin, E_1 and E_2 the Young moduli of the materials, and ν_1 and ν_2 the Poisson's ratios of the

materials. The combinations of load and radius of curvature considered in this study give the following contact stresses:

- Radius of 255.4 mm with a 5N load: ~30 MPa
- Radius of 55.3 mm with a 2N load: ~65 MPa
- Radius of 16.3 mm with a 1N load: ~120 MPa.

Initial maximum von-Mises stresses were computed to compare the initial stress within the contact zone with the high-temperature yield strengths of the materials [51]. The yield strengths and the von-Mises stresses for the chosen initial mean contact stresses are shown in Figure 103.

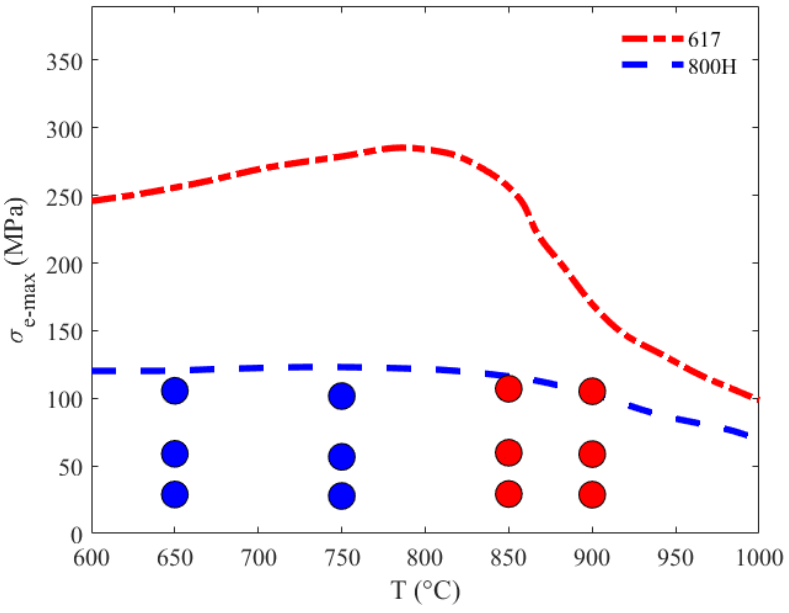

Figure 103: Yield strength versus temperature for alloys 800HT and 617 [27, 28]. The initial maximum von-Mises stresses for the tribotesting are plotted at the temperatures at which the respective alloys were tested.